University of Alberta

THICK/THIN FILM SULFUR OXIDE CHEMICAL SENSOR

by

Craig Dennis Eastman

A thesis submitted to the Faculty of Graduate Studies and Research in partial fulfillment of the

Doctor of Philosophy

in

Materials Engineering

Department of Chemical and Materials Engineering

Edmonton, Alberta

Fall 2006

Library and Archives Canada

Published Heritage Branch

395 Wellington Street
Ottawa ON K1A 0N4
Canada

Bibliothèque et Archives Canada

Direction du Patrimoine de l'édition

395, rue Wellington
Ottawa ON K1A 0N4
Canada

Your file Votre référence
ISBN: 978-0-494-23022-0
Our file Notre référence
ISBN: 978-0-494-23022-0

NOTICE:
The author has granted a non-exclusive license allowing Library and Archives Canada to reproduce, publish, archive, preserve, conserve, communicate to the public by telecommunication or on the Internet, loan, distribute and sell theses worldwide, for commercial or non-commercial purposes, in microform, paper, electronic and/or any other formats.

The author retains copyright ownership and moral rights in this thesis. Neither the thesis nor substantial extracts from it may be printed or otherwise reproduced without the author's permission.

AVIS:
L'auteur a accordé une licence non exclusive permettant à la Bibliothèque et Archives Canada de reproduire, publier, archiver, sauvegarder, conserver, transmettre au public par télécommunication ou par l'Internet, prêter, distribuer et vendre des thèses partout dans le monde, à des fins commerciales ou autres, sur support microforme, papier, électronique et/ou autres formats.

L'auteur conserve la propriété du droit d'auteur et des droits moraux qui protège cette thèse. Ni la thèse ni des extraits substantiels de celle-ci ne doivent être imprimés ou autrement reproduits sans son autorisation.

In compliance with the Canadian Privacy Act some supporting forms may have been removed from this thesis.

While these forms may be included in the document page count, their removal does not represent any loss of content from the thesis.

Conformément à la loi canadienne sur la protection de la vie privée, quelques formulaires secondaires ont été enlevés de cette thèse.

Bien que ces formulaires aient inclus dans la pagination, il n'y aura aucun contenu manquant.

Canada

Abstract

In this experimental work, a series of chemical sensor designs utilizing a solid electrolyte consisting of Ag_2SO_4 and Li_2SO_4 combined with thin/thick film depositions were fabricated and tested [1, 2]. The sensors were exposed to mixtures of SO_2 in air varying from 0.6 to 2400 ppm SO_2 at 535 °C and 525 °C.

Cell No. 1: Pt working electrode – solid electrolyte (25 m/o Ag_2SO_4-75 m/o Li_2SO_4) – composite reference electrode material (2:1 wt. ratio of Ag: 25 m/o Ag_2SO_4-75 m/o Li_2SO_4). The cell was found to display the following response to mixtures from 94 to 900 ppm SO_2 in air at 535 °C:

$$Emf(V) = (0.2176 \pm 0.0043) + (0.0725 \pm 0.0016)\ log[SO_2 - ppm] \quad (94 - 900\ ppm\ SO_2)$$
$$R^2 = 0.9847$$

Cell No. 2: Pt thin film working electrode – solid electrolyte (25 m/o Ag_2SO_4-75 m/o Li_2SO_4) – thin film Ag reference electrode. Cell displayed fluctuating voltage when exposed to a mixture of 496 ppm of SO_2 in air at 535 °C.

Cell No. 3: Pt thin film working electrode – solid electrolyte (25 m/o Ag_2SO_4-75 m/o Li_2SO_4) – Ag thick film reference electrode. The cell was found to display the following response to mixtures from 100 to 2400 ppm SO_2 in air at 525 °C:

$$Emf(V) = (0.1755 \pm 0.0044) + (0.0821 \pm 0.0014)\ log[SO_2 - ppm] \quad (100 - 2400\ ppm\ SO_2)$$
$$R^2 = 0.9931$$

Cell No. 4: Pt thin film working electrode – solid electrolyte (25 m/o Ag_2SO_4-75 m/o Li_2SO_4) – composite thick film reference electrode material (2:1 wt. ratio of Ag: 25 m/o Ag_2SO_4-75 m/o Li_2SO_4). The maximum gas concentration in each experimental run for cell No. 4 was determined according to the concentration of SO_2 in each gas cylinder utilized. In this part of the cell testing, five different cylinders of SO_2 in air were used. The cell was found to display the following responses for varying SO_2 ranges at 535 °C:

$$Emf(V) = (0.1658 \pm 0.0046) + (0.0824 \pm 0.0016)\ log[SO_2 - ppm]\ \ (100 - 2400\,ppm\,SO_2)$$
$$R^2 = 0.9968$$

$$Emf(V) = (0.1864 \pm 0.0027) + (0.0743 \pm 0.0012)\ \log[SO_2 - ppm]\ (10 - 496\,ppm\,SO_2)$$
$$R^2 = 0.9906$$

$$Emf(V) = (0.1686 \pm 0.0027) + (0.0816 \pm 0.0012)\ \log[SO_2 - ppm]\ (50 - 496\,ppm\,SO_2)$$
$$R^2 = 0.9995$$

$$Emf(V) = 0.2613 + 0.00162[SO_2] - 1.425x10^{-5}[SO_2]^2 + 5.255x10^{-8}[SO_2]^3\ \ (5.4 - 9.4\,ppm\,SO_2)$$
$$R^2 = 0.9998$$

$$Emf(V) = 0.2460 + \ 0.0024[SO_2 - ppm] - 1.389x10^{-5}[SO_2 - ppm]^2\ \ (0.6 - 11.6\,ppm\ SO_2)$$
$$R^2 = 0.9983$$

$$Emf(V) = (0.1810 \pm 0.0010) + (0.0769 \pm 0.0005)\log[SO_2 - ppm]\ (14.4 - 2400\,ppm\ SO_2)$$
$$R^2 = 0.9975$$

$$Emf(V) = (0.1723 \pm 0.0010) + (0.0802 \pm 0.0005)\log[SO_2 - ppm]\ (50 - 2400\,ppm\ SO_2)$$
$$R^2 = 0.9982$$

Cell No. 5 Pt thin film working electrode – thick film solid electrolyte (25 m/o Ag_2SO_4-75 m/o Li_2SO_4) – composite thick film reference electrode (2:1 wt. ratio of Ag: 25 m/o Ag_2SO_4-75 m/o Li_2SO_4). The cell was found to display a fluctuating response to mixtures from 71 to 947 ppm SO_2 in air at 535 °C.

The response of the sensor was found to closely match the theoretically expected values from 10 ppm to 2400 ppm of SO_2. Below 10 ppm the sensor was found to deviate from Nernstian behaviour. Several suggestions for the origin of the non-linear response at low concentrations are given. Recommendations for improvements to the

existing design and for future work directed towards miniaturization and full integration of this chemical sensor are also provided.

Dedication

I would like to thank the following organizations and individuals for their support:

Dr. T.H. Etsell for his advice and encouragement with all aspects of this research.

The Alberta Oil Sands Technology & Research Authority for funding this research.

The Alberta Microelectronic Centre for access to thin film deposition equipment and support for this work.

The University of Alberta for use of laboratory space and equipment.

A special dedication to my wife, Marilyn and daughter Lauren for their perseverance and encouragement during all phases of this work. And also to my parents, Wally and Shirley Eastman, especially to my mother who would have been very proud to have seen this accomplishment through to its final completion.

Table of Contents

CHAPTER 1: INTRODUCTION 1

CHAPTER 2: POTENTIOMETRIC CHEMICAL SENSORS 4

- IONIC CONDUCTIVITY 4
- ELECTRICAL CONDUCTIVITY 5
- MEASUREMENT OF CONDUCTANCE 9
- HIGH IMPEDANCE CONDUCTIVITY MEASUREMENTS 12
- IMPEDANCE SPECTROSCOPY 12

CHAPTER 3: POTENTIOMETRIC GAS SENSORS - CLASSIFICATION SYSTEM 15

- TYPE I SOLID ELECTROLYTE GAS SENSOR 15
- TYPE II SOLID ELECTROLYTE GAS SENSOR 16
- TYPE III SOLID ELECTROLYTE GAS SENSOR 20
- TYPE IIIA SOLID ELECTROLYTE GAS SENSOR 21
- TYPE IIIB SOLID ELECTROLYTE GAS SENSOR 22
- TYPE IIIC SOLID ELECTROLYTE GAS SENSOR 24

CHAPTER 4: LITERATURE REVIEW – SULFUR CHEMICAL SENSOR TECHNOLOGY 27

- FUSED SALTS 27
- SULFATE SOLID ELECTROLYTES 28
- ALTERNATIVE SOLID ELECTROLYTES 30
  - *SO_X Sensors:* *30*
  - *H_2S Sensors:* *37*

CHAPTER 5: SENSOR PERFORMANCE FACTORS 39

- SELECTIVITY 39
- SENSITIVITY 39
- ACCURACY 41
- LONG-TERM STABILITY 44
- RESPONSE TIME 44
- RECOVERY TIME 45
- WORKING LIFETIME 45

CHAPTER 6: FABRICATION TECHNIQUES 46

- FORMING AND PRESSING 46
- THICK FILM DEPOSITION 46
- THIN FILM DEPOSITION 52
  - *Traditional Evaporation* *52*
  - *Electron Beam Evaporation* *57*

CHAPTER 7: COMPONENTS OF EXPERIMENTAL SULFUR OXIDE SENSOR 59

- SOLID ELECTROLYTE LAYER: TWO PHASE Ag_2SO_4-Li_2SO_4 MIXTURE 59
- MECHANISM OF CONDUCTION IN SULFATE ELECTROLYTES 65
- REFERENCE ELECTRODE: Ag:Ag_2SO_4-Li_2SO_4 MIXTURE 66
- WORKING ELECTRODE: PLATINUM THIN FILM 69

CHAPTER 8: THEORETICAL CONSIDERATIONS-SULFUR OXIDE SENSOR 73

- THEORETICAL CELL VOLTAGE 73

CHAPTER 9 : EXPERIMENTAL SULFUR OXIDE SENSOR – FABRICATION PROCESS 75
THICK FILM SULFUR OXIDE SENSOR FABRICATION 75
CHAPTER 10 : CELL DESIGN AND OPERATION 79
CHAPTER 11 : EXPERIMENTAL RESULTS 83
CELL NO. 1: COMPOSITE REFERENCE ELECTRODE 83
CELL NO. 2: AG THIN FILM REFERENCE ELECTRODE 85
CELL NO. 3: AG THICK FILM REFERENCE ELECTRODE 88
CELL NO. 4: COMPOSITE THICK FILM REFFRENCE ELECTRODE 92
Experimental results: 100-2400 ppm SO_2 ..... *93*
Experimental results: 10-496 ppm SO_2 ..... *94*
Experimental results: 5.4-95.4 ppm SO_2 ..... *96*
Experimental results: 0.6-11.6 ppm SO_2 ..... *97*
Experimental results: 14.4-2400 ppm SO_2 ..... *98*
CELL NO. 4: FLOW RATE DEPENDENCE 101
CELL NO. 5: THICK FILM ELECTROLYTE 105
SUMMARY OF RESULTS 107
CALCULATION OF Ag_2SO_4 ACTIVITY 111
MICROGRAPHS AND CHEMICAL ANALYSIS OF ELECTRODES 114
X-RAY DIFFRACTION RESULTS 122
CHAPTER 12 : DISCUSSION OF RESULTS 125
SENSITIVITY ANALYSIS - CELL MEASUREMENTS 125
CELL MEASUREMENTS 128
Cell No. 1: Composite reference electrode *128*
Cell No. 2: Ag thin film reference electrode *129*
Cell No. 3: Ag thick film reference electrode *129*
Cell No. 4: Composite thick film reference electrode *130*
Cell No. 5: Thick film electrolyte *131*
GENERAL DISCUSSION 132
VOLTAGE DIFFERENTIAL AND SHIFT IN PARTIAL PRESSURES 133
CHAPTER 13: CONCLUSIONS, FUTURE WORK AND RECOMMENDATIONS 149
IMPROVED ELECTROLYTE 150
SENSOR INTEGRATION 153
ADDITIONAL AREAS 155
APPENDIX A: EXPERIMENTAL DATA FOR SULFUR OXIDE CHEMICAL SENSOR 158
APPENDIX B: METHOD OF LEAST SQUARES 175
APPENDIX C: STANDARD CELL POTENTIAL, E^o, AND ASSOCIATED ERROR 177
APPENDIX D: CELL EQUATION AND ASSOCIATED ERROR 180
APPENDIX E: PROPAGATION OF ERROR ANALYSIS 184
APPENDIX F: CALCULATION OF ADJUSTED CELL MOLAR FRACTION 185
REFERENCES 187

List of Tables

Table 3-1. Material configuration of Type I chemical sensors. 17
Table 3-2. Material configuration of Type II chemical sensors. 18
Table 3-3. Material configuration of Type IIIa chemical sensors. 23
Table 3-4. Material configuration of Type IIIb chemical sensors. 25
Table 3-5. Material configuration of Type IIIc chemical sensors. 26
Table 6-1. Thick film composition 50
Table 6-2. Dry print thickness. 51
Table 7-1. Conductivity of sulfates. 60
Table 7-2. Diffusion coefficients (D x 10^5 cm^2sec^{-1}) for some ions in solid sulfates 65
Table 7-3. Electronic mean free path of several metals. 72
Table 11-1. Summary of experimental results for Cell No. 1 - Composite reference electrode 109
Table 11-2. Summary of experimental results for Cell No. 3 - Thick film reference ... 109
Table 11-3. Summary of experimental results for Cell No. 4 - Thick film reference ... 110
Table 11-4. Average experimental activity, $a_{Ag_2SO_4}$, for cell No. 4 – Thick film reference, 14.4 to 2400 ppm SO_2 at 535 °C. 112
Table 12-1. Voltage and partial pressure shift. 134
Table 12-2. Furnace temperature profile. 137
Table 12-3. Adjusted Ag_2SO_4 activity 148
Table A-1. Cell No. 1: Composite reference electrode - emf versus [SO_2] and standard deviation (STDEV) of emf from 94 to 900 ppm SO_2 in air at 535 °C. 158
Table A-2. Cell No. 2: Ag thin film reference electrode- Emf versus time and standard deviation (STDEV) of emf for 496 ppm SO_2 in air at 535 °C. 159
Table A-3. Cell No. 2: Ag thin film reference electrode - Emf versus flow rate and standard deviation (STDEV) of emf in air at 535 °C. 160
Table A-4. Cell No. 3: Ag thick film reference electrode - %Variance from theory versus time for 100 to 2400 ppm SO_2 in air at 535 °C. 160
Table A-5. Cell No. 3: Ag thick film reference electrode - Emf versus [SO_2] and standard deviation (STDEV) from 100 to 2400 ppm SO_2 in air at 525 °C. 164
Table A-6. Cell No. 4: Composite thick film reference electrode - Emf versus [SO_2] and standard deviation (STDEV) of Emf for 100-2400 ppm SO_2 in air at 535°C. 165
Table A-7. Cell No. 4: Composite thick film reference electrode - Emf versus [SO_2] and standard deviation (STDEV) of emf for 10-496 ppm SO_2 in air at 535 °C. 165
Table A-8. Cell No. 4: Composite thick film reference electrode - Emf versus [SO_2] and standard deviation (STDEV) of emf for 5.4-95.4 ppm SO_2 in air at 535 °C. 167
Table A-9. Cell No. 4: Composite thick film reference electrode - Emf versus [SO_2] and standard deviation (STDEV) of emf for 0.6-11.6 ppm SO_2 in air at 535 °C. 167

Table A-10. Cell No. 4: Composite thick film reference electrode - Emf versus [SO_2] and standard deviation (STDEV) of emf for 14.4 to 2400 ppm SO_2 in air at 535 °C. 168
Table A-11. Cell No. 4: Composite thick film reference electrode – Emf versus flow rate and standard deviation (STDEV) of emf utilizing 200 ppm SO_2 in air at 535 °C. 169
Table A-12. Cell No. 4: Composite thick film reference electrode - Emf versus flow rate and standard deviation (STDEV) of emf utilizing 50 ppm SO_2 in air at 535 °C. 170
Table A-13. Cell No. 4: Composite thick film reference electrode - Emf versus flow rate and standard deviation (STDEV) of emf utilizing 5 ppm SO_2 in air at 535 °C. 170
Table A-14. Cell No. 5: Thick film solid electrolyte-Emf versus [SO_2] in air at 535°C. 171
Table A-15. Pressure, slope, y-intercept and temperature for sensitivity analysis. 172

List of Figures

Figure 2-1. Ionic conductivity versus temperature. 7
Figure 2-2. Ionic and electronic conductivity domains as a function of oxygen 9
Figure 2-3. Sheet resistance. 10
Figure 2-4. In-line four point probe. 11
Figure 2-5. Guard-ring circuit for ionic conductivity measurements. 12
Figure 3-1. Type I solid electrolyte gas sensor. 16
Figure 3-2. Type II solid electrolyte gas sensor. 18
Figure 3-3. Type IIIa solid electrolyte gas sensor. 22
Figure 3-4. Type IIIb solid electrolyte gas sensor. 24
Figure 3-5. Type IIIc solid electrolyte gas sensor. 25
Figure 5-1. Equivalent circuit for a potentiometric sensor 45
Figure 6-1. Thick film screen and holder. 48
Figure 6-2. Vapour pressure of evaporation materials. 53
Figure 6-3. Evaporation sources 55
Figure 6-4. Evaporator – thin film deposition 56
Figure 6-5. E-beam evaporator 58
Figure 7-1. Variation of $\log(\sigma_{ionic}T)$ versus 1/T*1000 for pure Ag_2SO_4 [64]. 60
Figure 7-2. Conductivity of Ag_2SO_4 (23 m/o) – Li_2SO_4 (77 m/o). 61
Figure 7-3. Phase stability diagram for the Li-S-O system at 808K. 62
Figure 7-4. Phase stability diagram for Ag-S-O system at 808K. 63
Figure 7-5. Ag_2SO_4-Li_2SO_4 phase diagram [68]. 64
Figure 9-1. Construction of thick film reference cell structure. 76
Figure 9-2. Cross-section of proposed Micro-Integrated Sulfur Oxide (MISOX) sensor. 78
Figure 10-1. Inner cell construction. 80
Figure 10-2. Control panel for computer control system – Part I. 81
Figure 10-3. Control panel for computer control system – Part II. 82
Figure 11-1. Cell No. 1: composite reference - construction schematic. 83
Figure 11-2. Cell No. 1: composite reference electrode - Emf versus log (SO_2-ppm) from 94 to 900 ppm SO_2 in air. 85
Figure 11-3. Cell No. 2: thin film reference - construction schematic 86
Figure 11-4. Cell No. 2: Ag thin film reference electrode – Emf versus time at 496 ppm SO_2 in air. 87
Figure 11-5. Cell No. 2: Ag thin film reference electrode - Emf versus flow rate, 496 ppm SO_2. 88
Figure 11-6. Cell No. 3: Ag thick film reference electrode. 89
Figure 11-7. Cell No. 3: Ag thick film reference electrode - %Variance from theoretical values versus time for 100 to 2400 ppm SO_2 in air at 525 °C. 90
Figure 11-8. Cell No. 3: Ag thick film reference electrode - Emf versus log (SO_2 -ppm) from 100 to 2400 ppm SO_2 in air at 525 °C. 91
Figure 11-9. Cell No. 4: Composite reference electrode thick film structure. 92
Figure 11-10. Cell No. 4: Composite thick film reference electrode - Emf (V) versus log (SO_2-ppm) for 100 to 2400 ppm SO_2 in air at 535 °C. 93
Figure 11-11. Cell No. 4: Composite thick film reference electrode -Emf (V)

versus log (SO_2-ppm) for 10 to 496 ppm SO_2 in air at 535 °C. 95
Figure 11-12. Cell No. 4: Composite thick film reference electrode – Emf (V) versus log (SO_2-ppm) for 59 to 496 ppm SO_2 in air at 535 °C. 96
Figure. 11-13. Cell No. 4: Composite thick film reference electrode – Emf (V) versus log(SO_2-ppm) for 5.4 to 95.4 ppm SO_2 in air at 535 °C 97
Figure 11-14. Cell No.4: Composite thick film reference electrode – Emf (V) versus log(SO_2-ppm) for 0.6 to 11.6 ppm SO_2 in air at 535 °C. 98
Figure 11-15. Cell No. 4: Composite thick film reference electrode – Emf (V) versus log (SO_2-ppm) for 14.4 to 2400 ppm SO_2 in air at 535 °C. 99
Figure 11-16. Cell No. 4: Composite thick film reference electrode – Emf (V) versus log (SO_2-ppm) for 50 to 2400 ppm in SO_2 in air at 535 °C. 100
Figure 11-17. Flow rate dependence utilizing 200 ppm SO_2 in air at 535 °C..... 102
Figure 11-18. Flow rate dependence utilizing 50 ppm SO_2 in air at 535 °C..... 103
Figure 11-19. Flow rate dependence utilizing 5 ppm SO_2 in air at 535 °C..... 104
Figure 11-20. Cell No. 5 Thick film solid electrolyte..... 105
Figure 11-21. Thick film solid electrolyte 106
Figure 11-22. Photograph of the working electrode consisting of a platinum thin film 1000 Å thick deposited on the solid electrolyte substrate – 72X..... 115
Figure 11-23. Photograph of the working electrode consisting of a platinum thin film 1000 Å thick deposited on the solid electrolyte substrate – 1,033X..... 117
Figure 11-24. Photograph of the working electrode consisting of a platinum thin film 1000 Å thick deposited on the solid electrolyte substrate – 5,167X..... 117
Figure 11-25. Energy dispersive x-ray (EDX) analysis of a working electrode – site No. 1, consisting of a platinum thin film 1000 Å thick deposited on the solid electrolyte. 118
Figure 11-26. Energy dispersive x-ray (EDX) analysis of working electrode – site No. 2, consisting of a platinum thin film (1000 Å thick) deposited on the solid electrolyte. 119
Figure 11-27. Photograph of the reference electrode consisting of a platinum thin film (10,000 Å thick) deposited on the Ag:Ag_2SO_4-Li_2SO_4 reference electrode – 3,100X. 120
Figure 11-28. Energy dispersive x-ray (EDX) analysis of the Pt thin film (10,000 Å thick) deposited onto the reference electrode. 121
Figure 11-29. X-ray diffraction pattern: pre-sintered material. 122
Figure 11-30. X-ray diffraction pattern: post-sintered material..... 123
Figure 11-31. X-ray diffraction pattern: post-use material. 124
Figure 12-1. Slope versus temperature and pressure 126
Figure 12-2. Intercept versus temperature and pressure 127
Figure 12-3. Polarization in an oxygen concentration cell. 142
Figure 12-4. Cross section of sensor layers and reactions. 143
Figure 12-5. Phase stability for the Ag-S-O system at 673K. 145
Figure 12-6. Phase stability for the Ag-S-O system at 808K. 146
Figure 12-7. Phase stability for the Ag-S-O system at 873K. 146
Figure 12-8. Emf versus log[SO_2-ppm] at low SO_2 concentrations. 147
Figure 13-1. Cross-sectional view of Ag:Ag_2SO_4-$MeSO_4$ integrated sensor. 155
Figure D-1. Emf (V) versus log [ppm SO_2] 183

List of Symbols

Chapter 2

Symbol	Description	Units
T	Kelvin, thermodynamic temperature	K
e	elementary charge	C
F	Faraday constant	C mole^{-1}
R	gas constant	J K^{-1} mole^{-1}
ρ	resistivity	Ωm
σ_T	total conductivity	Ω^{-1} m^{-1}
q_i	charge on ionic / electronic charge carrier	C
μ_i	mobility of charge carrier	m^2 V^{-1} s^{-1}
c_i	carrier density	charge carriers m^{-3}
I_T	total current	A
a	surface area	cm^2
i_k	current density of species k	A m^{-2}
σ_k	partial conductivity of species k	Ω^{-1} m^{-1}
z_k	charge number	dimensionless
$\tilde{\mu}_k$	electrochemical potential of species k	J mole^{-1}
σ_{ion}	ionic conductivity	Ω^{-1} m^{-1}
A_{exp}	pre-exponential factor	Ω^{-1} m^{-1}
E_{ion}	ionic activation energy	J mole^{-1}
n	vacancy concentration per m^3	m^{-3}
μ_o	vacancy mobility	m^2 V^{-1} s^{-1}
E_m	activation energy for vacancy migration	J mole^{-1}
N	total number of vacancies per m^3	m^{-3}
e'	excess electron	C

$h^{\bullet}$	positive hole	C
O^{2-}	oxygen anion	C
ΔV	measured voltage	V
R_{Ω}	resistance	Ω
R_s	sheet resistance	Ω
$i(t)$	partial current as a function of time	A
$V_e / i(t)$	indicial impedance	$V\ A^{-1}$
$v(t)$	signal as a function of time	cycles sec^{-1}
$V(\omega)$	alternating voltage	V
$V(\omega)/I(\omega)$	ratio of alternating to variable current	$V\ A^{-1}$

Chapter 3

Symbol	**Description**	**Units**
O^{2-}	oxygen anion	C
e'	excess electron	C
P'_{O_2}	partial pressure of oxygen	atm
P''_{O_2}	partial pressure of oxygen	atm
P'_{CO_2}	partial pressure of carbon dioxide	atm
P''_{CO_2}	partial pressure of carbon dioxide	atm
R	gas constant	$J\ K^{-1}\ mole^{-1}$
T	Kelvin, thermodynamic temperature	K
F	Faraday constant	$C\ mole^{-1}$
Au'	gold contact at electrode	V
Au''	gold contact at electrode	V
Pt'	platinum contact at electrode	V
Pt''	platinum contact at electrode	V
P'_{SO_3}	partial pressure of sulfur trioxide	atm

P''_{SO_3}	partial pressure of sulfur trioxide	atm

Chapter 4

Symbol	Description	Units
Ag^+	silver cation	C

Chapter 5

Symbol	Description	Units
δP	variance in pressure	atm
P	pressure	atm
δE	variance in emf	V
n	charge number	dimensionless
F	Faraday constant	C $mole^{-1}$
R	gas constant	J $K^{-1}mole^{-1}$
T	Kelvin, thermodynamic temperature	K
μ''_{X_2}	chemical potential	J mole-1
P''_{X_2}	partial pressure of gas phase	atm
P'_{X_2}	partial pressure of gas phase	atm
α	constant	VK^{-1}
E_a	absolute error	dependent
$\overline{x}$	average	dependent
x_i	accepted value	dependent
$E_{r.e.}$	relative error	dimensionless
E_{random}	random error	dependent
$E_{systematic}$	systematic error	dependent
$STDEV$	standard deviation	dependent
N	number of measurements	dependent

E	cell voltage	V
E_t	cell voltage at time, t	V
t	time	sec
t_{eq}	equivalent time constant	sec

Chapter 6

Symbol	Description	Units
μm	micron	10^{-6} m
p_{evap}	evaporation pressure	Torr
σ	surface tension	N m^{-1}
ΔH_v	enthalpy of evaporation	J mole-1
k	Boltzman constant	J K^{-1}
N	Avogadro number	$mole^{-1}$
T	Kelvin, thermodynamic temperature	K
Γ	rate of evaporated mass from source per unit area per unit time	kg cm^{-2} sec^{-1}
M	molecular weight	gm $mole^{-1}$

Chapter 7

Symbol	Description	Units
σ_{ion}	ionic conductivity	Ω^{-1} m^{-1}
$(\sigma T)_o$	pre-exponential factor	K Ω^{-1} m^{-1}
E_{ion}	ionic activation energy	J $mole^{-1}$
k	Boltzmann constant	J K^{-1} $mole^{-1}$
T	Kelvin, thermodynamic temperature	K
i_x	electrical current density of electrons	A m^{-2}

	in x-direction	
Δq	change in charge	C
A	area	m^2
Δt	increment of time	second (sec)
δE_x	applied electrical field	V
e	elementary charge	C
v_{dx}	velocity of electrons	m sec^{-1}
$N_{electrons}$	number of electrons	dimensionless
v_{xi}	velocity of i^{th} electron	m sec^{-1}
$n_{electrons}$	number of electrons per unit volume	electrons m^{-3}
V	volume of material	m^3
Δx	electron movement	m
m_e	mass of electron	C
u_{xi}	velocity of electron i in x-direction after collision	m sec^{-1}
$\overline{t-t_i}$	average free time between collisions	sec
τ	mean free time between collisions	sec
μ_d	drift velocity of electron	m sec^{-1}
const	temperature independent constant	K sec
ρ	resistivity	Ω m
ρ_T	resistivity at temperature, T	Ω m
σ_T	conductivity at temperature, T	Ω^{-1} m^{-1}
a	temperature independent constant	Ω m K^{-1}
ρ_R	residual resistivity	Ω m
α_o	temperature coefficient of resistivity	K^{-1}
T_o	reference temperature, typically 273K	K
ρ_o	resistivity at reference temperature	Ω m
$\delta\rho$	change in resistivity	Ω m

δT	change in temperature	K

Chapter 8

Symbol	Description	Units
E	cell voltage, electromotive force	V
E^o	standard cell voltage, electromotive force	V
P_{O_2}	partial pressure of oxygen	atm
P_{SO_3}	partial pressure of sulfur trioxide	atm
$P_{SO_{2(in)}}$	partial pressure of sulfur dioxide input	atm
$a_{Ag_2SO_4}$	activity of silver sulfate	dimensionless
k_p	equilibrium constant	$atm^{-1/2}$

Chapter 11

Symbol	Description	Units
$[SO_2]$	concentration of SO_2	atm
$\bar{a}_{Ag_2SO_4}$	activity of silver sulfate	dimensionless
T.P.B.	triple point boundary	m

Chapter 12

Symbol	Description	Units
E	cell voltage	V
E^o	standard cell voltage	V
R	gas constant	$J\ K^{-1}\ mole^{-1}$
F	Faraday constant	$C\ mole^{-1}$

T	Kelvin, thermodynamic temperature	K
ΔE	shift in voltage	V
E°_{exp}	measured experimental cell voltage	V
$E^{\circ}_{theoretical}$	theoretical cell voltage	V
$P^{\circ}_{O_2}$	partial pressure of oxygen	atm
$P^{'}_{O_2}$	partial pressure of oxygen	atm
$P^{\circ}_{SO_3}$	partial pressure of sulfur trioxide	atm
$P^{'}_{SO_3}$	partial pressure of sulfur trioxide	atm
δ_1	mass diameter of gas species 1	nanometer (nm)
δ_2	mass diameter of gas species 2	nanometer (nm)
D_{12}	ordinary diffusion coefficient	$m^2\ sec^{-1}$
D_T	thermal diffusion coefficient	$m^2\ sec^{-1}$
f_1	volume of heavier gas species 1	m^3
f_2	volume of heavier gas species 2	m^3
k_T	thermal diffusion ratio	dimensionless
$[c_1]_2$	concentration of gas species 1 at location 2	atm
$[c_1]_1$	concentration of gas species 1 at location 1	atm
α_T	thermal diffusion constant	atm^{-2}
c_1	initial concentration of gas species 1	atm
c_2	initial concentration of gas species 2	atm
T_2	temperature in Kelvin at hot zone	K
T_1	temperature in Kelvin at cool zone	K
R_T	thermal separation ratio	dimensionless
Δc_1	change in concentration of gas species 1	atm
α_{12}	thermal diffusion constant for gas species 1 and 2	atm^{-2}

α_{13}	thermal diffusion constant for gas species 1 and 3	atm^{-2}
c_3	initial concentration of gas species 3	atm
Δc_{O_2}	change in oxygen concentration	atm
$\left[c_{O_2}\right]_2$	oxygen concentration at hot zone	atm
$\left[c_{O_2}\right]_1$	oxygen concentration at cool zone	atm
$\alpha_{O_2\text{-}N_2}$	thermal diffusion constant O_2-N_2	atm^{-2}
c_{N_2}	concentration of N_2	atm
$\alpha_{O_2\text{-}SO_3}$	thermal diffusion constant for O_2-SO_3	atm^{-2}
c_{O_2}	concentration of oxygen	atm
$\left[\alpha_T\right]_i$	thermal diffusion constant for species I	dimensionless
M_i	molecular weight of species i	gm $mole^{-1}$
M_{i+1}	molecular weight of species i	gm $mole^{-1}$
Δc_{SO_3}	change in SO_3 gas concentration	atm
t_{ion}	ionic transference number	dimensionless
ΔG_f^o	standard free energy of formation	J $mole^{-1}$

Chapter 1: Introduction

In all facets of industrial processes, chemical sensors, which can measure real time operational parameters, are becoming of increased importance. Sensors are required for measurement and control of physical and chemical phenomena, of which chemical sensors are utilized in numerous applications. These applications include analytical equipment, chemical processes, food industry, environmental control, and biomedical applications. Sensory detection of oxidic gases such as NO, NO_2, NO_x, CO_2, and SO_2 has become important for protection of both global and local environments. With respect to chemical sensors, electrochemical sensors have the advantage of converting the chemical concentrations directly into an electrical signal. In addition, if solid electrolyte or superionic solid materials are utilized, the sensor can be assembled in an all solid-state form.

Sulfur dioxide and trioxide (SO_2/SO_3) are the most important compounds defining the acidic properties of earth's atmosphere. They are emitted in large quantities by the combustion of fossil fuels (coal and oil) and subsequently oxidized into sulfuric acid and sulfates. The sensor technology reported here is suitable for mass production of an inexpensive and compact atmospheric or industrial chemical sensor for pollution, corrosion and process control. Complementary to the development of selective, solid-state chemical sensors is the application of microelectronic fabrication techniques, ideally suited for mass production. Solid-state ionic conductors are amenable to these methods of fabrication, through the deposition of thin and/or thick films. A thin film is defined as having a thickness of from 50 to several thousand angstroms but less than 5 μm. Thin films are typically deposited on a substrate via vacuum deposition in combination with either an additive or a subtractive photolithography process. In comparison, a thick film has a thickness of between 5-50 μm and is deposited through a silk or stainless steel screen by selective deposition of a paste or slurry.

Through the experience gained in constructing this SO_2/SO_3 sensor, additional sensors for the detection of nitrous oxides and carbon oxides, for instance, could also be fabricated. Other solid electrolytes displaying oxygen, silver, sodium, potassium, hydrogen, or copper conduction are also suitable candidates for miniaturization and integration. The ultimate goal of this work is to construct a reliable, miniaturized and integrated SO_2/SO_3 chemical sensor.

This thesis reports on progress in the fabrication and testing of materials and deposition techniques for construction of a sulfur oxide chemical sensor. This sensor directly measures SO_2/SO_3 as opposed to many electrochemical gas sensors that require calibration curves. In relation to fabrication of the sensor, several designs were examined including: solid electrolytes fabricated as composite mixtures of Ag_2SO_4-Li_2SO_4 both in bulk form and as thick films, working electrode structures consisting of Pt thin films and Pt gauze, reference electrodes as composite mixtures of Ag: Ag_2SO_4-Li_2SO_4 both in bulk form and as thick films, and reference electrodes consisting of thin or thick films of pure Ag.

The sensor was shown to accurately measure SO_2/SO_3 concentrations over a wide range from 10 to 2400 ppm of SO_2 in air for several months, without degradation in the signal strength. This is primarily due to the use of a highly stable two-phase solid electrolyte. From the successful completion of fabrication and application of thick and thin films in this work, it is now possible to produce a miniaturized sulfur oxide sensor. The miniaturization of this sensor would provide the following benefits:

- lower cost per sensor unit as mass production would be possible with minimal material
- reliability would be enhanced through integration of sensor components
- the use of thin and thick films would significantly reduce sensor response time
- power consumption would be dramatically lowered, especially if the active sensing area were to be fabricated onto an isolated micro-machined heater structure

In addition, it would be possible to apply this technology to a wide range of additional gas sensors, e.g., O_2, CO/CO_2, NO_x, Cl_2, and H_2 . With the development of new types of solid electrolytes and auxiliary electrodes, gas sensors could be created that would be able to detect gases not possible at this time. In particular the development of a solid electrolyte capable of ionic conduction of sulfide ions would be highly beneficial for both the detection of sulfur-based gases and in the electrochemical decomposition of hydrogen sulfide into hydrogen and sulfur. The resulting hydrogen could be utilized in the production of electric power via fuel cell technology.

Chapter 2: Potentiometric Chemical Sensors

Ionic Conductivity

In most ionic solids, the ions are trapped in lattice sites and despite the fact that these ions continuously vibrate, ions rarely have enough thermal energy to escape from lattice sites. If the ions are capable of moving into adjacent lattice sites, this would permit either ionic conduction or diffusion. At higher temperatures, ionic conduction is more likely to occur since ions have greater thermal energy and, therefore, vibrate more vigorously. There is also a higher intrinsic defect concentration at higher temperatures.

It has been discovered that a relatively small group of solids called solid electrolytes, fast ion conductors, or superionic conductors, possess ions which can move very rapidly. These materials have unique crystal structures with open tunnels or layers in which the mobile ions can move through. For example, the conductivity resulting from Na^+ ion migration in $\beta-$alumina is in the range of 10^{-3} S cm^{-1} at 25 °C, which is comparable to liquid electrolytes.

In a perfect crystal all atoms are at rest in their correct lattice positions; such a perfect crystal can be obtained theoretically only at absolute zero. At temperatures above absolute zero, atoms vibrate which in itself can be considered a defect, but a number of atoms are inevitably misplaced from their lattice positions. For some crystals the number of defects can be quite low (i.e., $\ll 1$ per cent) such as with high purity diamond or quartz. In other crystals high defect concentrations may be present due to a reduction in free energy from the creation of defects. These crystal defects are divided into two groups:

- Stoichiometric defects – in which the crystal composition is unchanged on introducing defects

- Non-stoichiometric defects – where defects are a consequence of a change in composition

In addition, the defects can be classified according to their size and shape of the defect as either:

- Point defects – involving only one atom or lattice site, consisting of vacancies or interstitials, with the surrounding atoms somewhat perturbed
- Line defects (dislocations) – dislocations which are effectively point defects in two and three dimensions
- Planar defects – where whole layers in a crystal are defective

Two parameters can be modified to increase the conductivity of a solid, either the carrier concentration and/or the mobility. The carrier concentration consisting of ionic defects can be increased by the following methods:

- by doping, or adding aliovalent impurities (i.e., additives with a different valence state than the host material), which require the generation of ionic defects opposite in charge to maintain electrical neutrality
- by deviation from stoichiometry through reaction with a gas phase that results in a reduction or oxidation of the material and the formation of excess vacancies or interstitials. This process also simultaneously produces electronic species, resulting in mixed ionic-electronic conduction.

Electrical Conductivity

The total electrical conductivity (σ_T) of a solid is the sum of the partial conductivities of the ionic and electronic charge carriers. Total conductivity is defined by the following equation:

$$\sigma_T = \sum q_i \mu_i c_i \qquad (2.1)$$

where q_i is the charge, μ_i is the mobility and c_i is the carrier density.

The total cell current is obtained by multiplying the total current density by the surface area of the electrode. The cell current is equal to the individual current densities, (i_k), for the charge carrier k, which are proportional to the corresponding conductivity and electrochemical potential gradient. This relationship is defined by:

$$I_T = a\sum_k i_k = -a\sum_k \frac{\sigma_k}{z_k F}\left(\frac{\partial}{\partial x}\right)\tilde{\mu}_k \qquad (2.2)$$

where I_T is the total current of the cell, a is the surface area in cm^2, σ_k the conductivity of species k, z_k the charge number on species k, F is the Faraday constant and $\tilde{\mu}_k$ is the electrochemical potential of species k.

Typically the temperature dependence of ionic conductivity, σ_{ion}, is described by the Arrhenius equation as:

$$\sigma_{ion} = A_{exp}\exp\left(\frac{-E_{ion}}{RT}\right) \qquad (2.3)$$

where A_{exp} is the pre-exponential factor consisting of several constants including the vibrational frequency of the mobile ions, E_{ion} is the activation energy for ion migration, R the gas constant and T the temperature in Kelvin.

It is customary to produce a graph of $\log_e \sigma$ versus 1/T for an ionic material resulting in a straight linear line of slope of the general form –E/R as shown in Figure 2.1.

In the extrinsic region, conductivity depends on both the vacancy concentration and vacancy mobility as given by:

$$\sigma_{ion} = nze\mu_o \exp\left(\frac{-E_m}{RT}\right) \qquad (2.4)$$

where n is the vacancy concentration or charge carrier concentration, z is the valence, e the charge on the current carrier (vacancy), E_m is the activation energy for vacancy migration, R the gas constant, T the temperature in K and where μ_o is the pre-exponential term in the equation:

$$\mu_i = \mu_o e^{-E_M / RT} \tag{2.5}$$

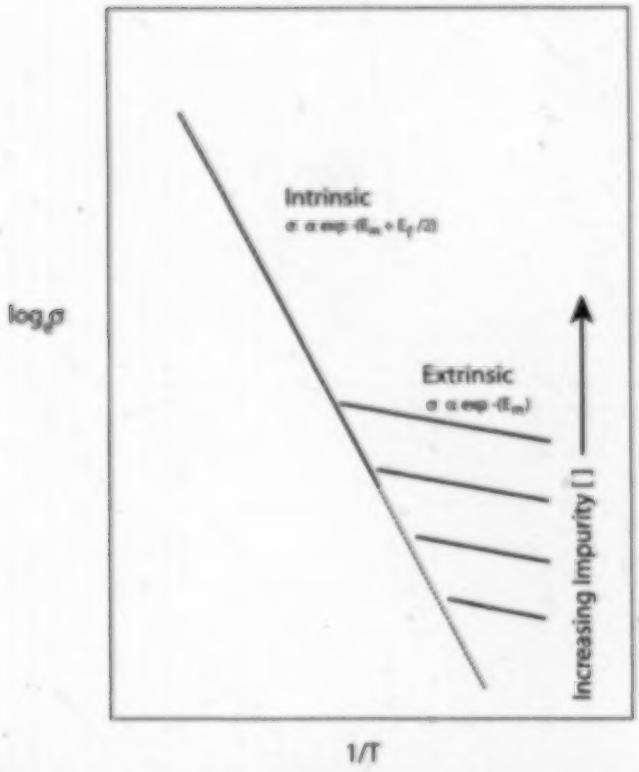

Figure 2-1. Ionic conductivity versus temperature.

As the concentration of dopant is increased, the vacancy concentration also increases followed by an increase in the ionic conductivity of the solid electrolyte. There is a significant increase in the conductivity of the extrinsic form of the electrolyte in comparison to the intrinsic version of the electrolyte, without doping, at the same temperature. This phenomena is displayed in Figure 2-1 in the extrinsic region of conductivity.

In the high temperature region the thermally induced vacancy concentration is greater than that created by the dopant. The concentration of vacancies, n, is given by:

$$n = N\exp\left(\frac{-E_f}{2RT}\right) \tag{2.6}$$

where N is the total number of ions in the crystal, and E_f is the activation energy of vacancy formation.

Therefore, it follows that the conductivity in the intrinsic region is given by:

$$\sigma_{ion} = Ne\mu_o \exp\left(\frac{-E_m}{RT}\right)\exp\left(\frac{-E_f}{2RT}\right) = A_{exp}\exp\left(-\frac{E_m + E_f/2}{RT}\right) \tag{2.7}$$

The transition between ionic conduction and electronic conduction (semiconductor) can be induced in the same material. If it is an oxide ion conductor such as ZrO_2 based solid electrolytes, this transition can be induced by varying the partial pressure of O_2 in the surrounding atmosphere (see Figure 2-2). This is typical of materials such as yttria-stabilized zirconia (YSZ) which possess an electrolytic domain over which the ionic transference number, t_i, is unity. In fact, measurement of constant conductivity over a range of partial gas pressure is a good indication of ionic conductivity. With an oxide ion conductor, upon varying the oxygen pressure there is a tendency for O_2 molecules to absorb or desorb from the solid electrolyte. At high oxygen pressures the material becomes a positive hole (p-type) conductor according to:

$$O_2 \rightleftharpoons 2O^{2-} + 4h^{\bullet} \tag{2.8}$$

Whereas at low oxygen pressures the material becomes an excess electron (n-type) conductor according to:

$$2O^{2-} \rightleftharpoons O_2 + 4e' \tag{2.9}$$

The discussion to this point relates to solid electrolytes which have high ionic conductivity but which are insulators electronically. In practical use as batteries, sensors and fuel cells, electronic conductivity must be avoided as it will result in

internal short circuits and, therefore, a loss in performance and accuracy. In materials that are mixed conductors, both ionic and electronic conduction occur simultaneously; these materials finding application as electrodes.

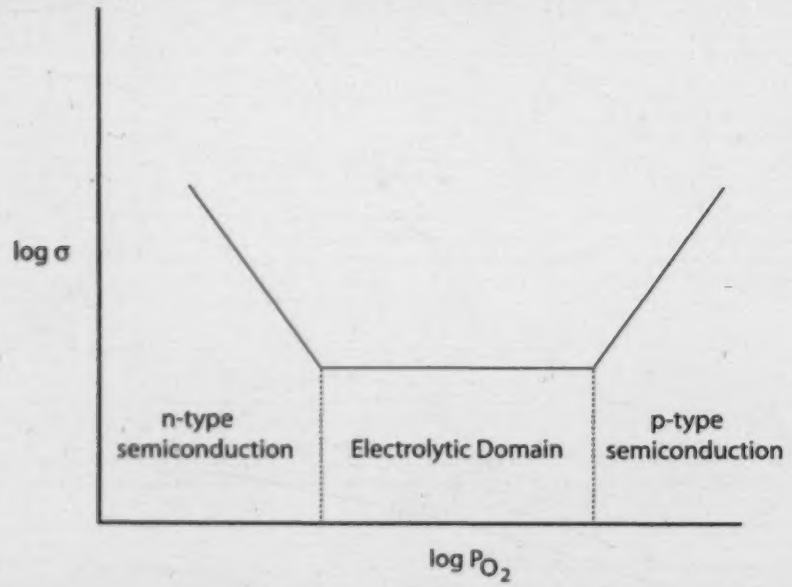

Figure 2-2. Ionic and electronic conductivity domains as a function of oxygen partial pressure.

Measurement of Conductance

The ionic conductivity in an electrolyte with negligible electronic conduction ($i_{ionic} \cong i_{ion}$) may be determined by using Ohm's law, provided that non-polarizable reversible electrodes are utilized. These electrodes will ensure the unimpeded delivery of the mobile ions from one side to the other side of the sample. This is accomplished through the use of separate voltage probes in the form of identical electronic leads connected to the electrolyte at positions separated by distance L. With this configuration, the ionic conductivity is given by:

$$\sigma_{ion} = -\frac{iL}{\Delta V} \tag{2.10}$$

where σ_{ion} is the ionic conductivity, i the measured current, L the distance between the electrical probes, and ΔV the measured voltage.

The technique known as the four-point dc technique [3] is commonly used for measurement of the conductivity of thin films produced in the fabrication of semiconductor products. The resistance/conductivity of thin films is measured according to sheet resistance, which is defined as the resistance of a rectangular shaped section of film as shown in Figure 2-3.

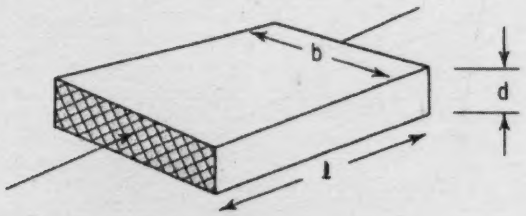

Figure 2-3. Sheet resistance.

The resistance of a rectangular shape is given by:

$$R_{\Omega} = \frac{\rho}{d}\frac{l}{b} \tag{2.11}$$

where ρ is the resistivity, l is the length, b the width and d the thickness of the rectangular section.

If $l = b$ then equation 2.11 becomes:

$$R_{\Omega} = R_s = \frac{\rho}{d} \tag{2.12}$$

With this formula the sheet resistance R_s, of one square of film is independent of the size of the square, depending only on the resistivity and thickness of the thin film. The sheet resistance is expressed in ohms per square. If the thickness of the film is known then the resistivity of the thin film is calculated by:

$$\rho = d\,R_s \tag{2.13}$$

The four-point probe method allows measurement of sheet resistance without fabrication of a rectangular thin film structure. The most common form of this technique is the in-line four-point probe as displayed in Figure 2-4.

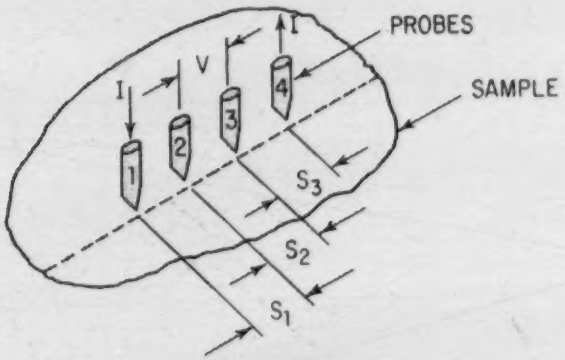

Figure 2-4. In-line four point probe.

When the probes are placed on a material of semi-infinite volume, the resistivity is given by:

$$\rho = \frac{\Delta V}{I} \frac{2\Pi}{1/s_1 + 1/s_3 - 1/(s_1+s_2) - 1/(s_2+s_3)} \tag{2.14}$$

When $s_1 = s_2 = s_3$, this reduces to:

$$\rho = \frac{\Delta V}{I} 2\Pi s \tag{2.15}$$

If the material on which the probes are placed is an infinitely thin slice resting on an insulating support, equation 2.15 becomes:

$$\rho = \frac{\Delta V}{I} \frac{d\Pi}{\ln 2} \tag{2.16}$$

which can be arranged to:

$$R_s = \frac{\rho}{d} = 4.532 \frac{\Delta V}{I} \tag{2.17}$$

High Impedance Conductivity Measurements

The measurement of ionic conductivity in high impedance solid electrolytes results in specific experimental challenges. The presence of very small leakage currents returning to ground potential via sensitive elements in the detector circuit can result in large errors in the measured conductivity. Even faint conductivities due to nanoampere or picoampere leakage currents through otherwise excellent insulators can enter the amplifier circuit and create error in measurement. Through the addition of a guard-ring circuit as shown in Figure 2-5 ground current leakage problems can be avoided or significantly reduced.

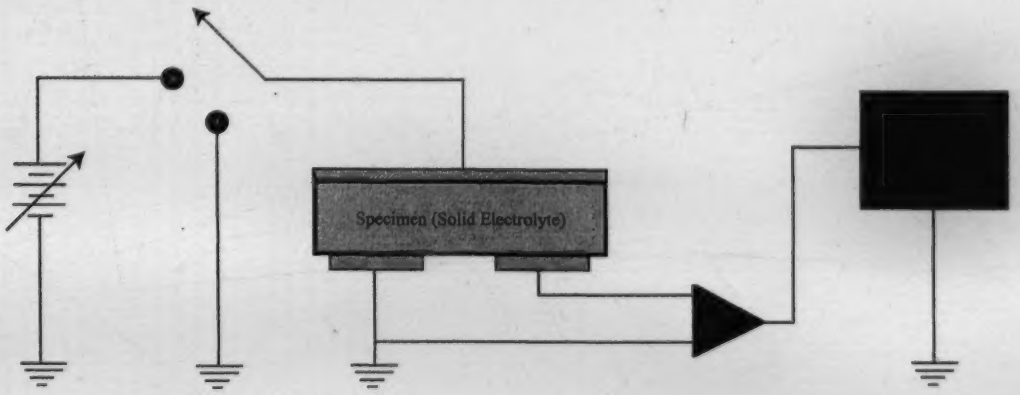

Figure 2-5. Guard-ring circuit for ionic conductivity measurements.

Impedance Spectroscopy

Determining the electrical conductance by DC measurements gives the sum of electronic contributions of electrode contacts, grains, intergrain boundaries, etc. By utilizing impedance spectroscopy it is possible to discriminate between these individual contributions. Impedance spectroscopy is used extensively in solid state ionics to separate bulk and interfacial contributions consisting of grain-boundary and electrode effects. It may be used to investigate the dynamics of bound or mobile charges in the bulk or interfacial regions of any kind of solid or liquid material. This

includes ionic, semiconducting, mixed electronic-ionic, or insulator (dielectric) materials. The ionic solid electrolyte material can be amorphous, polycrystalline or a single crystal.

For the evaluation of electrochemical behaviour of electrode or electrolyte material, electrical measurements are usually made with cells having two identical electrodes (in the form of a circular cylinder or rectangular shape) applied to the faces of a sample. The properties of the electrode-sample material are assumed not to change over time. Then an electrical stimulus consisting of a known voltage or current is applied to the electrodes and a response consisting of the resulting current or voltage is measured. There are three different types of electrical stimulus utilized in impedance spectroscopy consisting of:

- A step function of voltage is applied with the resulting time varying current $i(t)$ measured. The ratio defined by $V_o / i(t)$ is called the indicial impedance and quantifies the impedance resulting from the step function voltage perturbation. However, the results are usually Fourier-transformed into the frequency domain providing frequency dependent impedance. This transformation is only valid when the absolute value of V_o is small and the system response is linear. The advantage of this approach is that it is easily accomplished experimentally and that the independent variable, voltage, controls the rate of the electrochemical reaction at the interface. However, the frequency is not directly controlled so the impedance may not be well determined over the desired frequency range.

- The second technique is to apply a signal $v(t)$ composed of random or white noise to the interface and measure the resulting current. These results are also generally Fourier-transformed into the frequency domain to acquire the impedance. This technique is restricted to frequencies between 50-100 kHz, with application of Fourier transforms below 10 Hz being difficult. The upper

end of the frequency range is dictated by the speed of analog to digital conversion computer equipment which is steadily increasing every year.

- The third approach, which is the most commonly utilized technique, consists of measuring the impedance directly in the frequency domain through the application of a single-frequency voltage to the interface and measuring the phase shift and amplitude, or real and imaginary parts, of the resulting current at that frequency. The most significant advantage is that commercially available equipment can measure the impedance as a function of frequency from 1 mHz to 1 MHz. Therefore, the experimentalist can examine the frequency range of most interest in relation to the application. It is also possible to combine the two previous techniques with this approach to generate other forms of stimulus. The most important of these techniques, ac polarography, combines a linearly varying unipolar transient signal with a much smaller single-frequency sinusoidal signal [4].

This electrical stimulus consists of a small alternating voltage ($V(\omega)$) applied to the sample and the induced current is measured. The impedance which is derived from $\frac{V(\omega)}{I(\omega)}$ is evaluated as a function of the alternating-current frequency. These data are plotted on complex impedance diagrams (i.e., Nyquist or Cole-Cole plots) where the imaginary part (Z'') is plotted versus the real part of the impedance (Z'). Depending on the overall equivalent electrical characteristics of the cell, different plots are obtained. For example, the response of an ideal parallel circuit consisting of resistance R and capacitance C appears as a semi-circle centered on the real axis. The resistance of the circuit is calculated by measuring the diameter of the semi-circle, whereas C can be calculated from the maximum frequency of the semi-circle.

Chapter 3: Potentiometric Gas Sensors - Classification System

A solid state electrochemical sensor consists of a membrane of the solid electrolyte (an ionic conductor) with a pair of electrodes (i.e., cathode and anode) which are electronic conductors. From these fundamental structures a classification system can be used to describe a series of sensor configurations. This definition will be applied to potentiometric sensors otherwise known as galvanic sensors, which are divided into equilibrium and mixed-potential types. The classification system to be presented will be for equilibrium potentiometric sensors.

Type I Solid Electrolyte Gas Sensor

Type I gas sensors are constructed from a solid electrolyte in which the mobile ion is the same as that derived electrochemically from the gas phase. An example of this type would be an oxygen chemical sensor utilizing an O^{2-} ionic conductor such as yttria stabilized zirconia (YSZ). This sensor forms an oxygen concentration cell as follows:

$$O_2, Pt' \,|\, YSZ \,|\, Pt'', O_2 \tag{3.1}$$

At the three-phase contact zone consisting of the solid electrolyte (YSZ), electrode (Pt) and the gas phase (O_2) the following electrochemical reaction takes place:

$$O_2 + 4e' \rightarrow 2O^{2-} \tag{3.2}$$

This reaction links the mobile ion species, O^{2-}, to the gas phase, O_2, as stated previously. When the partial pressures of oxygen, P'_{O_2} and P''_{O_2}, are established at either side of the solid electrolyte at the electrodes, the electrochemical force (emf) is given by the Nernst equation:

$$E = \frac{RT}{4F} \ln \frac{P''_{O_2}}{P'_{O_2}} \tag{3.3}$$

where F is the Faraday constant, R is the gas constant and T the temperature in K. If one of the oxygen partial pressures is known, then the other partial pressure can be determined using equation 3.3.

In Figure 3-1 a schematic of the cell structure for a Type I solid electrolyte gas sensor (in reference to a A^+ conductive electrolyte) is provided. For the case of a YSZ oxygen concentration cell the mobile ionic species would be equivalent to B (i.e., mobile species is B^-) with the gas phase and reference activity refering to species B. The double arrows indicates the mobility of the ionic species throughout the electrolyte.

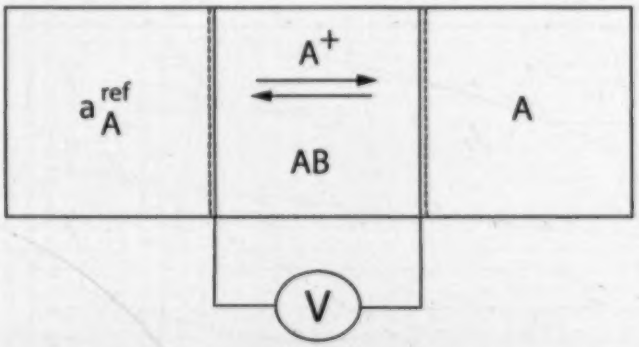

Figure 3-1. Type I solid electrolyte gas sensor.

Type I gas sensors are available for simple gases such as O_2, H_2, Cl_2, and Na vapour, using electrolytic conductors with mobile species consisting of O^{2-}, H^+, Cl^- or Na^+ (see Table 3-1). For the oxidic gases such as CO_2, NO_x and SO_x there are no type I electrolytes available at this time.

Type II Solid Electrolyte Gas Sensor

Type II sensors convert the gas being measured into the immobile ion of the electrolyte. This class of chemical sensors provides a means for detection of CO_2, NO_2 and SO_2 with electrochemical cells consisting of oxy-acids such as K_2CO_3,

$Ba(NO_3)_2$, and Na_2SO_4 (see Table 3-2). For example, to measure CO_2, a chemical sensor can be fabricated with the following configuration:

$$CO_2 - O_2, Au' \,|\, K_2CO_3 \,|\, Au'', CO_2 - O_2 \tag{3.4}$$

In this configuration, the solid electrolyte consists of K_2CO_3 with ionic conduction occurring via K^+ ionic conduction. The gaseous components interact with the electrode, Au, and the electrolyte, K_2CO_3, via the following electrochemical reaction:

$$2K^+ + CO_2 + \tfrac{1}{2}O_2 + 2e' \rightarrow K_2CO_3 \tag{3.5}$$

Table 3-1. Material configuration of Type I chemical sensors.

Configuration	Solid Electrolyte	Gaseous Phase
	ZrO_2-Y_2O_3 (O^{2-})	O_2
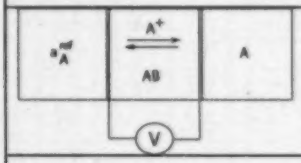	HUO_2PO_4:$4H_2O$ (H^+)	H_2 [5]
	Sb_2PO_5:$2H_2O$ (H^+)	H_2 [6]

In this fashion the gas is converted into the immobile ion of the electrolyte. The emf of a $CO_2 - O_2$ concentration cell is given by:

$$Emf(V) = \frac{RT}{2F} \ln \left\{ \frac{P''_{CO_2} \left(P''_{O_2}\right)^{1/2}}{P'_{CO_2} \left(P'_{O_2}\right)^{1/2}} \right\} \tag{3.6}$$

Table 3-2. Material configuration of Type II chemical sensors.

Configuration	Solid Electrolyte	Gaseous Phase
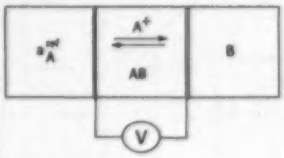	Li_2SO_4 (Li^+)	SO_x [7]
	Na_2SO_4 (Na^+)	SO_x [8]
	$Ba(NO_3)_2$-AgCl (Ag^+)	NO_2 [9]
	K_2CO_3 (K^+)	CO_2 [10]
	$SrCl_3$-KCl (K^+)	Cl_2 [11]

If $P'_{O_2} = P''_{O_2}$ it follows that the emf for the cell is given by:

$$Emf\,(V) = \frac{RT}{2F} \ln\left\{\frac{P''_{CO_2}}{P'_{CO_2}}\right\} \tag{3.7}$$

In Figure 3-2 a schematic of the cell structure for a Type II solid electrolyte gas sensor is displayed.

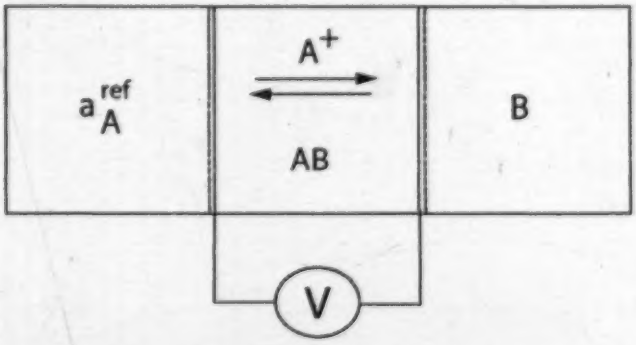

Figure 3-2. Type II solid electrolyte gas sensor.

The sulfur oxide chemical sensor in this work is classified as a Type II sensor, consisting of a solid electrolyte fabricated with Ag_2SO_4–Li_2SO_4, and a reference electrode consisting of either pure Ag or a mixture of Ag and Ag_2SO_4–Li_2SO_4, along with a working electrode fabricated with a Pt gauze or thin film. In the gas flow inlet quartz tube upstream of the working electrode, Pt strips and wire were placed in a quartz chamber for conversion of SO_2 to SO_3 according to the equation:

$$SO_2 + \tfrac{1}{2}O_2 \rightleftharpoons SO_3 \tag{3.8}$$

At the Pt working electrode, equilibrium is established according to the reaction:

$$SO_3 + \tfrac{1}{2}O_2 + 2e' \rightleftharpoons SO_4^{2-} \tag{3.9}$$

Following a Type II chemical sensor displayed in Figure 3-2, the component AB is equivalent to Ag_2SO_4 contained within the solid electrolyte (Ag_2SO_4–Li_2SO_4), B consists of SO_4^{2-} which is derived from the gaseous SO_2 phase, and the mobile ionic species (A^+) is equivalent to Ag^+. The reference in this work consists of pure silver (Ag^0) or Ag mixed with the electrolyte, Ag_2SO_4–Li_2SO_4.

Various electrolytic membranes consisting of metal sulfates such as: $Ag_2SO_4 - K_2SO_4$, $Ag_2SO_4 - Li_2SO_4$, or $Na_2SO_4 - Li_2SO_4 - Y_2(SO_4)_3 - SiO_2$ have been determined to be suitable for measurement of SO_2. There are available a series of isovalent and aliovalent sulfates suitable for use as Type II sensors. The sulfates of the form Me_2SO_4 , in order of highest conductivity to lowest, consist of: Rb_2SO_4, Cs_2SO_4, K_2SO_4, Li_2SO_4, and Na_2SO_4. However, with these electrolytes the reference electrode would be somewhat difficult to fabricate due to the reactivity of the metallic components (Group 1A elements) in air. The next group consists of sulfates of the form MSO_4, in order of highest conductivity to lowest: $MnSO_4$, $CoSO_4$, $NiSO_4$, $ZnSO_4$, $CuSO_4$, $CaSO_4$, $MgSO_4$, $BaSO_4$, and $PbSO_4$. From this group the best choices use metal - metal sulfate reference electrodes with the following compositions: Co-

$CoSO_4$, Ni-$NiSO_4$, Zn-$ZnSO_4$, Cu-$CuSO_4$ or Pb-$PbSO_4$. These reference electrodes are preferred since the metallic components are stable in air. The remaining reference electrodes would require handling of Ba, Ca, Mn, and Mg in an inert atmosphere, due to their reactivity with air and/or moisture. Finally, sulfates of the form $M_2(SO_4)_3$ in order of highest conductivity to lowest, consist of: $Gd_2(SO_4)_3$, $La_2(SO_4)_3$, $Y_2(SO_4)_3$ and $Dy_2(SO_4)_3$. From this group the best choice would require construction of a reference electrode consisting of Gd-$Gd_2(SO_4)_3$. For the remaining choices, La, Y and Dy require an inert atmosphere during assembly, followed by encapsulation for protection from air.

Selection of a sulfate solid electrolyte and sulfate based reference electrode is based on the thermodynamic stability of the solid electrolyte for the intended application, temperature of operation, required ionic conductivity, compatibility with respect to interfacial reactions, and ease of assembly.

Type III Solid Electrolyte Gas Sensor

Type III sensors conform to an electrochemical device of unconventional structure. *This type of sensor consists of an oxy-acid of the gas being measured, which is attached to a solid electrolyte membrane. In this case the solid electrolyte cannot measure the gas concentration without the addition of an auxiliary phase (oxy-acid salt).* This type of sensor has a significant advantage in that the monolithic membrane of an oxy-acid can be replaced by a more conventional and proven solid electrolyte, such as NASICON, a ZrO_2 based electrolyte, or β-alumina, etc. In this situation the solid electrolyte can detect the intended gas with the addition of an auxiliary electrode consisting of a sulfate, carbonate, or nitrite/nitrate.

Type III sensors were initially developed by Maruyama and Saito [12] using an electrochemical cell constructed with NASICON ($Na_3Zr_2Si_2PO_{12}$), a Na^+ conductor, for the measurement of SO_2 concentrations. It was observed that when NASICON was exposed to SO_2, Na_2SO_4 formed spontaneously on the surface. Therefore, in this

case the auxiliary oxyacid consists of Na_2SO_4. The configuration of the cell is of the form:

$$SO_2 - O_2 - SO_3, Na_2SO_4, Pt' \,|\, Nasicon \,|\, Pt'', Na_2SO_4, SO_2 - O_2 - SO_3 \qquad (3.10)$$

In this situation, SO_3 is produced up to its equilibrium concentration through the oxidation of SO_2 in the quartz catalyzing chamber and at the Pt electrodes. It follows that the electrochemical reaction for both electrodes consists of:

$$2Na^+ + SO_3 + \tfrac{1}{2}O_2 + 2e' \rightleftharpoons Na_2SO_4 \qquad (3.11)$$

Therefore, this cell would measure the concentration SO_3 via the overall cell reaction as given by:

$$E = \frac{RT}{2F} \ln \left\{ \frac{P''_{SO_3} \left(P''_{O_2}\right)^{1/2}}{P'_{SO_3} \left(P'_{O_2}\right)^{1/2}} \right\} \qquad (3.12)$$

In these devices the solid electrolyte membrane consists of NASICON in which the mobile ion is Na^+, combined with an auxiliary phase consisting of Na_2SO_4, with the same mobile ion Na^+. Typically, Type III sensors are further classified into three subtypes according to the relation between the mobile ions of the solid electrolyte and the auxiliary phase.

Type IIIa Solid Electrolyte Gas Sensor

For a Type IIIa sensor the mobile ion (i.e., A^+) contained in the solid electrolyte and in the auxiliary phase are the same (see Figure 3-3). In Table 3-3 some typical material configurations for a Type IIIa gas sensor are shown. Included in this table are some previously examined sensor configurations along with some additional proposed systems. These systems would consist of a Li^+ based fast ionic conductor

with Li_2SO_4 as the auxiliary, or a Ag^+ based fast ionic conductor with Ag_2SO_4 as the auxiliary.

It is important to choose a solid electrolyte that can be fabricated with high enough density to ensure gas tightness. The auxiliary phase also needs to be dense and gas tight so as to ensure proper coupling of the measured gas phase through the auxiliary to the solid electrolyte. As will be discussed later, fabrication of sulfate based electrolytes and auxiliary electrodes is crucial in implementation of these types of sensors.

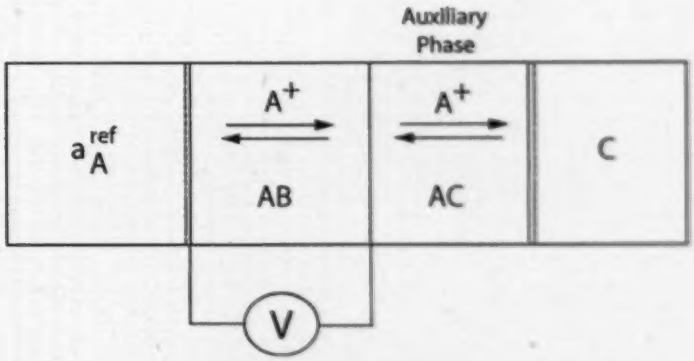

Figure 3-3. Type IIIa solid electrolyte gas sensor.

Type IIIb Solid Electrolyte Gas Sensor

For a Type IIIb sensor the mobile ions in the solid electrolyte and the auxiliary electrode are different but have the same valence. As shown in Figure 3-4 the mobile ions in the solid electrolyte and auxiliary electrodes are depicted as A' and A'', respectively. Presented in Table 3-4 are some typical material configurations for Type IIIb gas sensors.

In addition, it would be possible to construct Type IIIb sensors for the detection of SO_x utilizing sulfates in the auxiliary with the form Me_2SO_4 (the mobile ions are different but must have the same charge). As previously discussed there are several

sulfates from this group which possess high ionic conductivity (at 250-400 °C) which would be ideal candidates for this type of sensor. In addition, there are various techniques available for the deposition of thin films of NASICON [13-25].

Table 3-3. Material configuration of Type IIIa chemical sensors.

Configuration	Solid Electrolyte	Auxiliary Phase	Gaseous Phase
	β-Alumina (Na^+)	Na_2SO_4 (Na^+)	SO_x [26]
	β-Alumina (Na^+)	$NaNO_3$ (Na^+)	NO_2 [27]
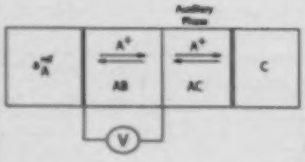	NASICON (Na^+)	Na_2CO_3 (Na^+)	CO_2 [28]
	Li^+ Conductor	Li_2CO_3 (Li^+)	CO_2 [29]
	Li^+ Conductor	Li_2SO_4 (Li^+)	SO_x (proposed)
	Ag^+ Conductor	Ag_2SO_4	SO_x (proposed)
	"fast" cation conductor (Me_2SO_4, Me_2SO_4, or MSO_4)	with matching cation conducting sulfate (Me_2SO_4, Me_2SO_4, or MSO_4)	SO_x (proposed)
	LaF_3 (La^{+3})	LaOF (La^{+3})	O_2 [29]

Type IIIc Solid Electrolyte Gas Sensor

For a Type IIIc sensor the mobile ions in the solid electrolyte and the auxiliary electrode are different and also have a different charge. As depicted in Figure 3-5 the mobile ions in the solid electrolyte and auxiliary electrode are depicted as B^- and A'^+, respectively. Presented in Table 3-5 are some typical material configurations for Type IIIc gas sensors. This an extremely flexible form of a gas sensor, in that the solid electrolyte typically consists of ZrO_2 based electrolytes which are available commercially with high gas tightness. It is also possible to deposit thin films of ZrO_2-Y_2O_3, via sputtering, sol-gel, screen printing or electrophoretic deposition processes [30]. This would be advantageous in the development of micro-machined gas sensors. The solid electrolyte thin film would be combined with an auxiliary sulfate(s) phase from the groups consisting of either Me_2SO_4, MSO_4, or $M_2(SO_4)_3$ for detection of SO_x. Since the mobile ions in the solid electrolyte and the auxiliary phase can be of different charge and different type, this allows considerable flexibility with sensor configurations.

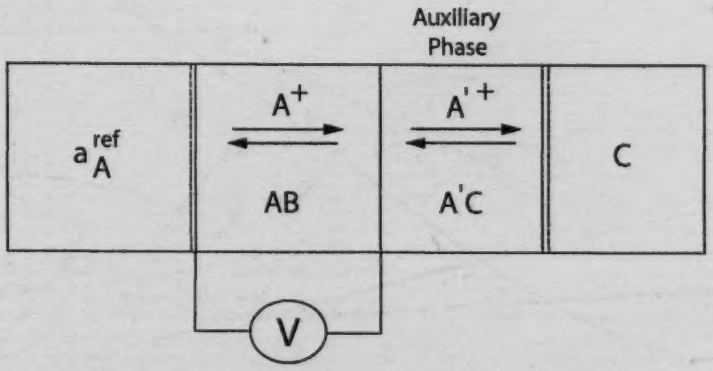

Figure 3-4. Type IIIb solid electrolyte gas sensor.

Table 3-4. Material configuration of Type IIIb chemical sensors.

Configuration	Solid Electrolyte	Auxiliary Phase	Gaseous Phase
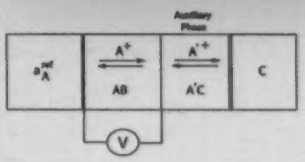			
	NASICON (Na^+)	Li_2CO_3 (Li^+)	CO_2 [31]
	NASICON (Na^+)	$Ba(NO_3)_2$ (Ba^+)	NO_x [32]
	NASICON (Na^+)	Me_2SO_4 (same valence charge – different mobile ion)	SO_x (proposed - Eastman

Figure 3-5. Type IIIc solid electrolyte gas sensor.

Table 3-5. Material configuration of Type IIIc chemical sensors.

Configuration	Solid Electrolyte	Auxiliary Phase	Gaseous Phase
	ZrO_2-MgO (O^{2-})	Li_2SO_4 (Li^+)	SO_x [33]
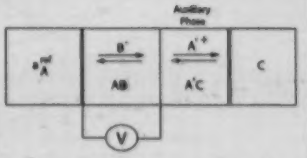	ZrO_2-MgO (O^{2-})	Li_2CO_3 (Li^+)	CO_2 [34]
	ZrO_2-MgO (O^{2-})	$Ba_2(NO_3)_2$ (Ba^{+3})	NO_x [35]
	LaF_3 (F^-)	Li_2CO_3 (Li^+)	CO_2 [36]
	ZrO_2-MgO (O^{2-})	Me_2SO_4, MSO_4, $M_2(SO_4)_3$	SO_x (proposed)

Chapter 4: Literature Review – Sulfur Chemical Sensor Technology

The production of SO_2 gas in industrialized economies results in the acidification of rain due to the formation of sulfuric acid (H_2SO_4) causing a significant negative impact on the environment. Major industrial sources of SO_2 emissions originate from coal-fired power plants, oil and gas production, non-ferrous smelting operations, and diesel engine road vehicles. Methods for detection and measurement of SO_2 in stack gases consisting of chemical analysis (i.e., West-Gaeke coulometric and hydrogen peroxide techniques) and instrument analysis (flame photometric detection and UV fluorescence technique) are considered to be complicated and expensive to operate. Therefore, considerable effort has been expended in finding suitable methods for the continuous detection and monitoring of SO_2 emissions. One of the possible solutions is the development of potentiometric or galvanic cells utilizing solid electrolytes. As measurements can be made in situ, superior accuracy is possible. Sensors based on solid electrolytes have a relatively more complicated design but are more selective to SO_x. In comparison, gas sensors constructed with metal semiconductor oxides may be simpler, but suffer from lack of selectivity and interference from other gaseous species with similar chemical and physical properties.

Fused salts

Early work performed by Salzano and Newman [37] consisted of fused salts, i.e., $Na_2SO_4, K_2SO_4, Li_2SO_4$, as the electrolyte in conjunction with a cationic permeable quartz. Contained within quartz envelopes, platinum leads were placed in contact with additional fused salt. In both of the quartz envelopes mixtures of $SO_2 + O_2$ were flowed; the reference electrode with a known concentration of SO_3, and the working electrode with an unknown concentration of SO_3. These cells were found to be capable of measuring concentrations of SO_3 in the ppm range according to the Nernst equation (i.e., Nernstian response) .

Sulfate solid electrolytes

In work performed by Gauthier et al. [9, 38], the fused salts previously utilized by Salzano were replaced with a solid electrolyte consisting of K_2SO_4. Using gas mixtures of $SO_2 + O_2$ at the working and reference electrodes, the cell responded to SO_2 concentrations between 0.5 and 40,000 ppm. The limitations of the gas mixture preparation prevented determination of the lower concentration limit. It was shown that the emf was essentially constant with a flow rate between a few cm^3/min to 500 cm^3/min, unlike previous work by Salzano. However, at higher concentration levels (above 1000 ppm) and at temperatures below 700 °C, it was apparent that conversion of SO_2 to SO_3 was not reaching equilibrium, with a subsequent drop in the cell emf noted.

These sulfate-sensor investigations continued with electrolytes such as K_2SO_4, Na_2SO_4 and Li_2SO_4 by Liu and Worrell [39, 40] . It was shown by Mari et al [41] that decreasing the thickness of the solid electrolyte reduced the response time of the sensor. In work performed by Worrell [7], it was shown that it is possible to utilize a two-phase electrolyte consisting of Ag_2SO_4 and Li_2SO_4 for the measurement of SO_2 and SO_3. In the two phase region (containing the phases αLi_2SO_4ss and (Ag, $Li)_2SO_4$ss), the chemical potential of each phase is constant at constant temperature. A chemical reaction can change the amount of each phase, but not its composition or chemical potential. In addition, if the Ag-Ag_2SO_4 reference electrode is constructed with the same chemical potential as the two-phase electrolyte, there will be no chemical interaction between them. Qualitative experiments clearly indicate that the lower SO_2 concentration limit for reliable measurements is determined by the thermodynamic decomposition of Ag_2SO_4 [38, 42] which is, in theory, approximately 10^{-6} ppm SO_2 in air at 530°C. The upper limit is related to the transport of SO_2 and/or SO_3 from the gas mixture to the silver components of the two-phase electrolyte. Hence, the upper limit is related to kinetic factors that vary with cell design and are, therefore, more difficult to determine. Evidence obtained from work by Liu and Worrell [40] has determined that the upper limit is at least 10,000 ppm SO_2/SO_3. The

construction of a sensor with these materials has the potential for measurement of SO_2/SO_3 concentrations from sub-ppm to 10,000 ppm with a single sensor.

The ionic conductivity of Ag_2SO_4 was determined to increase several times with the addition of either A_2SO_4, with A = Li, Na or K, or MSO_4, with M = Sr or Br [43]. With the addition of 5.3 m/o of K_2SO_4 the conductivity increased five times over pure Ag_2SO_4. The conductivity varied from ~$1.9x10^{-5}$ S/cm at 250 °C to ~0.12 S/cm at 560 °C. There was a smooth linear increase in conductivity without the large increase in conductivity of pure Ag_2SO_4 at 420 °C due to a phase transformation. It was also observed that the addition of 0.27 m/o $BaSO_4$ to Ag_2SO_4 increased the conductivity about half an order; however, a large step increase in conductivity at 420 °C was observed as in pure Ag_2SO_4. The conductivity of $BaSO_4$ doped material varied from ~$2.4x10^{-5}$ S/cm at 260 °C to ~0.02 S/cm at 560 °C. The activity of Ag_2SO_4 in Ag_2SO_4-(0.27 m/o) $BaSO_4$ is very close to unity and is expected to remain at this level over time. In addition, the thermal shock resistance is significantly improved with a small amount of $BaSO_4$. The sensor was of the following configuration:

$$Pt|Ag_2SO_4\text{-}(0.27\,mol\%\,BaSO_4)|Ag \qquad (4.1)$$

The working electrode consisted of a Pt mesh with the reference electrode consisting of Ag wire. This is an extremely simple design which is very amenable to miniaturization. The sensor was found to display a linear relationship between emf and the log of SO_2 concentration from 10-10,000 ppm at 600 °C. This sensor would also be suitable for operation between 450 and 600 °C and possibly lower temperatures, depending on the kinetics of the electrode reactions and the ionic conductivity of the solid electrolyte. Two different types of catalyst for the conversion of SO_2 to SO_3 were tested, one consisting of porous V_2O_5 powder, the other being a Pt –coated quartz fiber catalyst. The V_2O_5 catalyst was found to take a long time to adjust to changes in SO_2 concentration (i.e., 40 min for a change from 713 to 484 ppm SO_2) due to adsorption and desorption of SO_2 and SO_2 on the surface of the powder. In comparison the Pt-coated quartz fibre took three minutes to respond

to a change in concentration from 467 to 267 ppm of SO_2. Clearly, a properly designed catalyst is required as part of the overall sensor design.

Alternative solid electrolytes

SO_X Sensors:

The solid electrolyte CaF_2 had been utilized in a SO_2 sensor with a $CaSO_4$ auxiliary electrode [44]. Unfortunately, the sensor displayed a very slow response to SO_2 of between 2-8 hr. It was also found that CaF_2 is not stable in a humid atmosphere according to the following reaction:

$$CaF_2 + H_2O + SO_3 \rightleftharpoons 2HF + CaSO_4 \qquad (4.2)$$

It is also possible to utilize NASICON ($Na_{1+x}Zr_2Si_xP_{3-x}O_{12}\,(0 \le x \le 3)$) with an auxiliary electrode consisting of Na_2SO_4-$BaSO_4$ [45]. In this work the cells were of the configuration:

Cell I: $$Pt, SO_2, O_2 | Na_2SO_4 | NASICON | O_2 \text{ in air}, Pt \qquad (4.3)$$

Cell II: $$Pt, SO_2, O_2 | Na_2SO_4\text{-}BaSO_4 | NASICON | Na_2SiO_4, Pt \qquad (4.4)$$

In cell II the reference electrode consists of Na_2SiO_4 and Pt. The cell that utilized O_2 in air as a reference electrode was found to be very unstable. However, in Cell II with the solid phase reference electrode, good agreement between measured and calculated slopes from the Nernst equation was observed. This was studied with mixtures consisting of between 5-98 ppm SO_2 in air. It is well known that Na_2SO_4 is deliquescent and will absorb water. Therefore, the addition of 40 m/o $BaSO_4$ to the auxiliary electrode was found to eliminate the water vapour effect when exposed to a wet SO_2 atmosphere. However, all the measured experimental data were somewhat

below the calculated values. The explanation provided was that the reaction between the inlet SO_2 gas and water vapour results in the formation of H_2SO_4, with the gas composition being reduced according to the extent of this reaction.

A series of micro-machined thin film solid state electrochemical sensors capable of detecting CO_2, NO_2 and SO_2 were fabricated [46]. The SO_2 sensor consisted of the following configuration:

SO_2 Sensor $$SO_2, Pt | Na_2SO_4 - BaSO_4 - Ag_2SO_4 | Ag, SO_2 \qquad (4.5)$$

The SO_2 microsensor had a 90% response time of 1-2 seconds for introduction of SO_2 with 5 seconds required to reach the 90% recovery time upon removal of SO_2. Sensitivity was observed to be 50 ± 3 mV/decade as compared to the theoretical value of 51.9 mV/decade at 250 °C.

The power requirement of the micro-machined gas sensors compared to bulk sensors was 5 mW versus 15 W, respectively, and response and recovery times were between 6-15X faster with the micro-machined sensor. Since the solid electrolytes were deposited as thin films, the reaction rate was not governed by the ionic conductivity, an important benefit with miniaturization. The selectivity of the various sensors was determined with the addition of CO, CO_2, NO_2, SO_2, oxygen and humidity to the gas streams. With the CO_2 sensor there was no measurable interference for CO, oxygen or humidity, but both NO_2 and SO_2 had an effect between 10-100 ppm, causing the emf to change by 75 mV.

An SO_2 sensor was fabricated with a working electrode consisting of a Ag plated Pt mesh, a yttria stabilized zirconia (YSZ) solid electrolyte, an auxiliary phase of Ag_2SO_4-$BaSO_4$ and a reference electrode constructed with a Pt thin film and a bonded Pt gauze [47]. This sensor was of the following configuration:

$$\text{Ag (silver plated Pt)}, SO_2 | Ag_2SO_4\text{-}BaSO_4 | \text{Yttria-Zirconia} | Pt, O_2 \qquad (4.6)$$

The YSZ disk was 15 mm in diameter and ~0.5 mm (500 μm) thick, with a 90% response time to 100 ppm SO_2 of 40 seconds at an operating temperature of 600 °C. However, the time for recovery to an emf corresponding to 5 ppm SO_2 was about 1 minute. The sensor was tested with a concentration of between 1 and 1,000 ppm SO_2 in air. Over this range the emf was linear to the logarithm of [SO_2] with a slope of -85.6 mV/decade, which was considered to be very close to the theoretical calculated value of -86.6 mV/decade. For the auxiliary phase, Ag_2SO_4 was utilized instead of Li_2SO_4 due to its lower water solubility. This is an important distinction since typical combustion exhausts contain a substantial amount of water vapour.

A SO_2 potentiometric sensor consisting of a Ag+-glass-Ag_2SO_4 composite solid electrolyte was investigated for the measurement of SO_2 in a temperature range from 573-773 K [48]. In this work a glass phase consisting of $10Ag_2O{:}30SiO_2{:}60B_2O_3$ was dispersed into Ag_2SO_4 forming the glass electrolyte. Polycrystalline ion conductors are preferred over single crystal and glasses due to their ease of fabrication, isotropy in physical and mechanical properties, good response time and thermodynamic stability. However, polycrystalline materials have built-in micropores which both hinder the mobility of ions and allow permeation of gas. This is especially a problem with temperature cycling as the microcracks will continue to grow and eventually degrade the sensor. An alternative is glass dispersed composite electrolytes, which have been reported to be less porous as well as highly conductive [49]. The glass was found to not only fill the pores in the Ag_2SO_4 material, but also to reduce the grain size with an optimum reduction of voids at 30 wt.% glass. However, at 20 wt.% glass the maximum conductivity was obtained. With these materials a cell was constructed with the following configuration:

$$Ag\text{-}Ag_2SO_4|Glass\text{-}Ag_2SO_4|Pt \qquad (4.7)$$

The reference electrode consists of a Ag-Ag_2SO_4 mixture with the solid electrolyte formed from the glass-Ag_2SO_4 mixture and a working electrode fabricated out of a thin film of sputtered Pt.

This sensor was tested with a gas mixture consisting of either 500 or 1,000 ppm of SO_2 with a fixed oxygen partial pressure of 21 vol% oxygen at a temperature of 773 K. It was determined that this sensor is capable of measuring from 100-10,000 ppm of SO_2 in 21 vol.% O_2. The time to reach 90% of final response value was found to be 50 seconds for a solid electrolyte pellet with a thickness of between 1-2 mm (1,000-2,000 μm). It was determined that in comparison to a pellet constructed of pure Ag_2SO_4, the glass composite yielded a higher emf. This was attributed to the fact that since pure Ag_2SO_4 will present voids and micro-cracks at the surface, inferior ohmic contacts will result at the interfaces between the solid electrolyte and the electrodes. It was suggested that the uniform distribution of fine Ag_2SO_4 grains at the surface of the composite solid electrolyte provide a large number of triple points (Pt-Ag_2SO_4-SO_2) resulting in rapid equilibration and a shortened response time. This would explain the relatively short response time of 50 seconds observed, for the thick pellets used (1-2 mm). In addition, after five thermal cycles, it was determined that pure Ag_2SO_4 developed micro-cracks, whereas the glass composite remained intact.

A solid state electrochemical sensor for measurement of SO_x was constructed with a bi-electrolyte structure consisting of $Na_3Zr_2Si_2PO_{12}$ (NASICON) and Y_2O_3(8m/o)–ZrO_2 [50]. The sensor was of the form:

$$Pt, YSZ(\text{thin film})|NASICON|Na_2SO_4, Pt \qquad (4.8)$$

In previous work, biphasic reference electrodes consisting of either Na_2TiO_6 + TiO_2, $Na_2Ti_3O_7$ + $Na_2Ti_6O_{13}$, or $Na_2Ti_3O_7$ + $Na_{22}Ti_6O_{13}$ were utilized for the measurement of CO_2 gas [51-53]. However, if any of these biphasic reference electrodes were exposed to SO_x, thermodynamics predicts the formation of Na_2SO_4 from Na_2O present in the reference electrode material and the SO_x gas. This would result in instability of the open circuit voltage of the SO_x sensor over time. The bi-electrolyte design was chosen for the following reasons: to prevent the formation of Na_2SO_4 at the reference electrode surface of the NASICON solid electrolyte, to eliminate the need of isolating the reference electrode from the sensing electrode, and to provide a

planar sensor design that is simple to fabricate. This sensor's emf was measured from 823-1123 K at concentrations ranging from 100-3000 ppm SO_2 in air. The SO_2 gas mixture was converted into SO_3 by passing the gas stream through a heated ceramic honeycomb Pt catalyst before it arrived at the working electrode. It was determined that the measured emf of the sensor varied non-linearly as a function of temperature between 823-1123 K with a gas mixture containing 1000 ppm SO_2. The theoretical emf values were about 230 mV lower at higher temperatures and about 280 mV lower at lower temperatures in comparison to the measured values. With operation of the sensor between 973-1023 K in gas mixtures of 100-3000 ppm SO_2 in air, the measured emf was about 120 mV lower; however, the slope of the theoretical calculations agrees very well with the observed values. The deviation from the theoretical emf was attributed to:

- Non-equilibrium conditions prevailing in the gas mixtures at lower temperatures
- Uncertainty in the thermodynamic data for Na_2SO_4, Na_2O and SO_3
- The composition of the NASICON was closer to x = 1.5 ($Na_{2.5}Zr_2Si_{1.5}P_{1.5}O_{12}$) instead of x = 2 ($Na_3Zr_2Si_2PO_{12}$)

The time required for the sensor to reach 90% of the stable emf value was found to vary between 10-20 minutes depending on the temperature. Therefore, this sensor displayed a slow response to changes in gas concentration.

A NASICON based sensor was constructed utilizing a Na_2SO_4-$BaSO_4$ auxiliary electrode consisting of the following structure [54]:

$$Pt,SO_2,O_2|Na_2SO_4\text{-}xBaSO_4|NASICON|Na_2SiO_3|Pt \qquad (4.9)$$

NASICON is a good choice for use in SO_2, NO_2 and CO_2 sensors due to its high Na^+ conductivity at even relatively low temperatures (200-250 °C), no crack formation during thermal cycling and a negligible electronic transference number of 10^{-5}. As previously noted the use of a Na_2CO_3-$BaCO_3$ auxiliary in a NASICON based CO_2

sensor improved the effect of moisture on this sensor [55]. Therefore, the addition of x = 0-40 mol% $BaSO_4$ (water solubility of 0.000115 in 100 parts of water) into the auxiliary was added to reduce the effect of moisture in the measured gas stream. The reference electrode consisted of Na_2SiO_3. Gas mixtures consisting of between 5-95 ppm SO_2 in air were introduced into the sensor at a flow rate of 200 cm^3/min. The effect of moisture was observed by bubbling the gas mixtures through a water reservoir at a given temperature. Cells with an auxiliary electrode consisting of Na_2SO_4 only displayed unstable sensing behaviour (i.e., 50 mV spread in response) at the lower operational temperature of 400 °C. However, cells constructed with either pure Na_2SO_4 or Na_2SO_4-x$BaSO_4$ auxiliary electrodes exhibited stable behaviour above 550 °C in dry SO_2 atmospheres, arising from the lack of moisture and the complete conversion of SO_2 to SO_3 at the higher temperature. For cells with either pure Na_2SO_4, 10 m/o $BaSO_4$, 20 m/o $BaSO_4$ or 30 m/o $BaSO_4$, the slopes in the plot of emf versus log($P_{SO_{2(ss)}}$) were in good agreement with the expected Nernstian slope at 550 °C in dry SO_2. Cells consisting of pure Na_2SO_4 only were found to become unstable after only 10 days, even with dry SO_2. By comparison, with an auxiliary consisting of 10 m/o $BaSO_4$, a cell operated at 550 °C with gas concentrations between 5-95 ppm SO_2 was stable for 30 days. As the $BaSO_4$ content was raised from 10 to 40 m/o in the auxiliary electrode, the shift in the cell emf due to water vapour (~4 vol%) declined from 25 mV to 3 mV. The remaining shift of 3 mV was attributed to the formation of H_2SO_4 from water vapour, oxygen and SO_2 according to the reaction:

$$SO_{2(g)} + \tfrac{1}{2}O_{2(g)} + H_2O_{(g)} \rightleftharpoons H_2SO_{4(g)} \qquad (4.10)$$

Extended long-term testing of more than six months needs to be performed, as 30 days is too short for long term or commercial applications. Response times of 5, 3 and 4 minutes at 550 °C for pure Na_2SO_4, 10 m/o $BaSO_4$, and 20-30 m/o $BaSO_4$ in 90 ppm SO_2 were observed, respectively. The shortest response time was with a cell consisting of a 10 m/o $BaSO_4$ auxiliary electrode due to a porous, needle-like surface.

In most instances the reference electrode is physically separated from the working electrode. This requires gas tight electrolytes with good sealing between the sensing and reference sides of the sensor. Since sensors operate at relatively high temperatures, i.e., > 250 °C, there are sealing problems due to differential expansion coefficients in the materials that are commonly used. It is somewhat difficult to construct gas tight, long lasting cells, especially when temperature cycling occurs. The application of a gas reference electrode is not practical except for a few specialized applications.

To eliminate the need for a separate reference electrode, various sensor configurations have been developed and tested. In one configuration an SO_2 sensor based on temperature gradients and mobile Na^+ in β"-alumina without a reference electrode was tested [56]. The temperature difference between the reference and working electrode was about 100 °C, resulting in a large deviation in the experimental emf as calculated using the Nernst equation for an isothermal system. Response time for this cell was 10 minutes, too long for most applications, but the simple design holds promise if micro-machined.

The most recent work consists of an electrochemical cell constructed with a Na_2SO_4 auxiliary, combined with a divalent (Mg^{2+}) solid electrolyte consisting of $MgZr_4(PO_4)_6$ [57]. This cell had the following structure:

$$Pt, SO_3, O_2 | Na_2SO_4 | MgZr_4(PO_4)_6 | O_2, SO_3, Pt \qquad (4.11)$$

The porous Na_2SO_4 auxiliary layer was attached to one side of the $MgZr_4(PO_4)_6$ electrolyte by coating with Na_2SO_4 paste and sintering at 1173 K for 5 hr. As the sensor responds to SO_3, the measurement of SO_2 requires conversion to SO_3. Therefore, alumina pellets containing 1% Pt adjacent to the auxiliary electrode were used as a catalyst. The sensor was tested under controlled conditions at various SO_2 concentrations, operating temperatures and partial pressures of O_2. For the SO_2 flow (set at 100 cm^3/min) the mixture was prepared by diluting a parent gas consisting of

5,000 ppm of SO_2 in air + N_2 with synthetic air. The SO_2 concentration was varied from 0-1,000 ppm in air with P_{O_2} = 20.95%. Temperatures from 873-1073 K were investigated with the sensor. The measured emf response of the sensor versus the $\log(P_{SO_2})$ was determined to be linear along with a negative slope at all test temperatures. The number of electrons transferred in the electrochemical reaction, given as n, varied from 0.95 at 673 K, 1.16 at 923 K, 1.54 at 972 K, to 1.56 at 1021 K. It was observed that n approached the value of 2 at higher temperatures. The response time to achieve 90% of the stable emf value was less than 3 minutes, with response times decreasing as the SO_2 concentration increased. In comparison, the recovery time on switching off the SO_2 flow was 5 minutes.

H_2S Sensors:

A potentiometric gaseous sulfur sensor consisting of Ag β-alumina was constructed and tested for the range between 908-1043 K with H_2S gas [58] . The sensor examined in this work consisted of the following configuration:

$$Ag|\ Ag^{+}\beta\text{-Alumina}|Ag_2S, MoS_x, S_{2(gas)}, N_2, Au \qquad (4.12)$$

It was determined that Pt at the working electrode had an adverse effect on the equilibration of H_2S/H_2 and was, therefore, replaced with gold. This improved the response but the addition of an in-situ layer of Ag_2S and MoS_x was also required. To activate this layer, a 17 hr activation via a flow of 1% H_2S at 825K was performed. This sensor was found to be capable of measuring sulfur fugacity as low as 100 Pa (10^{-3} atm) which were obtained from dissociated H_2S in a narrow range of temperature from 950-1050 K in oxygen-free non-reducing atmospheres.

For the measurement of H_2S in coal gasification atmospheres, a sensor was constructed consisting of Na-β-alumina as the solid electrolyte and Na_2S as the auxiliary phase [59]. The configuration of this sensor is as follows:

$$Pt, Na_2S|Na\text{-}\beta\text{-alumina}|Fe_2O_3\text{-}Na_2O\text{-}Fe_2O_3 \quad (4.13)$$

This sensor was placed into a coal gasification unit with H_2S concentrations set at 2000 ppm. With the addition of limestone, the concentration drops to below 200 ppm. The sensor was capable of measuring H_2S concentrations from 2000 to 150 ppm at an operational temperature of 860K. The experimentally obtained emf values corresponded with theoretical values. Since the coal gasification atmosphere has an oxygen concentration of only 0.2 vol%, this atmosphere is considered to be reducing. It was determined that this sensor is usable as an online H_2S gas sensor and will survive in an aggressive coal gasification atmosphere.

Chapter 5: Sensor Performance Factors

Selectivity

This is probably the most important characteristic of a chemical sensor, the ability to discriminate between different substances. The behaviour is primarily a function of the selective component, although the operation of the sensor or transducer can contribute to the selectivity. Solid state ionic chemical sensors are inherently selective to their associated gaseous species. This is not the case with other chemical sensors based on semiconductor and optical technology, with interference from other gas species being a serious problem.

Sensitivity

Sensitivity of an instrument is the minimum detectable change of the variable being measured (the measurand). The required sensitivity can vary depending on the intended application, with liquid sensors typically requiring sub-millimolar sensitivity, but in some special cases sensitivity can be necessary into the femtomolar (10^{-15} M) range. In comparison with gas sensors, the required sensitivity is typically in the ppm range, with special cases requiring ppb sensitivity.

The equation for the sensitivity of a potentiometric sensor is given by:

$$\frac{\delta P}{\delta E} = \frac{nFP}{RT} \tag{5.1}$$

where δP is the variance in the pressure, δE the variance in the cell emf, n the number of electrons transferred, F the Faraday constant, P is the pressure, R the gas constant and T the temperature in Kelvin.

It follows that the sensitivity or relative error ($\delta P/P$) in measurement of a gas pressure is given by:

$$\frac{\delta P}{P} = \frac{nF}{RT}\delta E \tag{5.2}$$

For the sulfur oxide sensor studied in this work, the sensitivity is given by:

$$\text{sensitivity} = \frac{\delta P}{P} = \frac{2F}{RT}\delta E \tag{5.3}$$

With the sensor operating at 535 °C the sensitivity is equivalent to:

$$\text{sensitivity} = \frac{\delta P}{P} = 28.7(\delta E) \tag{5.4}$$

where δE = accuracy in the measured voltage, which is 0.001 V.

Therefore, the sensor in this work has a sensitivity of 2.9×10^{-2}. For example, a gas concentration of 100 ppm in SO_2 would result in a sensitivity of 2.9 ppm.

It is important that measurement of the open circuit voltage is performed with a high impedance voltmeter or an electrometer. If the impedance is not high enough, the electrodes can become polarized. For continuous measurements of cell voltages it is recommended to utilize an electrometer with an input impedance of 10^{12} ohms or higher.

It is important in the design of the sensor that effective shielding of the external voltage measurement circuit is incorporated, so as to maximize the accuracy of the voltage signal. Also, the higher the ionic conductivity, the less susceptible the sensor is to interference from stray electrical fields, resulting in a more accurate measurement of voltage. Properly shielded and grounded lead wires along with a grounded shield around the sensor would also be beneficial.

Variation in temperature across the sensor will also create an additional contribution to the measured cell voltage or emf. For example, with an oxide based solid electrolyte cell this contribution is defined by:

$$E = \frac{1}{4F}\left[\mu''_{X_2}\left(T_2, P''_{X_2}\right) - \mu'_{X_2}\left(T_2, P'_{X_2}\right)\right] + \alpha\left(T_2 - T_1\right) \tag{5.5}$$

where T_2 and T_1 are the temperatures at the two electrode-electrolyte interfaces, μ''_{X_2} and P''_{X_2} are the chemical potential and partial pressure of the gas phase X_2, and α is the seebeck coefficient consisting of the partial entropies and heats of transfer of the electrolyte and the electrode.

Accuracy

The accuracy of an instrument indicates the deviation or error of the reading from a known input. Related to the accuracy is the precision or the ability to reproduce a certain reading with a given accuracy. Uncertainty differs from the error in that it is an estimate of uncertainty or confidence in a measurement without having a known value with which to compare.

Accuracy is expressed in terms of either the absolute error or relative error. The absolute error, E_a, of the mean or average, $\bar{x}$, of a small set of measurements is given by the relationship:

$$E_a = \bar{x} - x_i \tag{5.6}$$

where x_i is the accepted value of the quantity being measured.

The relative error, $E_{r.e.}$, is typically given by:

$$E_{r.e.} = \left(\frac{\bar{x} - x_i}{x_i} \right) 100\% \tag{5.7}$$

The absolute error, E_a, consists of random or indeterminate errors, E_{random}, and systematic or determinate errors, $E_{systematic}$, as given by the equation:

$$E_a = E_{random} + E_{systematic} \tag{5.8}$$

When a set of measurements is repeated on the same sample, the data are typically scattered due to the presence of random or indeterminate errors which is an indication of the imprecision in the data. Random error is typically described by the equation:

$$STDEV = \sqrt{\frac{\sum_{i=1}^{N}(x_i - \bar{x})^2}{N-1}} \tag{5.9}$$

where STDEV is the standard deviation and N the number of measurements.

Typically, during measurement, random errors result in the data not all falling exactly on the line of a curve fit. It is usually assumed that deviation from the expected values is due to errors in measurement of the values on the ordinate axis. The values on the x-axis are considered to be known exactly. This is of course relative, as error in gas concentration is not insignificant in this experimental work. The vertical deviation of each point from the straight line is called a residual. And the line generated by the least-squares method (see Appendix B) is the one that minimizes the sum of the squares of the residuals for all of the points. This technique is utilized in determination of error in the experimental cell equations with respect to the slope and y-intercepts.

Systematic error has three sources consisting of instrumental, personal and method:

- Instrumental errors include drift in electronic circuits, leakage in vacuum systems, temperature effects on detectors, induced currents from ac power lines, decrease in voltage of battery sources, and calibration errors in meters, weights and volumetric equipment. It is, therefore, important to perform periodic calibration with quality standards so as to reduce systematic error.

- Personal errors are those introduced into a measurement due to judgments made by the experimentalist. For example, estimating the position of a pointer on a scale, the color of a solution in a titration, and prejudice contribute to

personal error. This type of error is reduced through the automation of data collection with computerized systems.

- Method errors result from non-ideal chemical and physical behaviour of reagents and reactions upon which the experiment is based. This is the result of slow kinetics of chemical reactions, losses due to volatility, adsorption of the analyte on solids, instability of reagents, contamination and chemical interference.

The sequence for the deployment of an accurate sulfur oxide sensor would require the creation of a calibration curve covering the span of the desired concentration range. It is, therefore, important that the concentration of the gas species is provided with the highest precision possible. From the creation of a calibration curve associated with each chemical sensor, measurements of the cell emf (volts) permit calculation of the gas concentration, [SO_2, ppm], and the associated error, $s_{measured}$, in the calculated value of concentration. It is apparent that the calibration curve needs to be created with the highest accuracy possible. Since measurement of the cell emf is accurate to 1 part in one thousand (±0.1%), the SO_2 concentration in the cylinders accurate to ±1% and mixtures of SO_2 in air accurate to ±5%, gas concentration is the major factor in experimental error.

In more general terms, accuracy can be expressed either in terms of a percentage of the absolute value measured or as a percentage of the accuracy of the range being measured. For example, a sensor with a measurement range of between 0-100 ppm with an accuracy of ±5% would be accurate to ±5 ppm. This is compared to a chemical sensor with an absolute measurement accuracy of ±5%, which would have more demanding requirements. For example at a sensor reading of 5 ppm, the accuracy would be ±0.25 ppm whereas for a reading of 90 ppm it would be accurate to ± 4.5 ppm. Regardless, attention must be paid to how accuracy is specified. For high quality chemical sensors, the required accuracy is typically ±5% of the absolute measurement value. There is also a close relationship between the sensitivity of the

sensor and obtainable accuracy. This must also be taken into consideration in the design and performance characteristics of the sensor.

Long-term Stability

Sensors can be divided into two groups, unstable sensors with irreversible drift in the measured signal and stable sensors with slight reversible fluctuations of the measured signal. An unstable signal can be explained in terms of a continuous change of transference numbers of different ions and electrons leading to the change in both n (the number of electrons transferred) and the value of the measured voltage. Changes in the ionic transference number are attributed to reactions between the electrodes and the electrolyte. The composition of the reference electrode also has a significant influence on the long-term stability of sensors. With stable sensors, fluctuations in the measured voltage can be due to the formation of phases at the interface between the reference electrode and electrolyte.

Response Time

The response of a sensor can be defined as the response time in relation to a step change in concentration. For an increase in concentration, the time required to reach 90% of the steady state value, E_t, is given as t_{90}. When there is a drop in concentration, the time to reach 10% of the lower steady state value is defined as t_{10}. The transient response is given by:

$$E = E_t\left(1\text{-}e^{-\frac{t}{\tau_{eq}}}\right) \qquad (5.10)$$

where τ_{eq} is the equivalent time constant of the whole sensor circuit.

The time constant, τ_{eq}, is equivalent to the time constant of the slowest mechanism. For comparison, the fastest response times are typically in the range of a few milliseconds with most other response times in terms of a few seconds or minutes. In a sensor, the response time is generally imposed by the kinetics required to reach a

new equilibrium state. Extrinsic phenomena can also occur such as diffusion in liquid or gaseous phases, convection, and interaction with all components of the sensor (i.e., adsorption and desorption phenomena), with all of these phenomena slowing down the response time. In Figure 5-1 a schematic of an equivalent circuit for a chemical sensor is given. It is apparent that impedance spectroscopy is a useful tool in determining the individual components and their effect on response times.

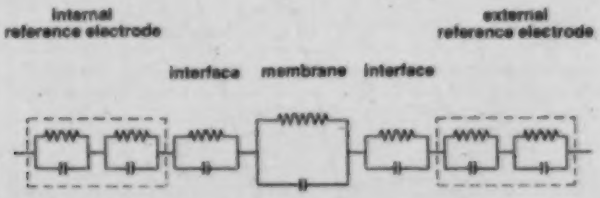

Figure 5-1. Equivalent circuit for a potentiometric sensor

Recovery Time

This is the time that elapses before the sensor is ready to analyze the next sample, the shorter time required the better – typically less than a couple of minutes for a chemical sensor.

Working Lifetime

The working lifetime is determined by the stability of the detection material. For biological sensors it can be as short as a few days; for other applications it should be several months or years. In general, it is required that a gas sensor should exhibit a stable and reproducible signal for at least 2-3 years (17,000-26,000 hr).

Chapter 6: Fabrication Techniques

In the fabrication of the sulfur oxide chemical sensor, various techniques were utilized in its construction. This included compaction and sintering of the base material as well as thick film and thin film deposition techniques.

Forming and Pressing

In the initial phases of the experimental work, mixtures of Ag_2SO_4 and Li_2SO_4 were transformed into a green product followed by sintering at 500 °C in an atmosphere consisting of 500 ppm SO_2 in air. The final product must be controlled with respect to density, size, shape, surface and microstructure. For these reasons it is imperative that the green product is carefully controlled with respect to density and microstructure. It is also important that if a smooth surface is required, it is initially obtained in the green product.

Dry pressing utilizes punches which are pushed into hardened alloy or carbide dies and is commonly used for pressing parts thicker than 0.5 mm and parts with surface features in the pressing direction. The die and punch sets are typically fabricated with hardened steel and, if wear is a concern, tungsten carbide or other ceramic inserts are added. When pressing micron-sized particles the clearance between the die and punch is between 10-25 μm, for granular particles the clearance is up to 100 μm.

The maximum pressure used in dry pressing is from 20-100 MPa, with higher pressures being used for technical ceramics as compared to clay based materials. If products with two or three dimensional shapes are required, isostatic pressing in flexible rubber molds would have to be utilized.

Thick Film Deposition

The deposition of thick films is based upon the formation of patterns through the use of woven screens and viscous pastes. What makes this technique incredibly versatile

is that virtually any material can be made imto a viscous paste, including most liquids and solids.

Thick film technology originated out of the need to fabricate resistors onto flat surfaces in combination with the printing of metallic conductors onto circuit boards. The need for thick film printing of capacitors onto flat surfaces also exists, but for various reasons, both technical and economic, this process has not been applied to date.

The thick film technique relies on the sintering of powders together to form either conductive or insulating layers. This technique is a high temperature process despite the fact that some metals can be sintered at around 300 °C. Regardless, particle sizes and distributions should be chosen such that sintering temperatures for both the conductor and insulating layers possess a common range.

The equipment required for deposition is relatively simple, with a woven mesh screen made of either stainless steel or nylon, mounted under tension typically on a metal frame. In Figure 6-1 a picture of the screen utilized for thick film depositions with the sulfur oxide chemical sensor is shown. To define the circuit pattern or deposited layer, an ultra-violet (U.V.) photosensitive layer was attached to the screen, then exposed to U.V. light through a mask followed by chemical development. The thick film paste was then placed onto the printing screen, with the screen suspended about 0.5 mm above the substrate to be coated. A scraper blade called a squeegee traverses the screen under pressure, bringing the screen with the thick film paste into contact with the substrate and, therefore, depositing the paste onto the substrate. Since the screen possesses elasticity, once the pressure on the squeegee is removed, the screen rebounds from the substrate leaving the thick film deposited onto the underlying substrate (in this case a round alumina disc). The scraping motion can be performed by hand or by machine; in this instance manual operation was adequate for fabrication of the chemical sensor given its moderate patterning requirements. To achieve dimensional accuracy with printed patterns in the range of 250 μm line widths, simple hand operated equipment is adequate.

Figure 6-1. Thick film screen and holder

Thick film pastes typically consist of three major components:

- The powdered metal or compound which makes up the functional component which provides the electric and/or sensing properties
- A glass frit or oxide also in particulate form which acts as a bonding agent for joining of the functional layer to the substrate
- An organic vehicle in which the above components are suspended that acts as a vehicle for the components to be sintered. This vehicle typically consists of a blend of volatile solvents, polymers and/or resins which provide a homogenous suspension of the functional materials and a rheology suitable for screen printing.

In this work, the materials utilized as the solid electrolyte possess a melting point within 50 °C of the maximum operational temperature; therefore, the addition of a frit is not practical.

The organic vehicle is required to possess a low temperature coefficient of viscosity and should also be constituted so as to burn off in air without leaving any residue. To lower the sintering temperature, the mean particulate size of the powders should be kept below 5 μm. During the firing process a large amount of shrinkage (up to 30%) will occur as the organic binders are burnt out and as higher temperatures are reached. The final size of the crystals formed is related to the firing temperature, the particle size and size distribution of the original powder, and the cooling rate (if very slow).

Thick film metallic conductor compositions typically consist of finely divided metal powder combined with a small amount of glass frit, which is carried in an organic vehicle. Typical components for a thick film paste are outlined in Table 6-1.

A simple formulation of organic vehicles typically consists of terpineol-type solvents and cellulose-type resins, most commonly $\alpha - terpineol$ and butylcarbitol as the solvents and ethyl cellulose as the polymeric viscosifier. The relative fractions of these ingredients are varied according to the types and amounts of the inorganic materials in the paste. These thick film vehicles are utilized in the printing of a variety of solid systems.

As the base metal systems became more common, nitrogen firing of the thick film depositions required a different selection of organic vehicles. In the normal firing of thick films in air, pyrolysis or burn-off of the organic carrier occurs. However, in nitrogen firing, many thick film compositions will not burn-off properly. Therefore, alternative solutions have been developed that utilize resins that de-polymerize during heating in the presence of nitrogen. These materials consist of acrylic resins and nitro-cellulose which decompose in the absence of oxygen. In certain types of solid electrolytes this would be invaluable.

Table 6-1. Thick film composition

Component	Comments
Functional Phase	Consists of either metal powders (i.e., Pt, Pd, Ag, Au, etc.) in conductive inks, metals and metal oxides (i.e., RuO_2, Bi_2O_3, Ru_2O_7, Pd, Ag) in resistors, ceramic/glass ($BaTiO_3$, glass) in dielectrics and in our application solid electrolyte materials (i.e., Ag_2SO_4-Li_2SO_4, Ag_2SO_4-Ba_2SO_4, etc.).
Binder Phase	To hold the ink to the ceramic substrate and merge with the ceramic materials during high temperature firing.
Vehicle	Acts as the carrier for the powders and is composed of both volatile (solvents) and non-volatile (polymers) organics. These evaporate and burn off during the early stages of drying and firing, respectively.
Modifiers	Small amounts of additives which control the behaviour of the inks before and after processing.

Another option for thick film depositions is the use of slurries, which consist of free flowing printable suspensions of fine solid materials in either an organic solvent or water. These are typically applied with brushing or ink jets. There are also polymer based thick film pastes that don't require high temperature firing and do not contain a glassy binder. Instead they utilize a resin consisting of a phenolic, alkyd, modified alkyd, polyester or acrylic composition. Recently, there has been considerable use of higher temperature resistant polyimides which provide enhanced durability.

Screen printing requires that the ink viscosity be controlled within limits determined by other rheological properties, such as the amount of inorganic powders in the ink. Ambient temperature will also influence the viscosity of the ink, altering a vehicle by as much as 4% per degree Celsius. Therefore, the temperature in the print room should be maintained with a constant temperature of 20 +/- 2° Celsius.

The printing screen is prepared by stretching stainless steel wire mesh cloth across the screen frame and attaching it, maintaining high tension in the mesh. The thick film emulsion is then spread over the entire mesh, filling all open areas. As the squeegee moves the ink across the screen, a shearing action causes a decrease in viscosity, allowing the ink to pass through the patterned areas, onto the substrate. As the squeegee passes, the screen peels away and the ink viscosity recovers, leaving a well defined print.

To control the thickness of the deposited layer, the dry print thickness is varied by employing a different screen mesh. In Table 6-2 the typical final dry print thicknesses obtained with various screen sizes are provided. The screen mesh size utilized with thick film depositions in this work was 280 mesh; therefore, the dry print thickness is in the range of 18-20 μm. In designing a miniaturized layered structure, be it an integrated circuit or a chemical sensor, the thickness of the deposited layers will determine the lateral spacing of the functional elements.

Table 6-2. Dry print thickness.

Screen Mesh	Wire Diameter (μm)	Dry print thickness (μm)
200	53	25
220	41	23
250	36	21
325	28	16

In this work, the flow of thick film material upon deposition must be both restricted and controlled once laid done. This is required when holes or vias are required that allow conductive connections between metal layers and when other dimensions are to be retained during several firing or sintering cycles. The design of an integrated sensor would have several structures of this type. There must also be low porosity in some fired films so as to ensure electrical isolation. This is extremely important in fabrication of the solid electrolyte layer.

Thin Film Deposition

Since fabrication of the working electrode consists of a thin film of platinum which was deposited via physical deposition (evaporation), a discussion on thin film deposition methods is necessary. Physical deposition of thin films typically utilizes either evaporation or sputtering techniques. The metal layers for all early semiconductor technologies were deposited by evaporation, due to the modest requirements at that time. Since then sputtering has replaced evaporation as the method of choice, primarily due to its ability to cover surface topology, otherwise known as step coverage. This has become even more critical as the geometries continue to shrink into the sub-micron and into the nanometer size ranges. In fabrication of the sulfur oxide sensor, the main reason for using the evaporation method was the prohibitive cost of acquiring a platinum sputtering target. However, if the lateral and vertical dimensions of the sensor are to be shrunk into the sub-micron ranges for faster response times, deposition of the functional layers would have to be changed to thin film sputtering.

Traditional Evaporation

Thin films are deposited by applying heat to the source material resulting in evaporation. As the temperature of a sample is raised, the source material typically goes through solid, liquid and gas phases. At every temperature there exists an equilibrium pressure, p_{evap}, of vapour above the material. When the sample is below the melting point it is called sublimation, above the melting point it is called evaporation. For the case where the sample charge being evaporated is liquid it has been shown that the partial pressure in torr, p_{evap}, is given by:

$$p_{evap} = 3x10^{12}\,\sigma^{3/2}\,T^{-1/2}\,e^{\Delta H_v/NkT} \qquad (6.1)$$

where σ is the surface tension of the metal, N is Avogadro's number, ΔH_v is the enthalpy of evaporation, k is the Boltzmann constant and T is the temperature in Kelvin.

In practise, even small errors in the determination of ΔH_v will result in large errors in calculation of vapour pressure. Therefore, the vapour pressures are generally determined experimentally. In Figure 6-2 the vapour pressure curves for commonly evaporated substances is given. These values were derived from equations tabulated in Metallurgical Thermochemistry, 5th edition [60].

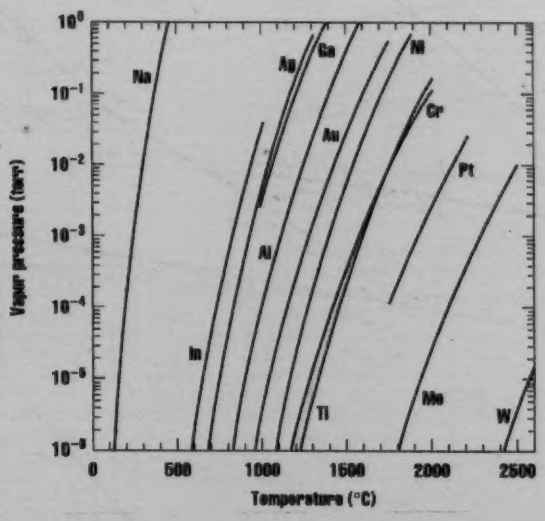

Figure 6-2. Vapour pressure of evaporation materials

It is possible to determine the vapour pressure experimentally under high vacuum conditions. If the heated source resides in a high-vacuum environment, the vaporized atoms or molecules are likely to strike the surface of the substrate without any intervening collisions with other gas molecules. The rate of mass evaporated from the source per unit area per unit time, Γ, due to this evaporation can be estimated from the Langmuir-Knudsen equation and is given as:

$$\Gamma(gm \cdot cm^{-2} \cdot s^{-1}) = 5.834 x 10^{-2} \left(\frac{M}{T}\right)^{1/2} \bullet p_{evap} \qquad (6.2)$$

where M is the molecular weight and T the temperature in Kelvin.

Assuming a uniform evaporation rate across the entire evaporation area and no variations during time, Γ can be obtained from experimental measurements and inserted into equation 6.2 to obtain the evaporation partial pressure, p_{evap}. Typically metal evaporation rates are found to be $\Gamma \approx 10^{-4}\ gm/cm^2$ sec for pressures in the range of 10 millitorr. For more information on metal evaporation rates refer to "Scientific Foundations of Vacuum Techniques" [61].

To obtain reasonable deposition rates, the partial pressure of the material being evaporated must be at least 10 millitorr. It is apparent from Figure 6-2 that several materials need to be heated to very high temperatures to achieve vapour pressures which provide reasonable deposition rates. These materials known as refractory metals, i.e., Ta, W, Mo and Ti have the highest melting points. Platinum which was utilized in the fabrication of the working electrode for this sensor has a melting point 1768.4 °C and requires evaporation temperatures in excess of 2000 °C. For the evaporation of refractory and other high melting point materials specialized equipment is required. Since ionic contaminants such as K have significant vapour pressure even at room temperature, the purity of the material charges is extremely critical. In addition, the cleanliness of the evaporation chamber and the vacuum obtained prior to evaporation are extremely important. During deposition, the vapour pressure created from the evaporated sample charge has to be significantly higher than the contaminants present in the evaporation chamber. This ensures that the thin film deposited contains a minimal level of impurities.

The evaporation of materials is performed under high vacuum conditions in the range of 10^{-7} torr which is obtained with either a diffusion or turbo-molecular vacuum pump prior to the initiation of the evaporation. As the source material is first heated the pressure rises initially as contaminants are desorbed from its surface prior to evaporation of the source material.

The characteristics that are responsible for the widespread use of thin film evaporation consist of the following:

- Thin films can be deposited at high rates (e.g., 0.5 μm / min for Al)
- The low energy of the impinging evaporated atoms onto the substrate (~0.1 eV) leaves the surface undamaged
- Substrate heating assists in the surface mobility of the adsorbed atoms and is the result of the heat of condensation of the deposited film and from heat radiation due to heating of the source material
- Since evaporation is performed at high vacuum, the thin films are deposited with low levels of residual gas incorporation.

With respect to evaporative techniques, the least complex method of depositing thin films is via resistance-heated sources. Usually, a wire of a low pressure metal such as tungsten (W) is used to support small strips of the metal to be evaporated. The W wire is then resistively heated, with the metal charge first melting and wetting the heated filament which is then followed by evaporation. In Figure 6-3 a series of wire and metal foil sources is displayed.

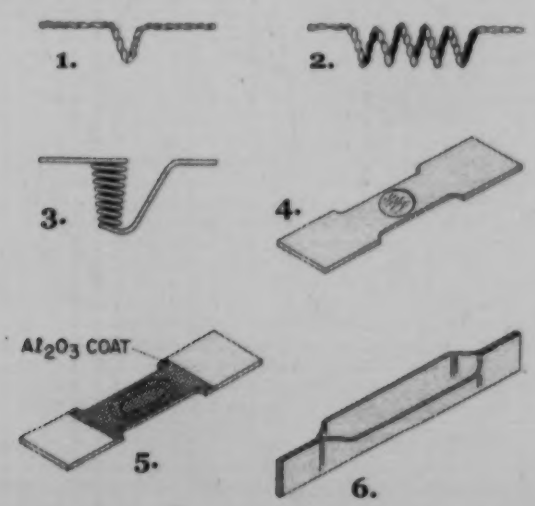

(1.) Hairpin Source. (2.) Wire Helix. (3.) Wire Baskets. (4.) Dimpled Foil. (5.) Dimpled Foil with Alumina Coating. (6.) Canoe Boat

Figure 6-3. Evaporation sources

The hairpin source and wire helix are typically made with 0.51 mm to 1.5 mm diameter tungsten wire with the evaporant species attached in the form of wire. Upon melting, the evaporant must wet the filament and be held by the filament due to its surface tension. In Figure 6-4 a schematic of a thin film evaporator is displayed. These systems consist of a mechanical roughing pump which first lowers the pressure in the vacuum chamber down into the millitorr range. This is backed up by a diffusion pump combined with a cold trap (liquid nitrogen) resulting in a base pressure in the vacuum chamber of 10^{-7} to 10^{-8} torr. At this point electric power is applied to the crucible resulting in evaporation of the material charge and subsequent coating of the substrate material.

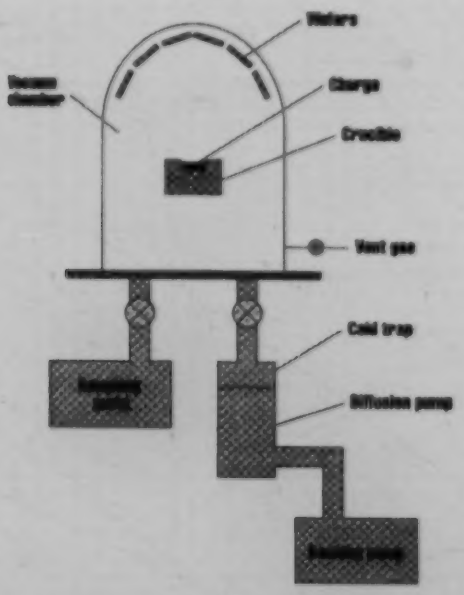

Figure 6-4. Evaporator – thin film deposition

This technique is simple but has several drawbacks in the fabrication of layered thin film microelectronic devices. Poor step coverage of topography and difficulty in producing well-controlled alloys are typical problems. In response to these drawbacks, two other techniques have become widely adopted for performing evaporation depositions - electron beam evaporation and inductive heating

evaporation. In fabrication of the sulfur oxide chemical sensor, deposition of the platinum thin film electrodes was performed with an electron beam evaporator.

Electron Beam Evaporation

With electron beam evaporation, a stream of electrons is accelerated to high kinetic energy (5-30 kV) and then directed at the material to be evaporated, with the kinetic energy being converted into thermal energy upon impact. An electron stream can melt and evaporate any material as long as the energy supplied to the material is equal or greater than the rate at which heat is lost. Electron beam guns are typically able of supplying 1-2 kW of highly concentrated electron energy; therefore, very high film deposition rates in the range of $0.5\,\mu m/\min$ can be attained. Also since the beam energy is concentrated on the surface of the target material, a molten region is created in the center of a cooled structure. This eliminates the problem of the molten evaporant material reacting with or dissolving the crucible leading to contamination of the evaporated species. Therefore, highly pure thin films are possible. In Figure 6-5 a simplified e-beam evaporator system is depicted. Underneath the crucible an intense, high energy beam is ejected. The electron source consists of a tungsten filament located underneath the crucible, so as to minimize the deposition of filament material onto the substrate to be coated. Deflection of the electron beam through an angle of 270 ° with a strong magnetic field is performed steering the beam onto the surface charge. The beam can also be steered and rastered across the charge, melting only the centre of the charge. Therefore, the hot portion of the charge is effectively contained within the cooler portion of the charge.

However, there are two problems which can arise from electron beam evaporation:

- With voltages higher than 10 kV the electron beam will result in the emission of x-rays from the evaporant materials. These x-rays can create damage through the creation of trapped charges. This is particularly a problem with the gate oxides of metal oxide semiconductor (MOS) devices. To remove such damage requires an annealing process.

- If excessive power is applied to the source, metal droplets that are blown out of the charge source by the expanding metal vapour will deposit on the surface of the substrate. Therefore, the power applied to the electron beam must be carefully controlled.

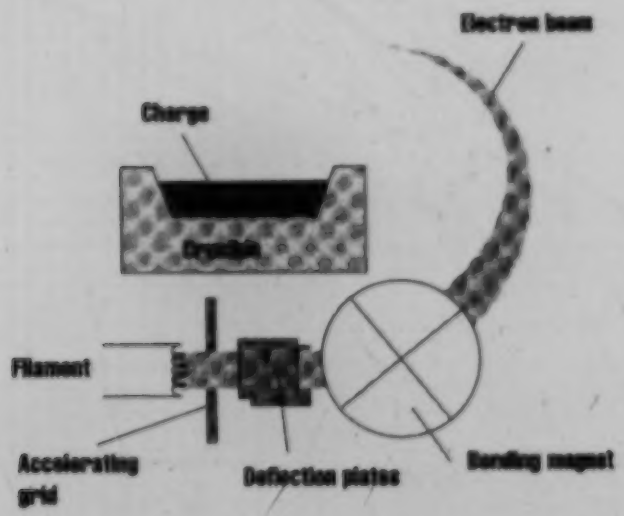

Figure 6-5. E-beam evaporator

If an even higher quality film is required, the technique of sputter deposition is typically utilized. It has enhanced step coverage compared to evaporation, induces less radiation damage than electron beam evaporation and is better at depositing layers of compound materials and alloys. These are the reasons that the majority of metallic thin film depositions in semiconductor manufacture occur via sputtering.

Chapter 7: Components of Experimental Sulfur Oxide Sensor

Solid Electrolyte Layer: Two Phase Ag_2SO_4-Li_2SO_4 Mixture

The ionic conductivity of alkali metal sulfates has been measured, e.g., Na_2SO_4 at 2.1×10^{-3} S/cm at 700 °C [8] and K_2SO_4 at 1.6×10^{-3} S/cm at 800 °C [62]. These values of conductivity are considered to be too low for practical use, especially at these already high operating temperatures. Regardless, the ionic conductivity needs to be increased for the following reasons:

- the higher the conductivity of the electrolyte, the less the effect on the measurement of the emf due to interference from stray electrical fields
- higher ionic conductivity results in a higher ionic diffusion coefficient which is necessary for faster response to changes in gas concentration

For pure Ag_2SO_4, the conductivity is found to follow the Arrhenius rate equation for both the α and the β phases as defined by:

$$\sigma_{ion} T = (\sigma T)_0 \exp\left(-\frac{E_{ion}}{kT}\right) \tag{6.3}$$

where σ_{ion} is the ionic conductivity, T is the temperature in Kelvin, $(\sigma T)_0$ is the pre-exponential factor, E_{ion} the activation energy, and k is the Boltzmann constant.

In Figure 7-1 the variation of log $(\sigma_{ion} T)$ versus 1/T is displayed for pure Ag_2SO_4. There is a significant change observed in the conductivity of pure Ag_2SO_4 due to a phase transition from the orthorhombic phase (β) to the hexagonal phase (α) at 416 °C. The conductivity of pure Ag_2SO_4 at 530 °C is equal to 0.0193 S/cm which is less than ideal since a lower electrolyte conductivity results in a sensor which is more susceptible to stray electrical fields.

Other candidates for the detection of SO_2/SO_3 will now be discussed. Li_2SO_4 possesses reasonable conductivities of 0.5 S/cm at 530 °C, 1.78 S/cm at 700 °C and 2.56 S/cm at 800 °C [63] - see Table 7-1.

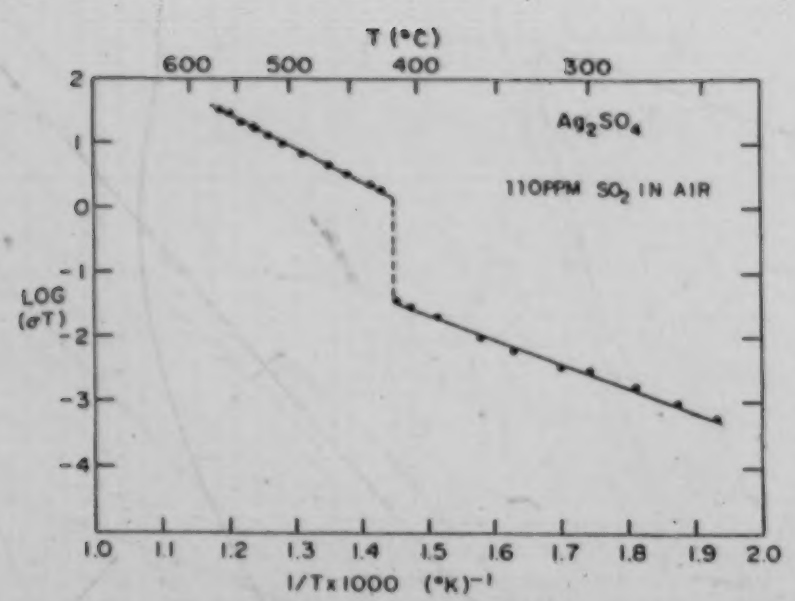

Figure 7-1. Variation of $\log(\sigma_{ionic}T)$ versus 1/T*1000 for pure Ag_2SO_4 [64].

Table 7-1. Conductivity of sulfates.

Composition	Conductivity (S/cm)	Conductivity (S/cm)	Conductivity (S/cm)
Temperature	**530 °C**	**700 °C**	**800 °C**
α-Ag_2SO_4	0.0193	-	-
23m/o Ag_2SO_4 - 77m/o Li_2SO_4 [64]	0.88	-	-
45m/o Ag_2SO_4 - 55m/o Li_2SO_4 [64]	1.17	-	-
Li_2SO_4 [63]	0.5	1.78	2.56
Na_2SO_4 [8]	0.00031	0.0021	0.005
K_2SO_4 [65]	0.00005	0.0004	0.0016

It is apparent that mixtures of Li_2SO_4 containing 23 m/o Ag_2SO_4 and 45 m/o Ag_2SO_4 possess much higher conductivity at the lower temperature of 530 °C than the other

sulfates listed. In Figure 7-2 a plot of conductivity versus temperature for 23 m/o Ag_2SO_4 -77 m/o Li_2SO_4 is provided. With the solid electrolyte Li_2SO_4-Ag_2SO_4, there are two step changes in conductivity at temperatures between 390 to 405 °C and at ~515 °C which correspond to the transition between the α and β phases, respectively, as present in pure Ag_2SO_4. Li_2SO_4 is stable in exhaust stack environments; however, unfortunately, Li_2SO_4 will decompose into Li_2S as encountered in coal gasification environments (see Figure 7-3).

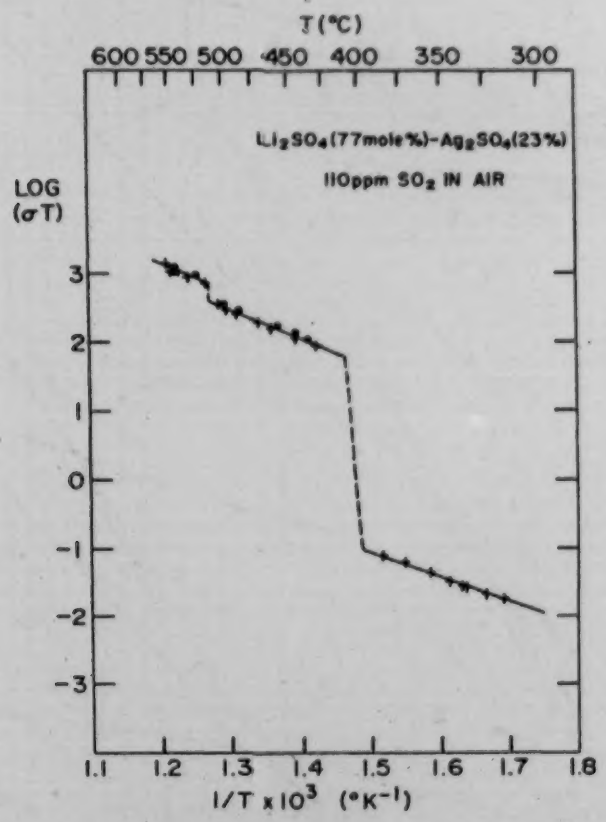

Figure 7-2. Conductivity of Ag_2SO_4 (23 m/o) – Li_2SO_4 (77 m/o).

The regions defined by ovals in the figure are in reference to exhaust stack and coal gasification environments. Regardless, the most serious problem with Li_2SO_4 is its hygroscopic nature. Fortunately, it was discovered that Ag_2SO_4-Li_2SO_4 solid

solutions are both ionic conductors and non-hygroscopic even when the Ag_2SO_4 concentration is as low as 5 mole percent (m/o) [66, 67]. In addition, for pure Ag_2SO_4, it can be seen in Figure 7-4 that Ag_2SO_4 is also stable in exhaust stack atmospheres, but not in coal gasification atmospheres.

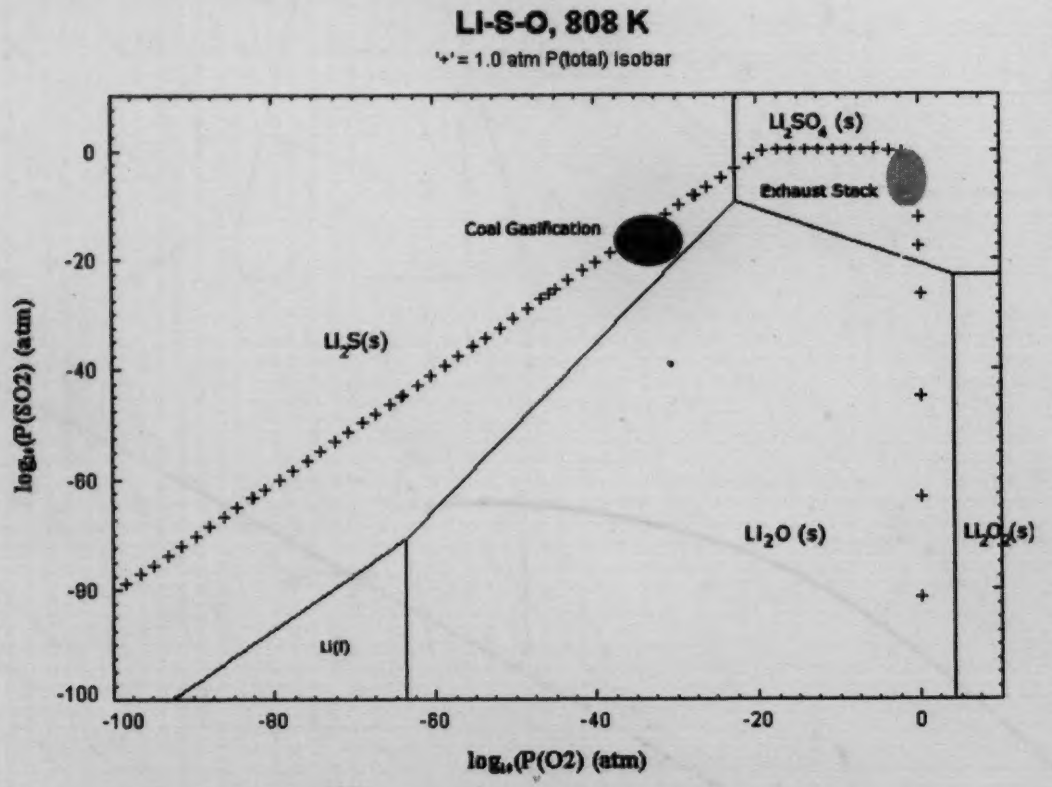

Figure 7-3. Phase stability diagram for the Li-S-O system at 808K.

According to the Li_2SO_4-Ag_2SO_4 phase diagram (see Figure 7-5), there is a two-phase region between 515-560 °C where this solid electrolyte is particularly well suited for operation in a chemical sensor. The most important benefit in operating a two-phase electrolyte sensor is the potential for long-term chemical stability. As observed in the Li_2SO_4-Ag_2SO_4 phase diagram, a variation of Ag_2SO_4 concentration from 21 to 35 m/o in the two phase region will only change the amount of each phase (i.e., $\alpha\,Li_2SO_4$ and $(Ag,Li)_2SO_4$), but not the concentration or activity of each phase. It is

also possible to utilize a solid reference electrode fabricated with a combination of silver powder and the two-phase electrolyte. In fact it would be possible to predict the buffering ability of the two-phase electrolyte according to the level of silver present in the reference electrode, especially in the case with a pure silver reference electrode.

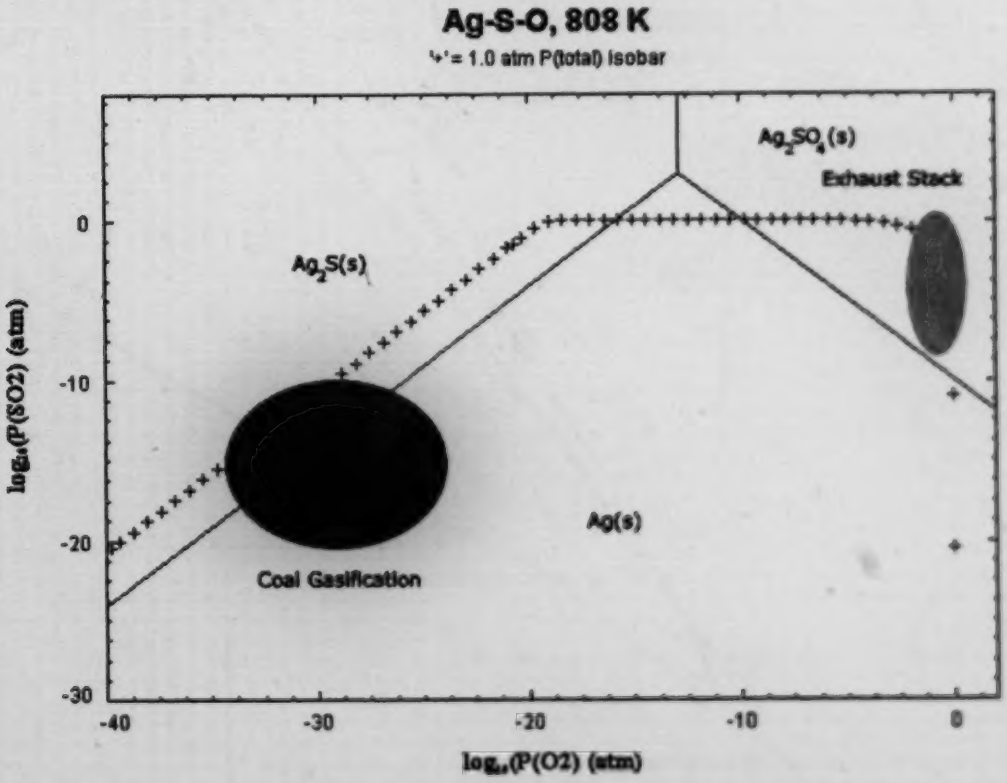

Figure 7-4. Phase stability diagram for Ag-S-O system at 808K.

As listed in Table 7-1 the conductivity of 45m/o Ag_2SO_4 -55m/o Li_2SO_4 is actually higher than that of 23m/o Ag_2SO_4 -77m/o Li_2SO_4; however, the solid electrolyte would operate in a less desirable single-phase region. Operation with this electrolyte may result in cation interdiffusion between the electrolyte and the reference electrode resulting in long-term stability problems. Therefore, the higher conductivity solid electrolyte of 45m/o Ag_2SO_4 -55m/o Li_2SO_4 is not the best choice.

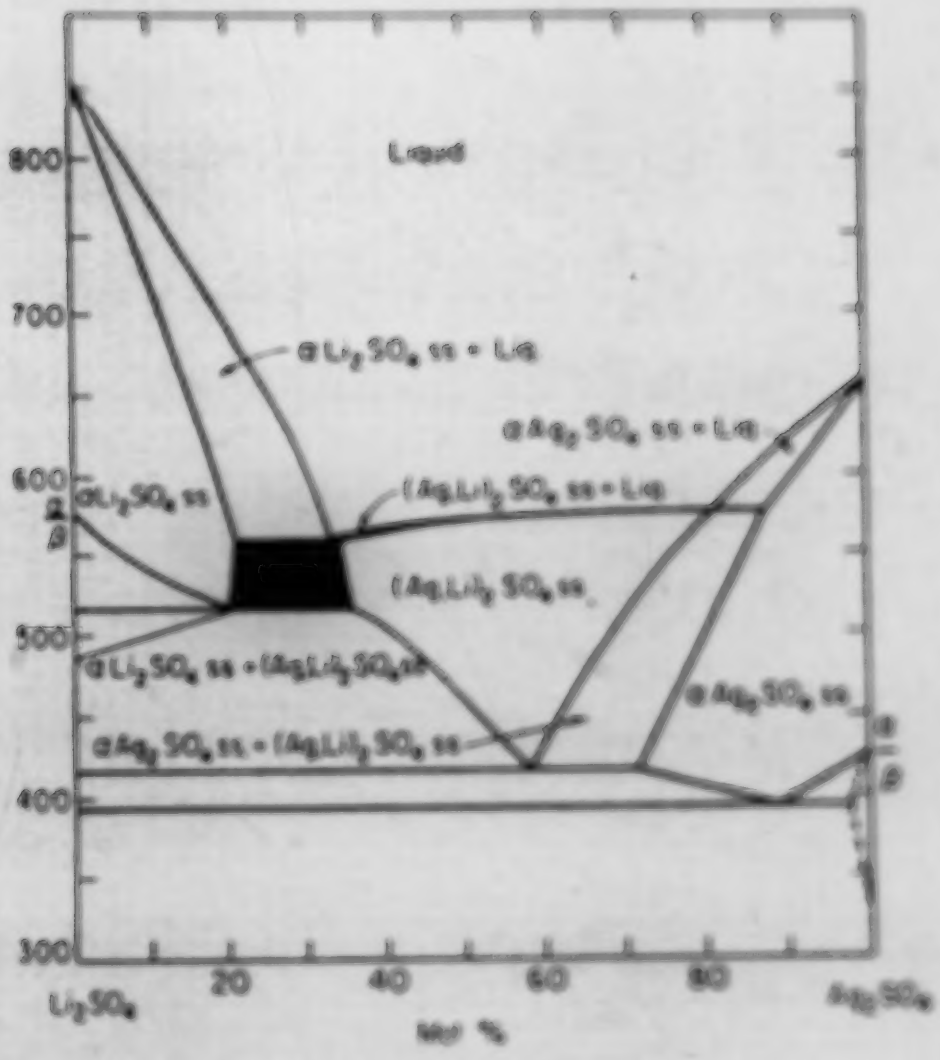

Figure 7-8. Ag_2SO_4-Li_2SO_4 phase diagram [88].

Mechanism of Conduction in Sulfate Electrolytes

In fast ion conducting sulfate solid electrolytes, the ionic conductivity is due to the cations only, with the sulfate ions forming a translationally fixed lattice. It has been determined that the activation energy for cation diffusion in fcc-Li_2SO_4 is 0.34 eV and even higher at 0.52 eV for both Li^+ and Ag^+ in bcc-$LiAgSO_4$ [69]. Both phases are also characterized by a high degree of oxygen disorder along with a high latent heat of transformation (solid-solid transition) in comparison to their heat of fusion. It has been suggested that these properties indicate a pre-melting process with rapid rotational re-ordering of the sulfate groups [70]. This was then expanded to a "paddle-wheel" model where rotations of the sulfate ions enhance the cation diffusion resulting in high conductivity [71-73]. In more typical solid electrolytes, an ionic species with the optimum ionic radius is more mobile than ions that are either smaller or larger. This is not the case for some high temperature sulfate phases where both monovalent and divalent cations are mobile. For example, the paddle wheel mechanism is present with ionic conduction in fcc Li_2SO_4, bcc $LiNaSO_4$, and bcc $LiAgSO_4$, but not with hexagonal Na_2SO_4 [69]. Studies have determined that the diffusion coefficients are in the order of 10^{-5} cm^2sec^{-1} for monovalent ions and 10^{-6} cm^2sec^{-1} for divalent cations. The diffusion coefficients for trivalent and sulfate ions are, however, much smaller [74]. In Table 7-2 values of diffusion coefficients for monovalent and divalent cations are provided.

Table 7-2. Diffusion coefficients ($D \times 10^5$ cm^2sec^{-1}) for some ions in solid sulfates

Ionic Species	fcc Li_2SO_4, 750 °C	fcc Li_2SO_4, 550 °C
Li^+	4.2	1.0
Na^+	3.7	0.93
K^+	2.1	0.44
Mg^{2+}	0.22	0.13
Zn^{2+}	0.22	
Co^{2+}	0.51	0.08
SO_4^{2-}	2.9×10^{-9}	

Reference Electrode: $Ag:Ag_2SO_4$-Li_2SO_4 Mixture

The reference material consists of silver combined as a mixture with the dopant-host sulfate electrolyte. It may also be possible to utilize pure silver as the reference electrode as in previous work with a $BaSO_4$ (0.27 mol%) – Ag_2SO_4 electrolyte [43]. If this were proven to perform properly, this change would dramatically simplify the fabrication of this sensor, especially with respect to deposition of a silver layer and the overall fabrication process.

In most cases, one is only concerned with a reaction at one of the electrodes. An experimental cell would, therefore, be constructed of a working (or indicator) electrode coupled with an electrode of known potential that approaches ideal non-polarizability, the reference electrode. Reference electrodes are utilized to fix a certain chemical potential in the sample next to the interface with the electrolyte. The reference electrode's potential should be constant enough so that any change in potential due to current, time or other variables is sufficiently small and that the overall cell measurement is not adversely affected. They are expected to maintain their chemical potential even when material is either removed or added to the reference electrode. An example would be pure metal references such as Ag electrodes that retain a constant chemical potential, regardless of mass loss or mass gain. Pressed mixtures of CuO/Cu_2O, which maintain fixed oxygen and copper chemical potentials regardless of changes in overall oxygen content, is an example of how a reference electrode should perform.

The factors in selecting a reference electrode consist of the following:

- The materials utilized in constructing the reference electrode should be readily available and easy to fabricate. Air is always present and platinum is the best established electrical lead material in potentiometric cell studies. Even with condensed phase reference electrodes such as CuO/Cu_2O for oxygen sensors, platinum is invariably used as the lead wire.

- Reference electrodes should be highly reversible and, therefore, not polarized easily. A highly reversible electrode would be indicative of a good electronic conductor with high oxygen diffusivity over the required temperature range of operation. Solid phase reference electrodes typically get polarized irreversibly on passing macroscopic quantities of charge. This is particularly important in coulometric studies where a calculated number of coulombs of electrons is passed through the cell. Reference electrodes for oxygen measurements have been ordered with respect to reversibility as follows [75]:

  $$CuO/\ Cu_2O\ >\ Fe/\ Fe_xO\ >\ Ni/NiO > Cr/Cr_2O_3$$

  Air/Pt and O_2/Pt reference electrodes are considered to be far superior to even Cu_2O/CuO [76, 77].

- Inert gases containing O_2 could be used as reference electrode materials combined with a platinum lead. However, these electrode systems display considerable flow rate dependence of cell voltage depending on the oxygen content of the inert gas carrier gas [78-80]. The same phenomena is also experienced with H_2/H_2O or CO/CO_2 buffer gas mixtures [76]. In contrast, reference electrodes consisting of O_2/Pt or air/Pt are almost unaffected by flow rate with air/Pt and even working with a static air supply.

- The reference electrode should also be well characterized thermodynamically. Considerable work has been performed with the oxides Cu_2O and NiO which satisfy this criteria very well [81]. For Fe_xO, the ΔG_f° has been well assessed after an analysis of numerous published papers prior to 1973 [82]. However, since this publication, sufficient evidence has appeared for revising these data [83]. The best metal/metal oxide reference electrodes possess an uncertainty in the range of ± 200 J. These reference electrodes consist of either air/Pt or O_2/Pt which display minimum uncertainty [84].

- The reference electrodes should have a small dependence on temperature of their associated chemical potential. For example M/MO_x reference electrodes have a steeper temperature dependence owing to the significant value for $\Delta S^o_{O_2}$ of oxygen. Whenever the temperature of a galvanic cell is changed, the chemical potential will require time to readjust to a value close to that of the phase boundary between the metal and the coexisting metal compound (e.g., metal oxide). Also, if the mutual solubility of the metal and its oxide changes rapidly with temperature, more time will be required to reach equilibrium during thermal cycling. In the case of the air/Pt reference electrode the P_{O_2} is temperature independent; therefore, there is no readjustment of the composition at the phase boundary.

- The reference electrode material should be inert chemically with respect to the electrolyte and the electrical lead. It is well known that the condensed phase electrodes have high temperature restrictions with respect to inertness.

- A wide temperature range of applicability is a required characteristic of a reference electrode. For example, it is relatively easy to obtain ΔG^o_f data from emf measurements but not so with entropy data. This is due to large uncertainties in the temperature coefficient of emf over relatively narrow experimental temperature ranges. If the experimental range is increased, more reliable entropy data could be acquired. However, condensed phase reference electrodes are frequently restricted in temperature range due to: low temperature irreversibility, solid state transitions such as melting or vaporization, and high temperature chemical reactivity with the electrolyte and/or lead. In comparison, the air/Pt reference electrode provides emf measurements over several hundreds of degrees and, therefore, is considerably more accurate in the calculation of entropy.

Working Electrode: Platinum Thin Film

Alternative names for this electrode consist of indicating electrode or test electrode in addition to working electrode. This is the electrode at which the electrochemical phenomena is measured and may be constructed of inert materials, but not always. The working electrode always exists as a separate physical electrode from the reference electrode and, if present, also separate from the auxiliary electrode. In a three-electrode arrangement, an auxiliary or counter-electrode serves as a source or sink for electrons so that current can be passed through the cell. Typically, the current or potential of the auxiliary electrode is not known or measured.

The critical factors to consider in the performance of the working electrode consist of:

- Stability of the electrode and electrolyte with respect to temperature and gas atmosphere. If the electrode and electrolyte materials chemically react with the gas atmosphere and form compounds, the interfacial impedance will increase. Pt is assumed to be inert with respect to high-temperature oxidation; however, there is some evidence that various oxygen compounds form on the surface of Pt [85]. In the case of a sulfur oxide sensor, the presence of SO_2/SO_3 in the gas stream may result in the formation of Pt-sulfide compounds.

- The kinetics of the working electrode reactions which determine the exchange current density must be fast enough to maintain equilibrium conditions in a potentiometric sensor. These kinetics will be a function of temperature, gas concentration, electrode and electrolyte materials, and the length of "triple phase boundary" (TPB) presented by the working electrode. The working electrode reactions are described by a combination of mass transfer of gaseous species through a porous electrode (Pt deposited on electrolyte surface), adsorption and surface diffusion of reactant gas species. In this work with the sulfur oxide sensor, there will be a series of steps including adsorption of O_2

and SO_3 molecules, followed by surface diffusion, and combination and reduction of the adsorbed species resulting in the formation of SO_4^{2-} in the solid electrolyte. These reactions will occur at the T.P.B. between the gas phase, platinum electrode and electrolyte material. It is important that the T.P.B. area is maximized to ensure the highest possible sensitivity and shortest response times in a chemical sensor.

- If the gases at the working electrode are not in thermodynamic equilibrium at the electrode surface and at the interface to the solid electrolyte, mixed potentials will result. This is determined by the kinetics of the different electrode reactions and by the catalytic reactions at the electrode surfaces. In the sulfur oxide sensor this would involve the kinetics of the reaction $SO_3 + \frac{1}{2}O_2 + 2e^- \rightleftharpoons SO_4^{2-}$. To some degree the kinetics of the reaction of $SO_2 + \frac{1}{2}O_2 \rightleftharpoons SO_3$ may have some influence on the cell potential; however, the inclusion of a significant amount of Pt catalyst upstream from the working electrode should minimize this contribution.

- A good match of thermal expansion coefficients (TEC) is required between the working electrode and the electrolyte; otherwise stresses will develop resulting in separation or delamination of the two layers. If utilizing a thin film for the electrode as in this work, additional consideration must be given for the chosen materials. The T.E.C.s for the deposited thin films differ from the bulk material values depending on the method of deposition and the thickness of the deposited thin film. For example, the TEC for thin film aluminum varies from 18.2 ppm/°C to 9.0 ppm/°C when the thickness varies from 0.3 to 1.7 μm [86]. There are various methods which can be utilized to measure the TEC of deposited thin films including micro-machined cantilevers [86] and X-ray analysis [87].

- Adequate adhesion combined with good electrical/ionic contact with the electrolyte is necessary. Adhesion between the thin films and the substrate, in this case the electrolyte, is extremely important for overall performance and reliability of a chemical sensor. Classical adhesion tests [88] consist of the scotch tape test, scratching, bending, pulling and the deceleration techniques (ultrasonic and ultracentrifuge). The cleanliness of the surface also has a significant influence on the adhesion of the thin film. The addition of surface roughness will provide more surface area and result in mechanical locking. Adhesion is enhanced through the formation of intermediate compounds between the thin film and the electrolyte, resulting in the reduction of stress between the two materials due to different thermal coefficients of expansion and through the formation of a strong mechanical bond between the two layers.

- Variations in the conductivity/resistivity of a metal correspond to changes in the mean free path of the conduction electrons. An electron will experience a reflection when it reaches a surface. When the thin film becomes thinner the electrons will increasingly reflect off the surfaces and once the internal dimensions of the film become comparable to the mean free path of the electrons, the resistivity will increase. The surface scattering of electrons at room temperature becomes important in pure metals of thickness less than between 2 to 300Å, depending on the metal. On the other hand as the temperature is increased the mean free path of electrons is dramatically reduced (see Table 7-3). Therefore, at higher operational temperatures, the thickness at which surface reflections of electrons becomes significant is actually reduced, compared to room temperature. As can be observed in Table 7-3 the mean free path for Pt is only 79 Å at 100 °C. From these facts it can be concluded that in the operation of the Li_2SO_4-Ag_2SO_4 sensor at 535 °C, the Pt working electrode would not experience reductions in conductivity due to electron scattering. However, there will be a decrease in conductivity due to the temperature coefficient of resistivity (T.C.R.) according to bulk material

considerations. The T.C.R. is defined as the fractional change in resistivity per unit temperature increase from a reference temperature, T_o, usually at 273.15K.

- The cost of electrode materials is an important consideration in the fabrication of typical chemical sensors. However, material costs become less of a concern when deposition of thin films is involved. This is especially true with an integrated sulfur oxide sensor as the Pt being deposited is less than 1 μm in thickness.

Table 7-3. Electronic mean free path of several metals.

Metal	Calculated (Å)	Mean Free (Å)	Path (Å)	Temp. Coeff. Resistivity (T.C.R.) ppm/°C (0-100 °C)
	-200 °C	**0 °C**	**100 °C**	
Li	955	113	79	4220
Na	1870	335	233	4400
K	1330	376	240	5500
Cu	2965	421	294	4330
Ag	2425	575	405	4100
Au	1530	406	290	4000
Ni	-	133	80	6750
Co	-	130	79	6580
Fe	2785	220	156	4110
Pt	720	110	79	3920

Chapter 8: Theoretical Considerations-Sulfur Oxide Sensor

Theoretical Cell Voltage

The sensor consists of a solid-state reference electrode or anode in combination with a working electrode or cathode, which is exposed to a gas flow containing SO_2 in air. For this sensor the following reactions apply:

$$2Ag^{+} + SO_3 + \tfrac{1}{2}O_2 + 2e^{-} \rightleftharpoons Ag_2SO_4 \qquad \oplus \text{ Cathode - Working Electrode} \qquad (8.1)$$

$$2Ag \rightleftharpoons 2Ag^{+} + 2e^{-} \qquad \ominus \text{ Anode – Reference Electrode} \qquad (8.2)$$

$$2Ag + SO_3 + \tfrac{1}{2}O_2 \rightleftharpoons Ag_2SO_4 \qquad \text{Overall Sensor Reaction} \qquad (8.3)$$

Accordingly, the voltage of the sensor is defined by the following equation:

$$E = E^{o} + \frac{RT}{2F} \ln \frac{\left(P_{O_2}\right)^{1/2}\left(P_{SO_3}\right)}{a_{Ag_2SO_4}} \qquad (8.4)$$

where E is the measured cell voltage and E^{o} is the standard voltage of the overall sensor reaction (Equation 8.3) under standard conditions at the operating temperature. The partial pressure of oxygen P_{O_2} at sea level is equivalent to 0.2095 atm due to the air in the air-SO_2 mixture. The activity of Ag_2SO_4 ($a_{Ag_2SO_4}$) in a two-phase mixture of 77 m/o Li_2SO_4 – 23 m/o Ag_2SO_4 has been stated as being equal to 0.25 at 530 °C according to the literature [40, 89] .

The partial pressure of the sulfur trioxide (P_{SO_3}) at the working electrode is related to the partial pressure of the sulfur dioxide entering the sensor ($P_{SO_2(in)}$) by:

$$P_{SO_3} = \frac{P_{SO_{2(in)}}}{\left(1 + \frac{1}{K_p \left(P_{O_2}\right)^{1/2}}\right)} \qquad (8.5)$$

where $P_{SO2(in)}$ is the partial pressure of the sulfur dioxide in the incoming gas stream, K_p is the equilibrium constant for $SO_2 + \frac{1}{2}O_2 \rightleftharpoons SO_3$ at the sensor operating temperature, P_{O_2} is the partial pressure of oxygen in the gas stream, and P_{SO_3} is the partial pressure of sulfur trioxide measured at the working electrode.

Utilizing published thermodynamic data [60, 90], the value for E^o was calculated to be equal to 0.6571 ± 0.0391 V at 535 °C or 0.6685 ± 0.0391 V at 525 °C (see Appendix C). Since atmospheric pressure was observed to range between 690 to 710 mm Hg, therefore assuming an average of 700 mm Hg, $P_{O_2} = \left(\frac{700}{760}\right) 0.2095\,atm = 0.1930\,atm$.

The activity for silver sulfate, $a_{Ag_2SO_4}$, is quoted as being equal to 0.25 at 530°C in the literature [43, 89], however it was determined experimentally to be equal to 0.2932 ±0.0242 at 535 °C or 0.3714 ±0.0276 at 525 °C (see Chapter 11, Calculation of Ag_2SO_4 Activity). In addition, (ppm SO_2) = $1 \times 10^6 P_{SO_2(in)}$.

It follows that the theoretical voltage ($E_{theoretical}$) of the sensor at 535 °C is:

$$E_{535°C}(V) = (0.1839 \pm 0.0391) + (0.08018 \pm 0.00020) \log(\text{ppm}SO_2) \qquad (8.6)$$

The theoretical cell voltage ($E_{theoretical}$) at 525 °C is:

$$E_{535°C}(V) = (0.1963 \pm 0.0391) + (0.07919 \pm 0.00020) \log(\text{ppm}SO_2) \qquad (8.7)$$

The error in the y-intercept (i.e., ±0.0391) and the slope (i.e., ±0.00020) is described in Appendix D.

Chapter 9 : Experimental Sulfur Oxide Sensor – Fabrication Process

Thick Film Sulfur Oxide Sensor Fabrication

In this work the sulfur dioxide/trioxide sensor was constructed with various reference electrode configurations consisting of either: 2:1 weight ratio composite mixtures of $Ag:Li_2SO_4$-Ag_2SO_4 in the form of a disc or thick film paste, or a thin or thick film of Ag deposited onto a solid electrolyte substrate (see Figure 9-1). The solid-state electrolyte substrate is formed by compressing a mixture of 75 mol% lithium sulfate powder (Li_2SO_4 - 99.9993% pure from Aldrich Chemical Co.) and 25 mol% silver sulfate powder (Ag_2SO_4 - 99.9999% pure from Aldrich Chemical Co.) in a carbide lined steel die at 280 MPa. These substrate discs were then sintered in a furnace atmosphere consisting of 500 ppm of SO_2 in air for two days at 535 °C.

For construction of the various sensor designs, the reference electrodes were as mentioned either: thin or thick films of Ag, or a composite in disc form or as a thick film consisting of a 2:1 weight ratio of Ag: Ag_2SO_4-Li_2SO_4. The thin film material (Ag- 99.99% pure) utilized for deposition of Ag was acquired from Kurt J. Lesker Company of Pittsburgh, PA. Thick film material (silver conductor, 903-A) utilized for fabrication of the Ag thick film reference was acquired from ESL Electro-Science (King of Prussia, PA). This material is a lead free conductor designed for use with ceramic tapes. The material utilized for fabrication of the composite reference electrode consisted of Ag powder (99.99+%, -325 mesh from Aldrich Chemical Co.) mixed with the electrolyte (25 mol% Ag_2SO_4 and 75 mol% Li_2SO_4) in a 2:1 weight ratio. When used to form a thick film this powder was, in turn, mixed with an organic carrier consisting of: butyl cellusolve, terpenieol, phenoxypropanol and butyric acid to form the suspended thick film. The powder content and chemical composition of the carrier were adjusted so as to obtain the optimum viscosity and flow characteristics for this application. The thick film was then deposited via a silk screen onto the solid-state electrolyte substrate. The reference electrode produces a constant chemical potential at the operating temperature of 535 °C.

The working electrode is exposed to a flow of SO_2 in air, which is converted to SO_3 in a Pt containing quartz chamber, consisting of a porous thin film structure of Pt. The cylinder gas mixtures utilized in the testing of the sensor were certified mixtures accurate to ±1% supplied by Liquid Air Products. On the face of the sensor at the working electrode, a porous Pt thin film facilitates the reaction $SO_3 + \frac{1}{2}O_2 \rightleftharpoons SO_4^{2-}$ due the abundance of the TPB areas. A previous investigation by Imanaka et al. [91] proved the advantage of utilizing sputtered thin films of platinum. In this work, a platinum thin film about 10,000 Å (1 μm) thick was deposited via evaporation onto the reference electrode side of the sensor to ensure good electrical contact. For contact to the external electrical circuit and the electrometer/voltmeter, a platinum gauze with an attached Pt lead wire was placed against the working electrode. Contact at the reference electrode was made with a solid Pt foil disc and attached Pt lead.

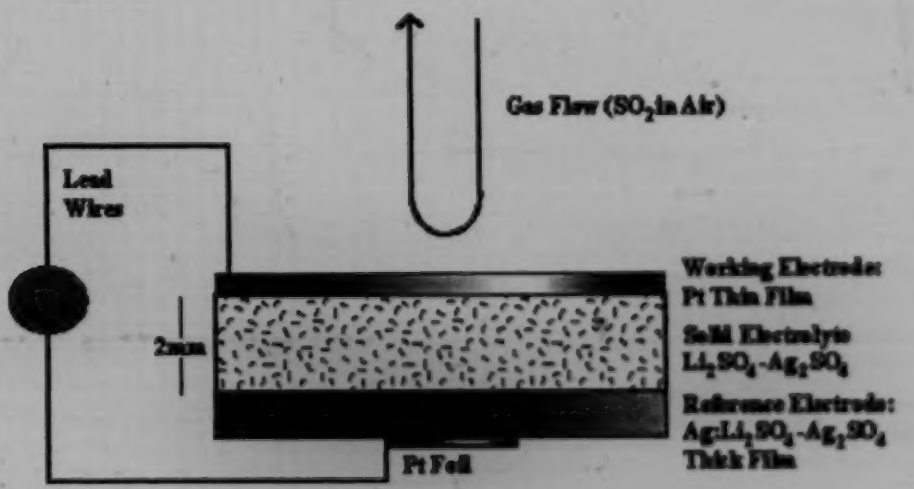

Figure 9-1. Construction of thick film reference cell structure.

Considerable work was performed towards the development of a miniaturized and integrated sulfur oxide (MISOX) sensor through a series of screen patterned thick film depositions of the various layers. These layers or patterns of thick film depositions consisted of the following:

Layer No. 1: Deposition of Reference Electrode

Mask No. 1 consisted of the reference mask. This layer had two purposes: first to provide the reference electrode consisting of the silver and electrolyte mixture, and second to define the alignment marks required for the subsequent layers.

Layer No. 2: Deposition of Electrolyte Layer

The next deposition consisted of the solid electrolyte mixture (25m/o Ag_2SO_4 - 75m/o Li_2SO_4) which was placed in contact to the underlying reference electrode. This layer was found to be the limiting factor in fabrication of the integrated sensor. Further work is required to produce a functional solid electrolyte.

Layer No. 3: Deposition of Platinum Contact/Working Electrode Layer

This layer provides electrical contact onto the underlying electrolyte and also functions as the working electrode. Due to the thickness of the electrolyte, a thin film platinum layer was deposited directly onto the electrolyte which is then followed by a platinum gauze.

Layer No. 4: Deposition of Final Sealing Layer

The final layer to be deposited consists of Mask No. 4. This layer consists of an alumina based paste which forms a sealant to the overall structure.

Since difficulties were experienced in fabricating non-porous thick films of the electrolyte (25m/o Ag_2SO_4 – 75m/o Li_2SO_4), miniaturization and integration of the sulfur oxide sensor were not pursued at this time. Once a suitable thin or thick film deposition technique for the electrolyte is developed, further work on the miniaturized

sensor could proceed. This device consists of the thick film reference and platinum contact layers deposited onto the substrate consisting of an alumina disc. Much smaller dimensions and, therefore, faster response times and low power consumption would be possible through the use of thin and thick films. In Figure 9-2, a cross section of the proposed miniaturized device is provided.

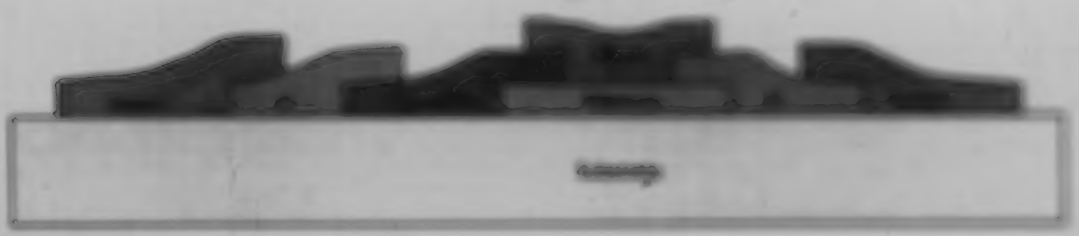

Figure 9-2. Cross-section of proposed Micro-Integrated Sulfur Oxide (MISOX) sensor.

Chapter 10 : Cell Design and Operation

In the test apparatus, a ceramic fixture was utilized in the centre of the furnace which was a machined piece of MACOR, a machinable ceramic consisting of 55% fluorophlogopite mica and 45% borosilicate glass manufactured by Corning Incorporated (Corning, NY). This material is suitable for a continuous operating temperature of 800 °C and a peak temperature of 1000 °C. It also possesses a DC resistivity of $>10^8$ Ωcm at 535 °C, more than adequate for this application. The machined MACOR piece holds the electrolyte disk in place by a threaded ring (see Figure 10-1). The working electrode side of the cell is exposed to the SO_2 gas flow, with a solid Pt foil and external Pt lead contacting the reference electrode side. A pair of bolted metal plates outside the cell compresses the ceramic tubes together. The SO_2 containing gas mixtures were certified accurate to within ± 1% from the gas cylinders and were mixed via a set of calibrated electronic mass flow controllers (Tylan Ltd.) calibrated to within ± 1% of the flow rate. The primary gas cylinders consisted of mixtures of 5.4, 11.6, 100, 500, and 2400 ppm SO_2 in air. The gas from the primary cylinders was then mixed with clean dry air by the electronic mass flow controllers to the required concentrations. Measurements of the cell emf were made at an operational temperature of either 535 °C or 525 °C.

The input mixture of SO_2 and air to be measured by the sensor was passed through a quartz tube with a catalytic chamber containing cut up platinum gauze and foil. This chamber assured the complete conversion of SO_2 to SO_3. For automated control of the furnace and sensor, a computer control and data acquisition system was assembled. This consisted of a LabView combination software/hardware system that controlled all aspects of the experimental conditions and acquisition of experimental data. In Figures 10-2 and 10-3 the front panel of the computer control system is displayed. This system allowed for control of both total flow rate and SO_2 concentration of the gas mixtures. It is possible to either manually control the SO_2 concentration or to program the concentration automatically with an initial SO_2 concentration and timed step increments or decrements in concentration. The data collected consisting of cell

voltage, temperature, mass flow rate and SO_2 concentration were written to disk with a time-date stamp.

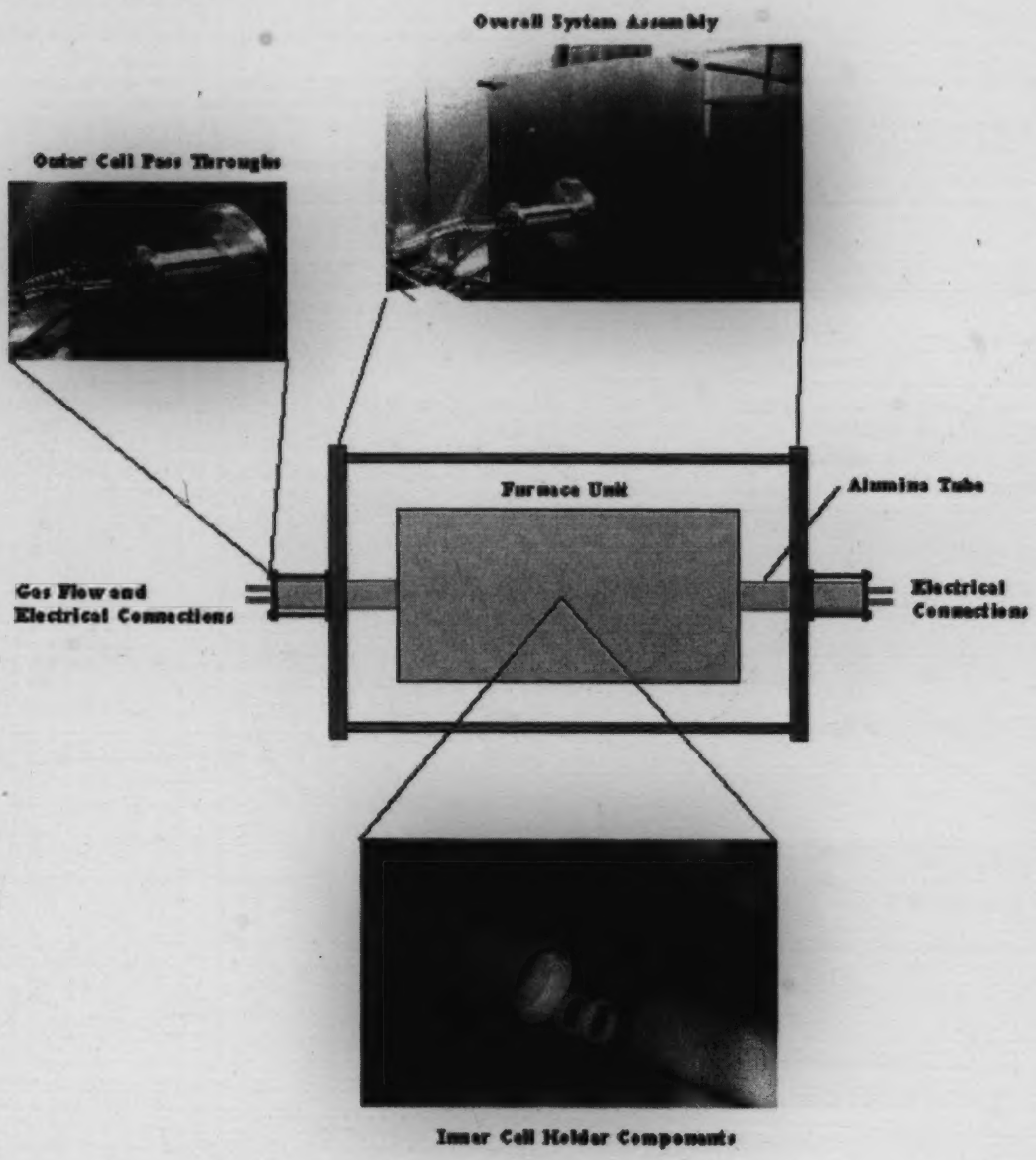

Figure 10-1. Inner cell construction.

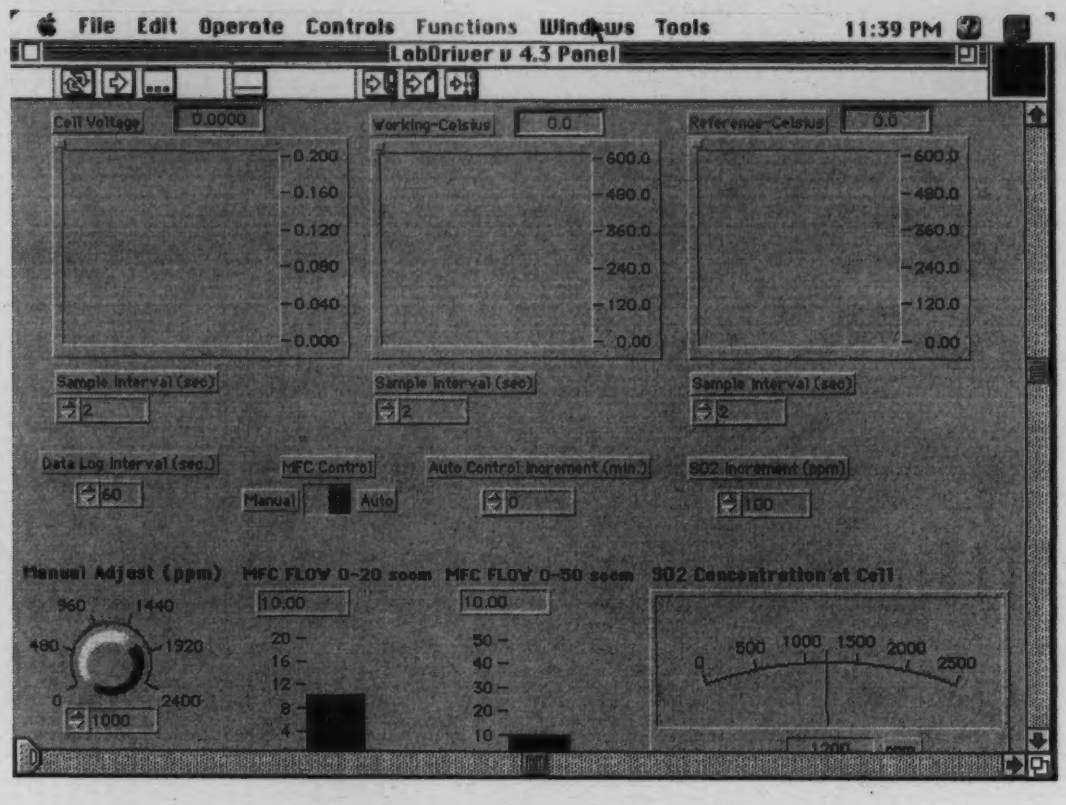

Figure 10-2. Control panel for computer control system – Part I.

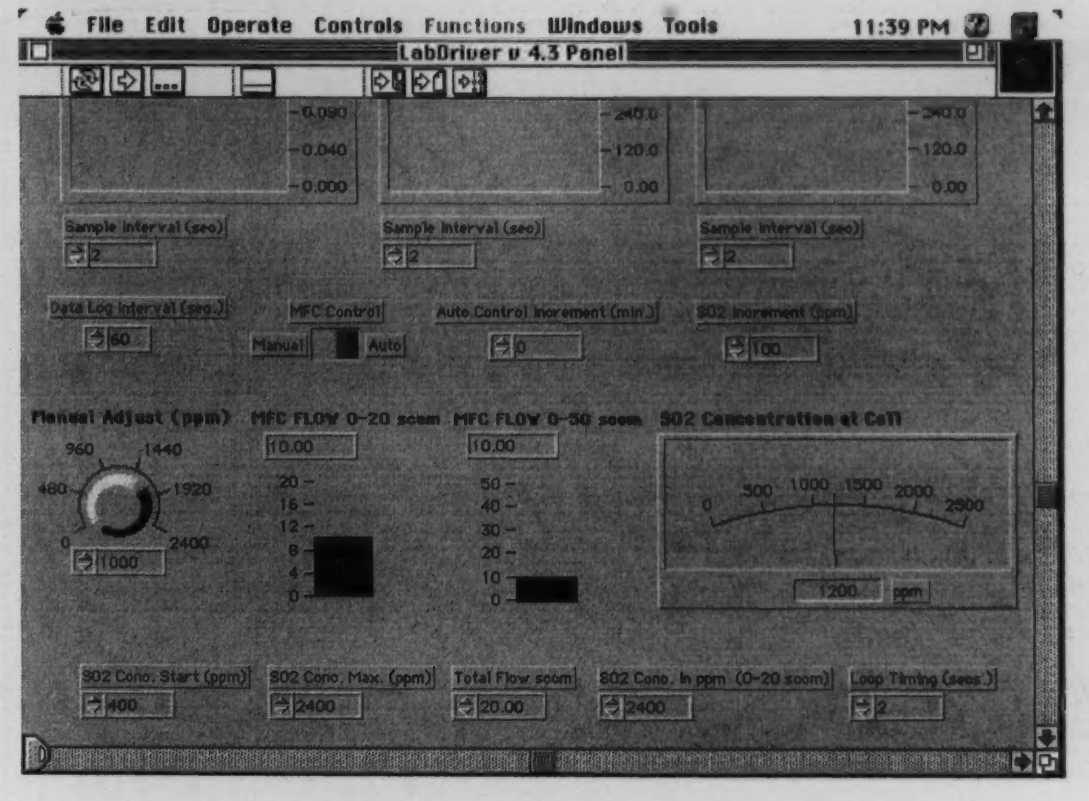

Figure 10-3. Control panel for computer control system – Part II.

Chapter 11 : Experimental Results

Cell No. 1: Composite Reference Electrode

This cell consists of a disc with a diameter of 25.4 mm constructed with the following layers:

- the working electrode consists of an 80 mesh Pt gauze, which is connected to the external voltage measuring equipment via a Pt lead
- a 2 mm thick layer of solid electrolyte consisting of 25 m/o Ag_2SO_4 – 75 m/o Li_2SO_4
- a composite reference electrode consisting of a 2:1 weight ratio mixture of Ag: 25m/o Ag_2SO_4 – 75m/o Li_2SO_4, 2 mm thick, and a Pt foil which was connected to the external voltage measuring equipment via a Pt lead

The construction of this sensor is depicted in Figure 11-1.

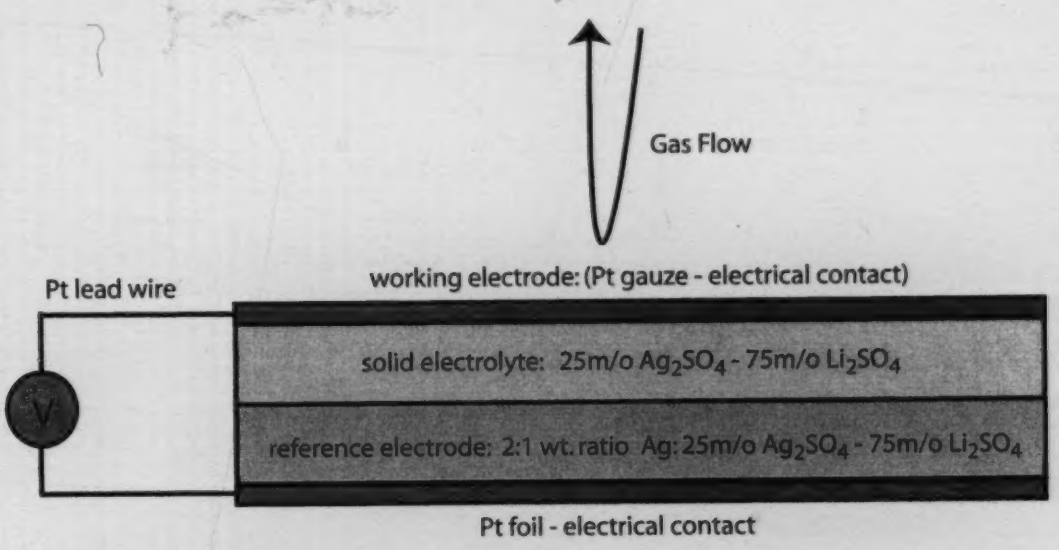
Gas Flow
Pt lead wire
working electrode: (Pt gauze - electrical contact)
V
solid electrolyte: 25m/o Ag2SO4 - 75m/o Li2SO4
reference electrode: 2:1 wt. ratio Ag: 25m/o Ag2SO4 - 75m/o Li2SO4
Pt foil - electrical contact

Figure 11-1. Cell No. 1: composite reference - construction schematic.

This sensor produced a cell voltage versus the log of ppm of SO_2 in air at an operating temperature of 535 °C as displayed in Figure 11-2. The data for this experimental run are listed in Appendix A in Table A-1. Each data point consists of

an average of 10 measurements made over five minutes. In addition, each measurement was obtained via a "box car average" consisting of hundreds of individual measurements. This method for collection of experimental data was utilized throughout the experimental work. The data were collected continuously in increments of between 5 and 30 ppm SO_2 (as listed in Table A-1) when either rising or decreasing in concentration. The cell was found to be repeatable with the STDEV error in cell voltage between 0.0010 to 0.0014 Volts over all measurements. The best fit line for these data was found to be:

$$Emf(V) = (0.2176 \pm 0.0043) + (0.0725 \pm 0.0016)\ log[SO_2 - ppm] \quad (94 - 900\ ppm\ SO_2)\ R^2 = 0.9847 \tag{11.1}$$

The theoretical cell equation for 535 °C (see Appendix D for derivation) is given by:

$$Emf(V) = (0.1839 \pm 0.0391) + (0.08018 \pm 0.0002)\ log[SO_2 - ppm] \tag{11.2}$$

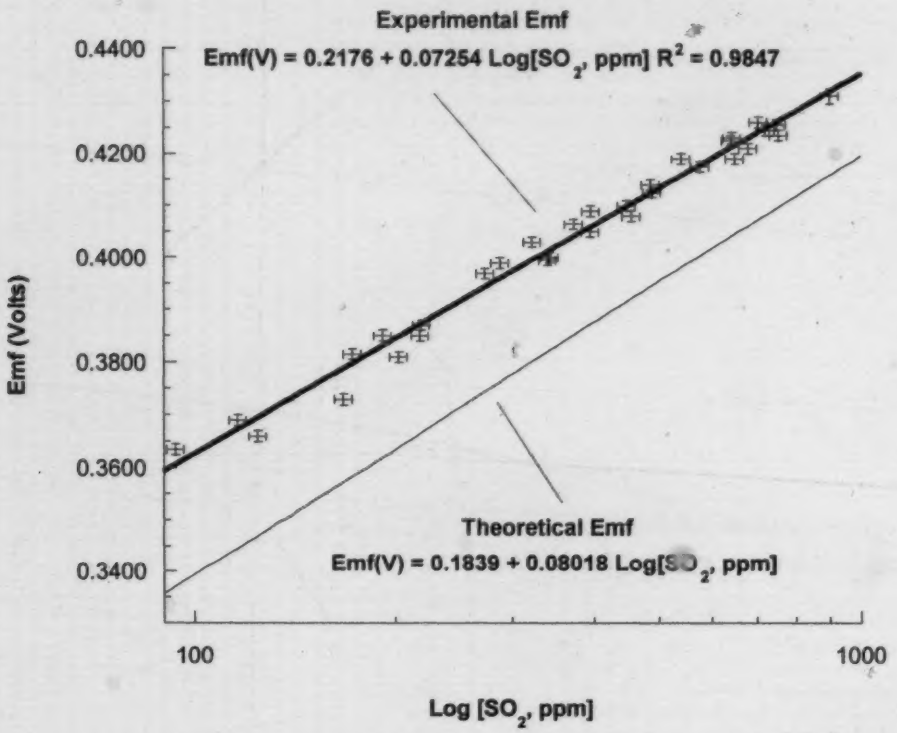

Figure 11-2. Cell No. 1: composite reference electrode - Emf versus log (SO_2-ppm) from 94 to 900 ppm SO_2 in air.

The error associated with the emf(V) present in Figure 11-2 and all subsequent figures is related to the STDEV of the measured emf as listed in the data tables. In addition, the error in the mixed SO_2 concentration is due to the mixing of two gas streams: air and the SO_2 cylinder mixture (±1%, certified mixture), via two electronic mass flow controllers (MFCs) each with an error of ±1% of the full scale flow rate, resulting in a total error of ±5% of the absolute value for each supplied gas concentration.

Cell No. 2: Ag thin film reference electrode

This cell consists of a disc with a diameter of 25.4 mm constructed with the following layers:

- a working electrode consisting of a Pt thin film 0.5 μm (5000 Å) thick, deposited onto the solid electrolyte material combined with an 80 mesh Pt gauze and Pt lead for connection to the external voltage measuring equipment
- a 2 mm thick layer of solid electrolyte consisting of 25 m/o Ag_2SO_4 – 75 m/o Li_2SO_4
- the reference electrode consisting of a 0.8 μm (8000 Å) thick Ag layer and a Pt foil which is connected to the external voltage measuring equipment via a Pt lead

The construction of this sensor is depicted in Figure 11-3.

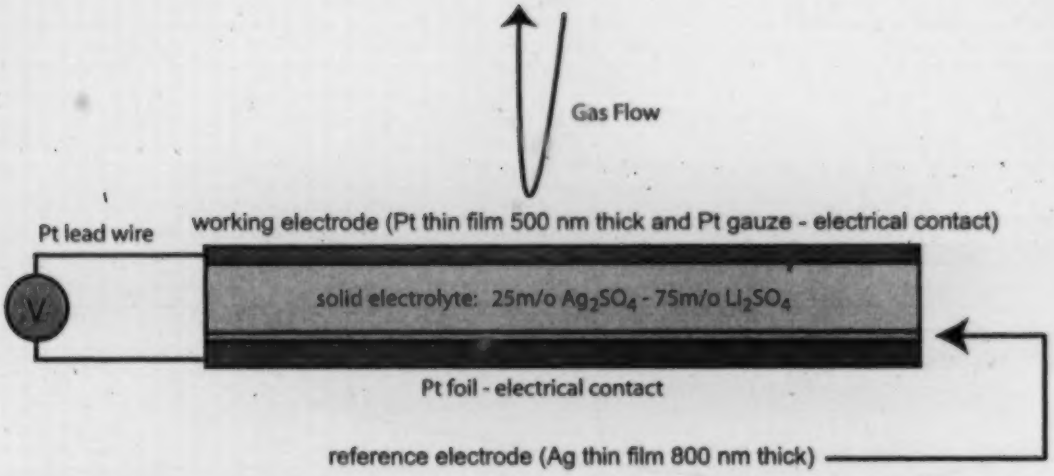
Gas Flow
Pt lead wire
working electrode (Pt thin film 500 nm thick and Pt gauze - electrical contact)
V
solid electrolyte: 25m/o Ag_2SO_4 - 75m/o Li_2SO_4
Pt foil - electrical contact
reference electrode (Ag thin film 800 nm thick)

Figure 11-3. Cell No. 2: thin film reference - construction schematic

This cell was operated for several weeks and in Figure 11-4 the results show the emf of cell No. 2 over time – with the concentration fixed at 496 ppm and the cell held at 535 °C. The data for this experimental run are listed in Appendix A, Table A-2. It is apparent that the emf of the cell was somewhat unstable, with a trend towards higher cell emfs over time. However, there was a clustering of measurements around the theoretical cell emf (0.396 Volts) at 496 ppm SO_2 in air. As a test of reversibility, the electrical leads were disconnected (initial cell voltage at 0.4465 V) for a couple of minutes and then reconnected at which time the cell emf returned to 0.4475 V. This check indicates that the cell was displaying reversibility during this portion of the test run.

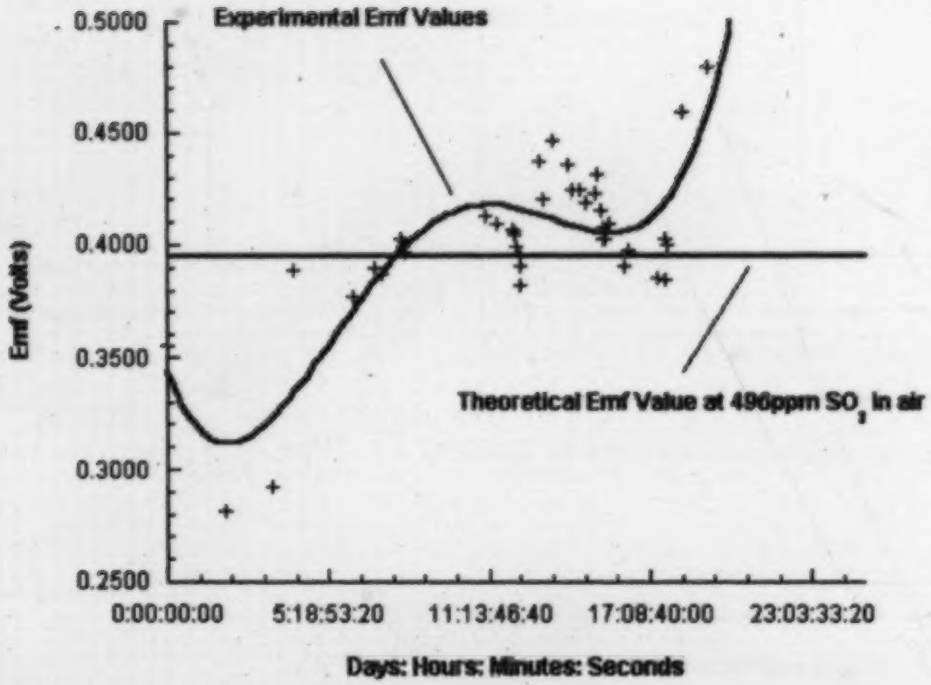

Figure 11-4. Cell No. 2: Ag thin film reference electrode – Emf versus time at 496 ppm SO_2 in air.

During operation of this cell at approximately half-way through the test, the relationship between flow rate and emf was examined and is presented in Figure 11-5. The data for this experiment are listed in Appendix A, Table A-3. In long term testing, this cell displayed instability in the measured emf. This is apparent in the large variance as indicated by the error bars in the direction of the y-axis (emf(V)) at low flow rates in Figure 11-5. The error present along the flow rate axis is equivalent to ±1% of the full scale range of the electronic mass flow controller (M.F.C.). Since the M.F.C. had a range of 0-200 sccm, the error in flow rate equals ±2 sccm. There appears to be an optimum flow rate in the range between 30-50 sccm.

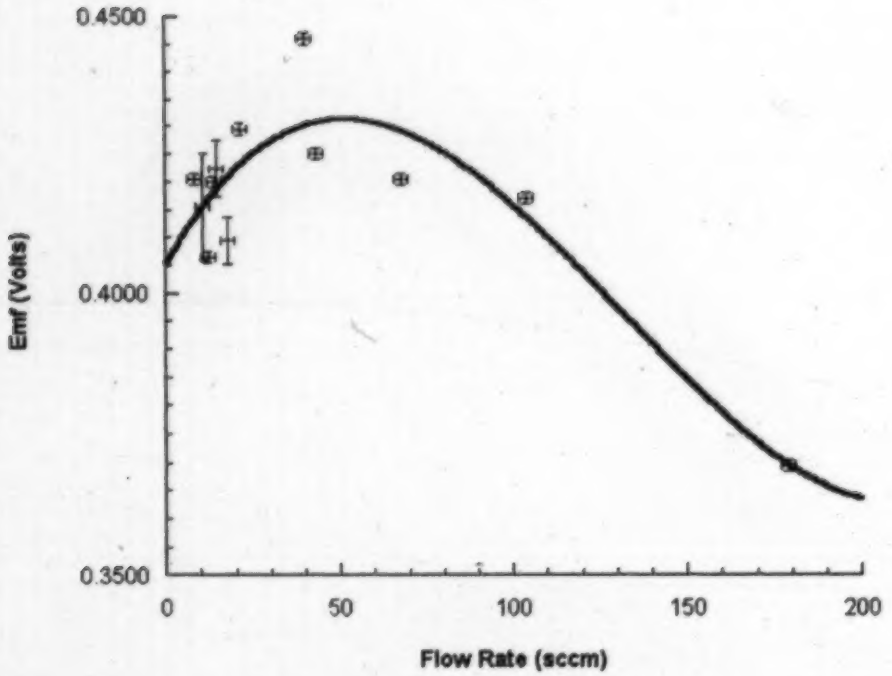

Figure 11-5. Cell No. 2: Ag thin film reference electrode - Emf versus flow rate, 496 ppm SO_2.

Cell No. 3: Ag thick film reference electrode

For cell No. 3, the Ag thin film utilized in cell No. 2 was replaced with a Ag thick film approximately 25 μm (250,000 Å) thick. This cell consists of a disc with a diameter of 25.4 mm constructed with the following layers:

- the working electrode consisted of a Pt thin film 0.5 μm (5000 Å) thick, deposited onto the solid electrolyte material combined with an 80 mesh Pt gauze and Pt lead for connection to the external voltage measuring equipment
- a 2 mm thick layer of solid electrolyte consisting of 25 m/o Ag_2SO_4 – 75 m/o Li_2SO_4
- the reference electrode consisted of a 25 μm thick Ag layer and a Pt foil which is connected to the external voltage measuring equipment via a Pt lead

The construction of this sensor is depicted in Figure 11-6.

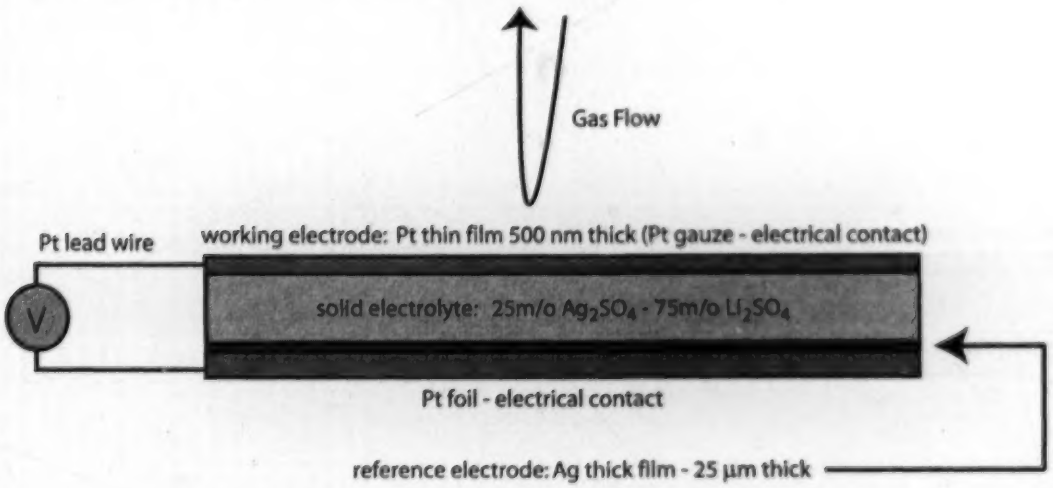
Gas Flow
Pt lead wire
working electrode: Pt thin film 500 nm thick (Pt gauze - electrical contact)
V
solid electrolyte: 25m/o Ag2SO4 - 75m/o Li2SO4
Pt foil - electrical contact
reference electrode: Ag thick film - 25 μm thick

Figure 11-6. Cell No. 3: Ag thick film reference electrode.

In Figure 11-7 the experimental results are presented for cell No. 3 as %Variance (in comparison to the theoretically calculated values) versus time for concentrations from 100 to 2400 ppm SO_2 in air. The data for this figure are listed in Appendix A, Table A-4. After approximately 100 hours of operation the cell voltage dropped to 5% below the theoretical voltage; at 132 hours the cell displayed a cell voltage 42% below the theoretical value.

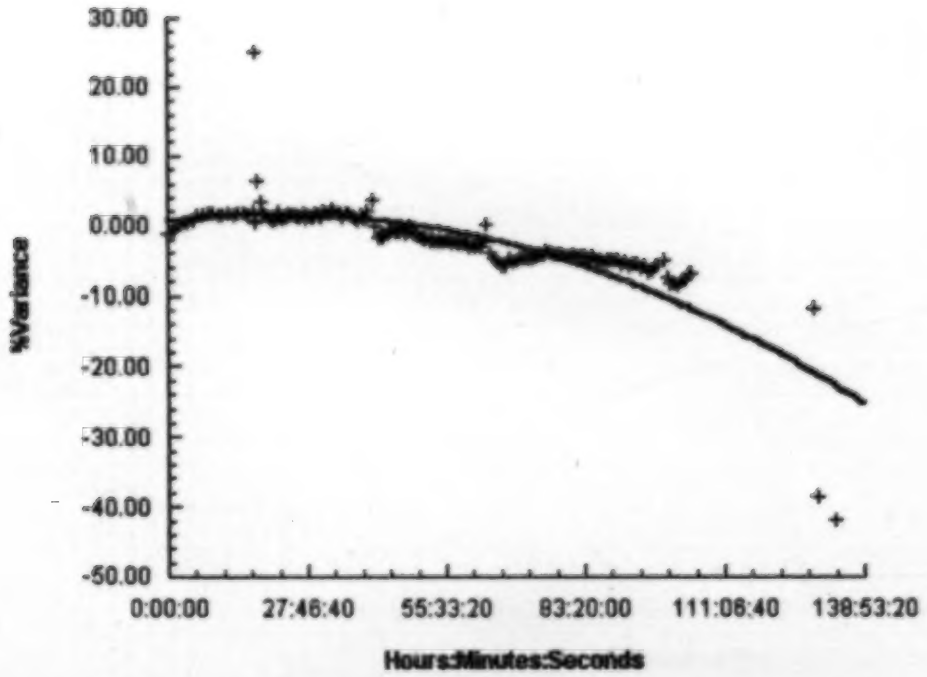

Figure 11-7. Cell No. 3: Ag thick film reference electrode - %Variance from theoretical values versus time for 100 to 2400 ppm SO_2 in air at 525 °C.

However, there was an extended period of time where the emf from the cell was relatively stable. Therefore, the results from this section of the experiment are plotted in Figure 11-8. The data for this graph are present in Appendix A, Table A-5.

The results from this run are:

$$Emf(V) = (0.1755 \pm 0.0044) + (0.0821 \pm 0.0014) log[SO_2 - ppm] \quad (100 - 2400\ ppm\ SO_2)\ R^2 = 0.9931 \tag{11.3}$$

from 100 to 2400 ppm SO_2 in air at 525 °C.
The theoretical cell equation at 525 °C (see Appendix D) is:

$$Emf(V) = (0.1963 \pm 0.0391) + (0.0792 \pm 0.0002) \log[SO_2 - ppm]$$

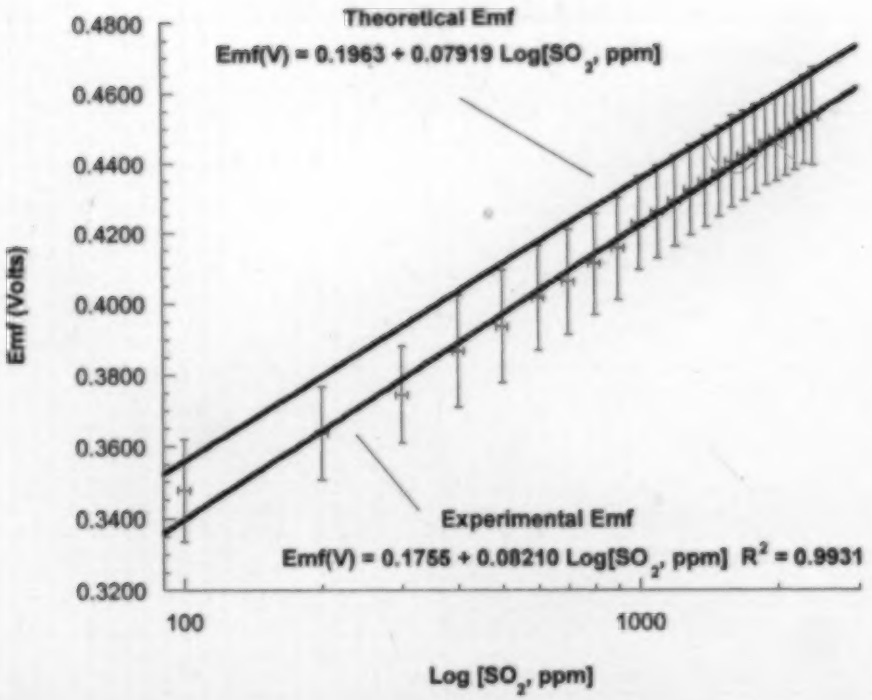

Figure 11-8. Cell No. 3: Ag thick film reference electrode - Emf versus log (SO_2 - ppm) from 100 to 2400 ppm SO_2 in air at 525 °C.

The experimental results for cell No. 3 fall outside the theoretical limits of error for the slope (0.07919 ±0.0002 V/decade) from between 0.07900 to 0.07940 V/decade which differs from theory by 3.7%. However, the experimental results are within the limits of error for the theoretical y-intercept (0.1963 ±0.0391 V) from between 0.1572 to 0.2354 V. The experimental Y-intercept varies from theory by 10.6%. A lower experimental value for the y-intercept is not unexpected since the cell emf had been observed to be declining over time.

Cell No. 4: Composite thick film reference electrode

This cell consists of a disc with a diameter of 25.4 mm constructed with the following layers:

- a working electrode consisting of a Pt thin film 0.1 μm (1000 Å) thick, deposited onto the solid electrolyte material, combined with an 80 mesh Pt gauze and Pt lead for connection to the external voltage measuring equipment
- a 2 mm thick layer of solid electrolyte consisting of 25 m/o Ag_2SO_4 – 75 m/o Li_2SO_4
- a reference electrode consisting of a 100 μm thick film layer fabricated with a 2:1 weight ratio mixture of Ag and 25 m/o Ag_2SO_4 – 75 m/o Li_2SO_4. In addition, a 1 μm (10,000Å) thick layer of Pt was deposited onto the reference electrode to ensure electrical contact
- a Pt foil pressed against the reference electrode which is connected to the external voltage measuring equipment via a Pt lead

The construction of this sensor is depicted in Figure 11-9.

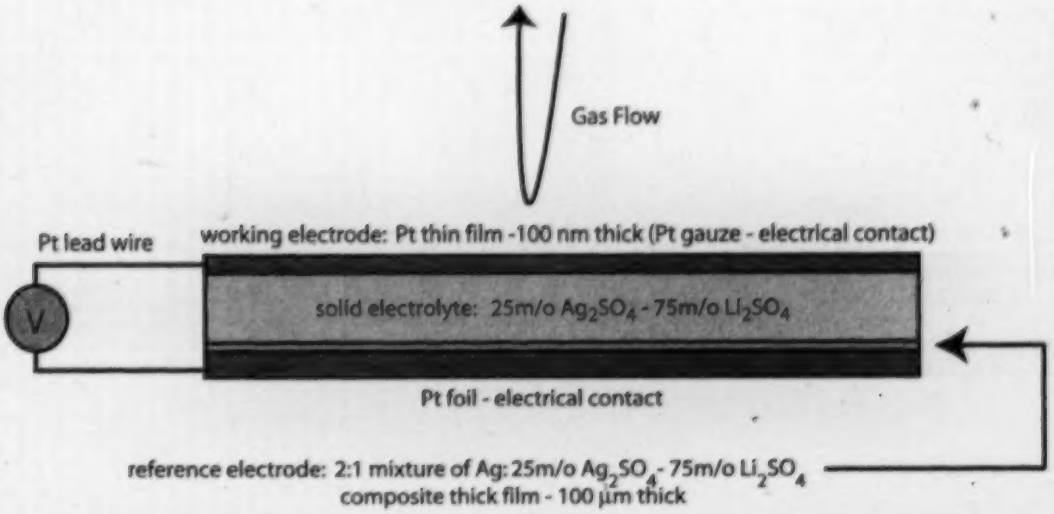
Gas Flow
Pt lead wire
working electrode: Pt thin film -100 nm thick (Pt gauze - electrical contact)
V
solid electrolyte: 25m/o Ag2SO4 - 75m/o Li2SO4
Pt foil - electrical contact
reference electrode: 2:1 mixture of Ag: 25m/o Ag2SO4 - 75m/o Li2SO4
composite thick film - 100 μm thick

Figure 11-9. Cell No. 4: Composite reference electrode thick film structure.

Experimental results: 100-2400 ppm SO_2

In Figure 11-10 the experimental results are shown for mixtures consisting of between 100-2400 ppm SO_2 in air at 535 °C. In Appendix A in Table A-6 the data for this graph are provided.

For the range of concentration between 100 and 2400 ppm SO_2 in air at 535 °C, the experimental equation was determined to be:

$$Emf(V) = (0.1658 \pm 0.0046) + (0.0824 \pm 0.0016)\log[SO_2 - ppm] \quad (100 - 2400\ ppm\ SO_2)\ \ R^2 = 0.9984 \tag{11.4}$$

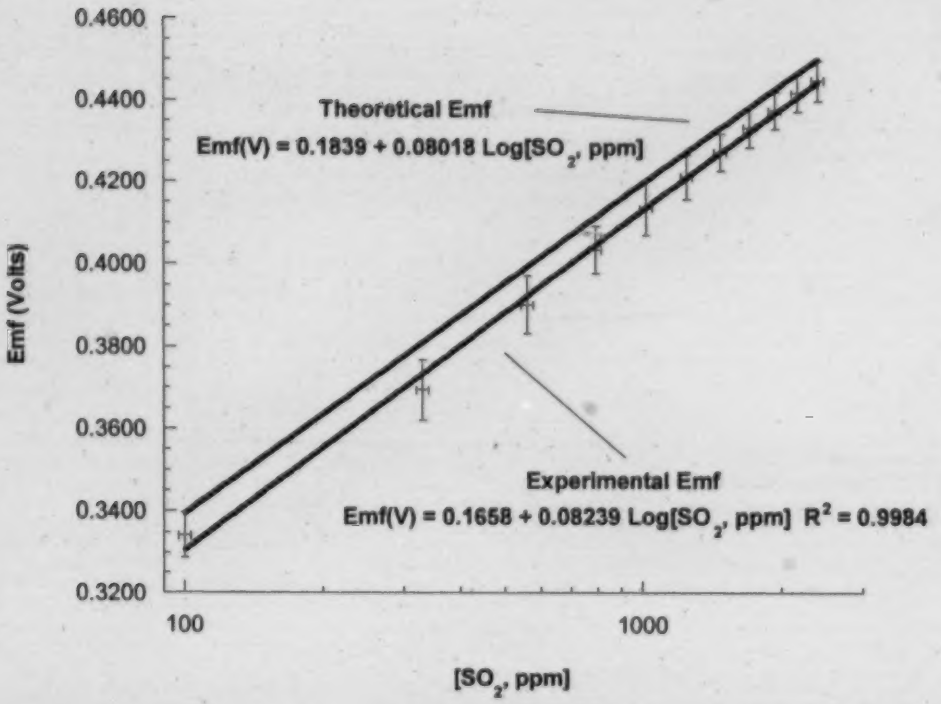

Figure 11-10. Cell No. 4: Composite thick film reference electrode - Emf (V) versus log (SO_2-ppm) for 100 to 2400 ppm SO_2 in air at 535 °C.

The experimentally determined value for the slope in this range of concentration is 0.0824 ± 0.0016 V/decade, i.e., the slope at 535 °C is within a range of between

0.0808-0.0840 V/decade. In comparison to the theoretically calculated value for the slope of 0.0802 ±0.0002 V/decade at 535°C, the experimental value differs by 2.7%.

The y-intercept is determined when the SO_2 = 1 ppm which is equal to log [SO_2-ppm] = 0 (see discussion in Appendix D, Figure D-1). According to the experimental data, the value for the y-intercept is equal to 0.1658 ± 0.0046 V (between 0.1612 – 0.1704 V) which is within the error limts of the theoretical theoretically calculated value for the y-intercept (0.1839 ±0.0391V) between 0.1479-0.2261. This is a difference from the theoretical y-intercept of 9.8%; however, this is not surprising given the size of the uncertainty in the free energy values for the cell reactions.

Experimental results: 10-496 ppm SO_2

In Figure 11-11 the experimental results for mixtures consisting of between 10 and 496 ppm SO_2 in air at 535 °C is presented. The data for this graph are provided in Appendix A, Table A-7.

The experimental equation from between 10 to 496 ppm SO_2 in air at 535 °C is:

$$Emf(V) = (0.1864 \pm 0.0027) + (0.0743 \pm 0.0012)\ \log[SO_2 - ppm] \quad (10 - 496\ ppm\ SO_2)\ R^2 = 0.9953 \qquad (11.5)$$

The experimentally determined slope in Figure 11-11, 0.0743 ± 0.0012 V/decade (i.e., a range of between 0.0731 and 0.0755 V/decade at 535 °C), in comparison to the theoretical value of 0.0802 ±0.0002 V/decade (i.e., a range of between 0.0800 to 0.0804 V/decade) differs by 7.4%. The experimental value for the y-axis intercept is 0.1864 ± 0.0019 V (i.e., a range of between 0.1845 to 0.1883V) which is a difference of only 1.4% compared to theory. However, it is apparent that in the lower ranges of concentration (<20 ppm) the sensor's performance is being affected as a rising tail in the experimental data is beginning to appear. For this reason in Figure 11-12 data from 59 ppm SO_2 and higher has been graphed separately.

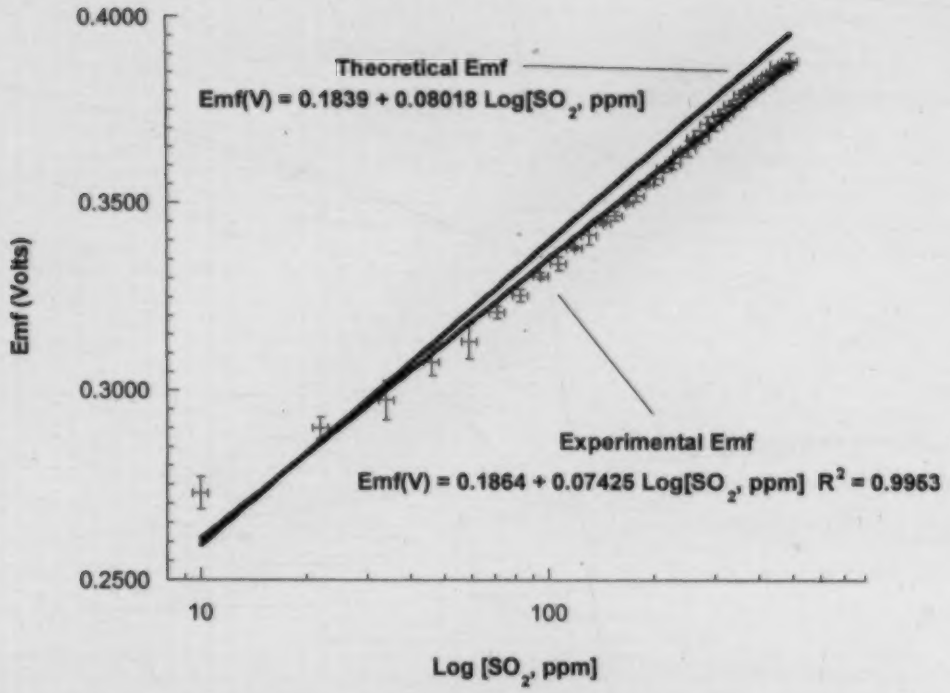

Figure 11-11. Cell No. 4: Composite thick film reference electrode -Emf (V) versus log (SO_2-ppm) for 10 to 496 ppm SO_2 in air at 535 °C.

The experimental equation for the range between 59 and 496 ppm SO_2 in air at 535 °C was determined to be:

$$Emf(V) = (0.1686 \pm 0.0027) + (0.0816 \pm 0.0012) \log[SO_2 - ppm] \quad (59 - 496\ ppm\ SO_2)\ R^2 = 0.9995 \tag{11.6}$$

In this situation the experimental slope is within 1.8% and the Y-intercept 8.3% of theory. However, the elimination of the tail at lower concentrations and an improved correlation coefficient of $R^2 = 0.9995$ more accurately represents cell performance.

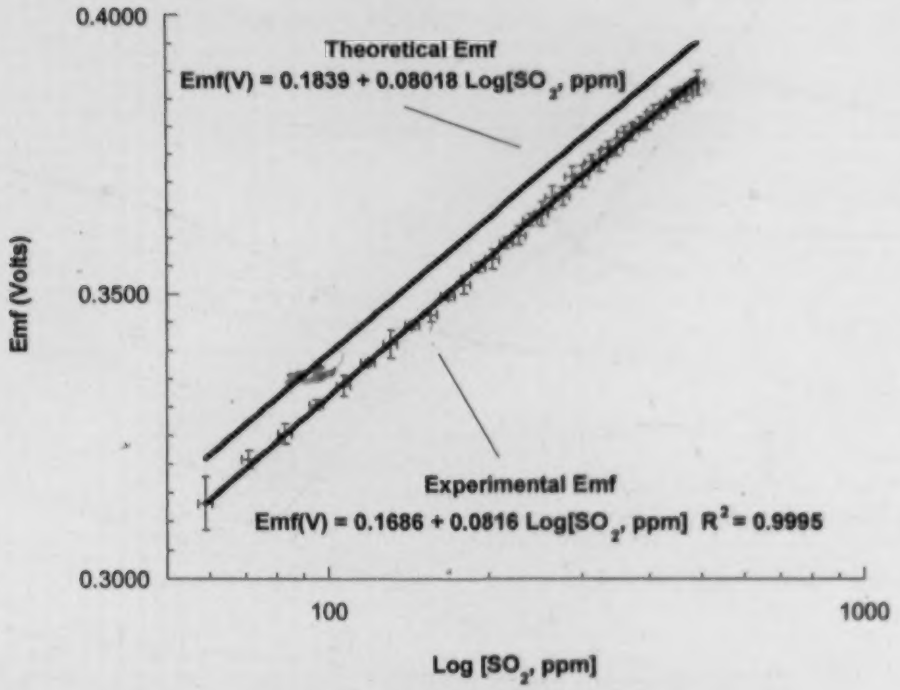

Figure 11-12. Cell No. 4: Composite thick film reference electrode – Emf (V) versus log (SO_2-ppm) for 59 to 496 ppm SO_2 in air at 535 °C.

Experimental results: 5.4-95.4 ppm SO_2

In Figure 11-13 the experimental results for mixtures consisting of between 5.4 and 95.4 ppm SO_2 in air at 535 °C are presented.

The data for this graph are provided in Appendix A, Table A-8. It is apparent in Figure 11-13 is that the experimentally determined slope does not follow a log-linear relationship due to a rising tail which develops in the experimental curve at concentrations below 20 ppm of SO_2 in air. Regardless, the best fit equation consists of a third order polynomial and was determined to be:

$$Emf(V) = 0.2613 + 0.00165[SO_2] - 1.425x10^{-5}[SO_2]^2 + 5.255x10^{-8}[SO_2]^3 \quad (5.4 - 95.4\ ppm\ SO_2) \qquad (11.7)$$

where the correlation coefficient R^2 = 0.9998 (however, a polynomial fit limits its relevance for this application).

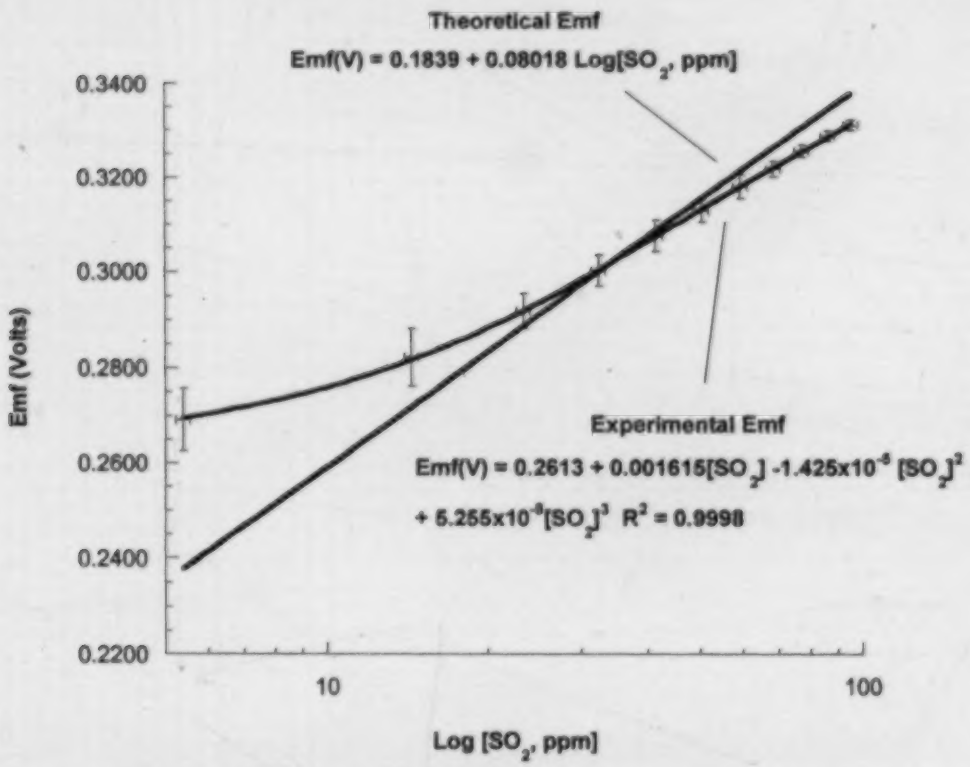

Figure. 11-13. Cell No. 4: Composite thick film reference electrode – Emf (V) versus log(SO_2-ppm) for 5.4 to 95.4 ppm SO_2 in air at 535 °C

Experimental results: 0.6-11.6 ppm SO_2

In Figure 11-14 the experimental results for mixtures consisting of between 0.6 and 11.6 ppm SO_2 in air at 535 °C are presented.

The data for this experimental run are located in Appendix A, Table A-9. The experimentally best fit equation was determined to be:

$$Emf(V) = 0.2460 + 0.00238[SO_2 - ppm] - 1.389x10^{-5}[SO_2 - ppm]^2 \quad (0.6 - 11.6\ ppm\ SO_2)\ R^2 = 0.9983 \tag{11.8}$$

It is apparent that, below concentrations of 10-20 ppm SO_2, the cell began to behave in a non-linear manner. At lower concentrations Nernstian behavior is lost and the cell becomes essentially unresponsive to changes in SO_2 concentration below about 5 ppm SO_2.

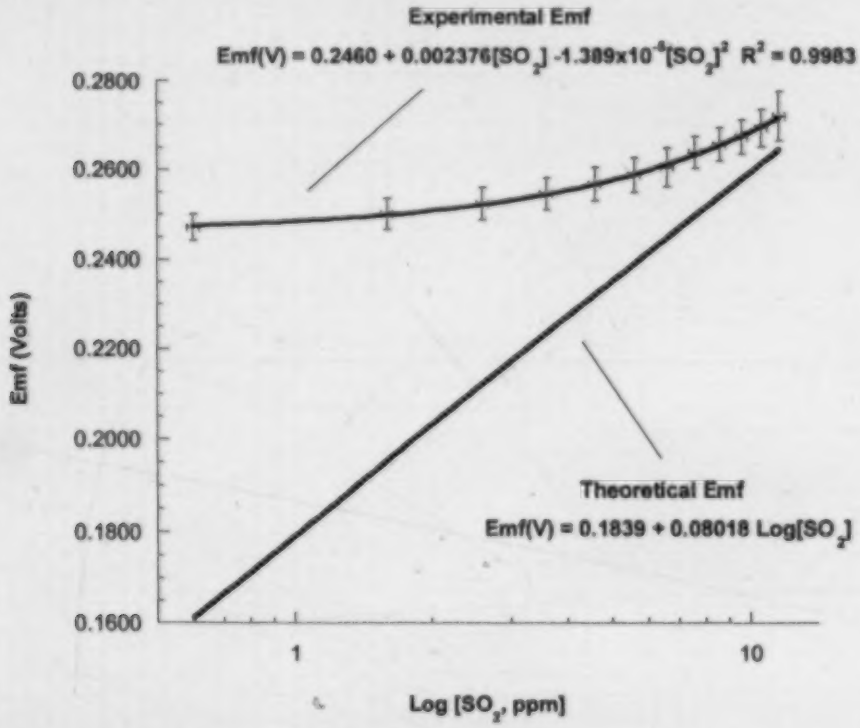

Figure 11-14. Cell No.4: Composite thick film reference electrode – Emf (V) versus log(SO_2-ppm) for 0.6 to 11.6 ppm SO_2 in air at 535 °C.

Experimental results: 14.4-2400 ppm SO_2

In Figure 11-15 cumulative experimental results for mixtures consisting of between 14.4 and 2400 ppm SO_2 in air at 535 °C are provided. The data for this graph are located in Appendix A, Table A-10.

The experimental equation for the range between 14.4-2400 ppm SO_2 in air at 535 °C was determined to be:

$$Emf(V) = (0.1810 \pm 0.0010) + (0.07686 \pm 0.0005)\log[SO_2 - ppm] \quad (14.4 - 2400\, ppm\ SO_2)\ R^2 = 0.9975 \tag{11.9}$$

The experimentally determined slope in Figure 11-15, is 0.07686 ± 0.0005 V/decade (i.e., a range of between 0.0764 and 0.0774 V/decade at 535 °C). In comparison to the theoretical value for the slope (0.08018 ±0.0002 V/decade, i.e., a range of between 0.0800 to 0.0804 V/decade) the experimental value differs by 4.1% from theory. However, it is again apparent that in the lower ranges of concentration (<20 ppm) a tail in the experimental data is beginning to appear which is skewing the experimental slope.

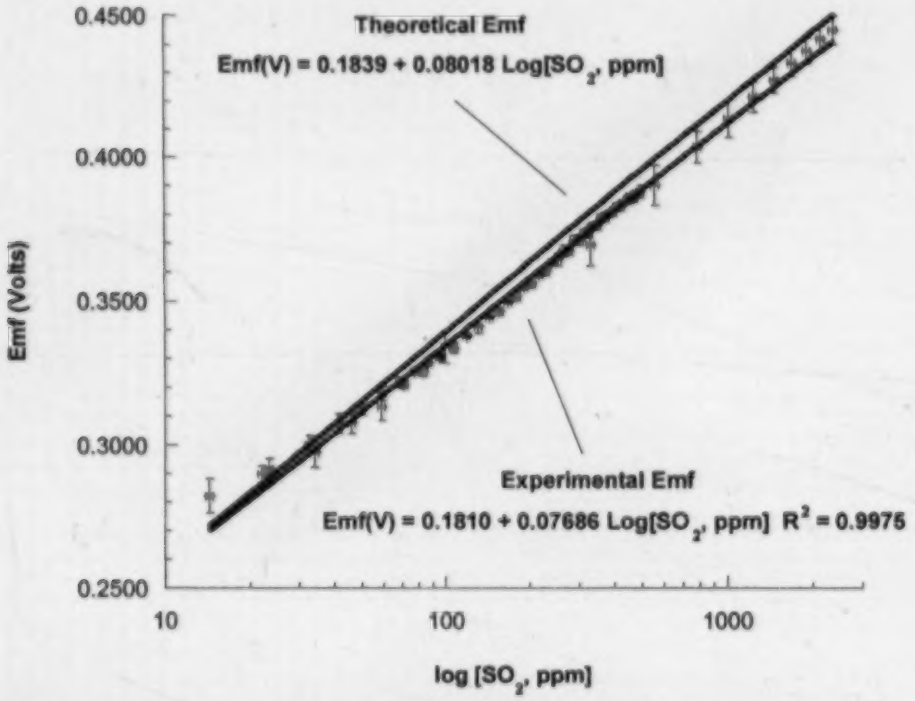

Figure 11-15. Cell No. 4: Composite thick film reference electrode – Emf (V) versus log (SO_2-ppm) for 14.4 to 2400 ppm SO_2 in air at 535 °C.

In addition, the experimental value for the y-axis intercept is 0.1810 ± 0.0010 V (i.e., a range of between 0.1800 to 0.1820 V) which varies from theoretical Y-intercept by only 2.9 mV or 1.6%. Again it is observed in Figure 11-15 that the sensor performance at lower concentration levels is affecting the value of the y-intercept.

In Figure 11-16 the data is plotted with exclusion of values below 50 ppm. The experimental curve fit in comparison to the theoretical equation is such that the y-intercept is within 11.6 mV or 6.3% of theory. At the same time the experimental slope is virtually the same value as the theoretical value. This precisely confirms the Nernstian response of the cell and the predominance of ionic conductivity within the solid electrolyte.

The experimental equation for the range between 50-2400 ppm SO_2 in air at 535 °C was determined to be:

$$Emf(V) = (0.1723 \pm 0.0010) + (0.0802 \pm 0.0005)\log[SO_2 - ppm] \quad (50 - 2400\,ppm\ SO_2)\ R^2 = 0.9982 \tag{11.10}$$

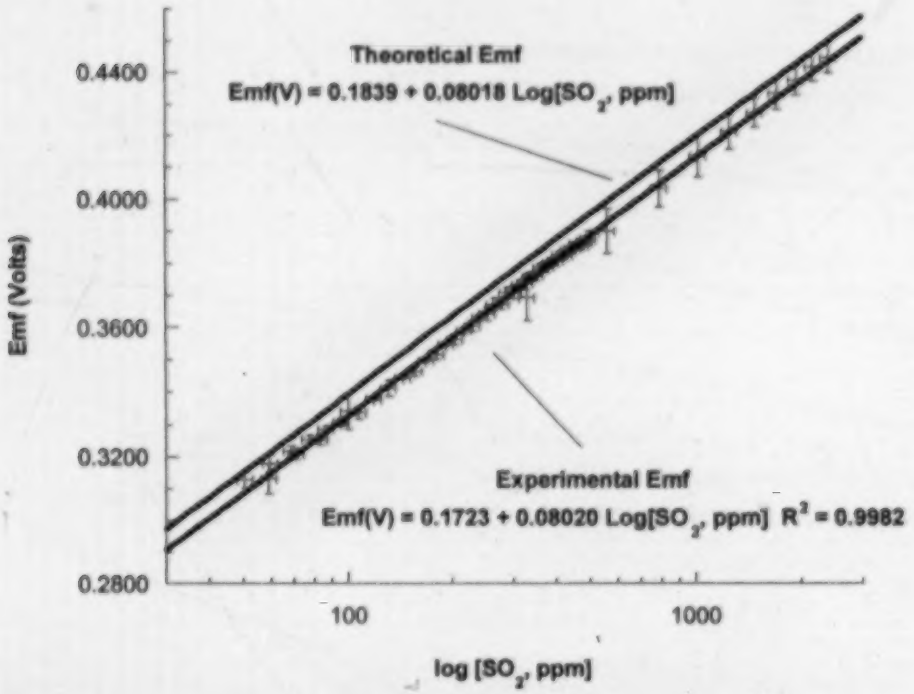

Figure 11-16. Cell No. 4: Composite thick film reference electrode – Emf (V) versus log (SO_2-ppm) for 50 to 2400 ppm in SO_2 in air at 535 °C.

Cell No. 4: Flow rate dependence

An often under-appreciated phenomenon associated with gas sensors is flow rate dependence. Therefore, utilizing cell No. 4 a series of flow rate tests were performed with mixtures consisting of 200, 50 and 5 ppm SO_2 in air at 535 °C. The error bars in these graphs are due to the error in measurement of emf and ±1% of full scale flow rate for the electronic mass flow controllers (i.e., ±2 sccm).

As is apparent in Figure 11-17 for 200 ppm SO_2, a minimum flow rate is necessary to realize flow rate independence, i.e. ± 0.7 mV from 25-60 sccm. The data for this graph are located in Appendix A, Table A-11.

For a mixture consisting of 50 ppm SO_2 in air, Figure 11-18 displays a larger variance in the emf, i.e., ± 1.2 mV from 25-55 sccm. It is also apparent that the size of the standard deviation of the measurements for each flow rate has increased. From an analysis of the data located in Appendix A, Table A-12 it is observed that the standard deviation varies from 0.0080 V (8 mV) at 5 sccm to an average of approx. 0.002 V (2 mV) at other flow rates.

The final mixture tested consisted of 5 ppm SO_2 in air, as presented in Figure 11-19. These results display an even narrower range of flow independence, i.e., ± 1.5 mV from 25-55 sccm. However, examination of run data in Table A-13 indicates a reduced standard deviation in the measurements.

Inaccuracy at low flow rates can be attributed either to electronic conduction in the electrolyte resulting in concentration polarization at the working electrode or thermal diffusion in the gas mixture. Flushing problems upon varying the SO_2 concentration that are highly dependent on cell configuration can also contribute. Optimizing the gas flow becomes more critical for gas mixtures dilute in the electro-active component. This was observed in mixtures consisting of 5 ppm SO_2 as displayed in

Figure 11-19. As the flow rate increases beyond the optimal level, cooling of the working electrode results in a decline in measured cell voltage.

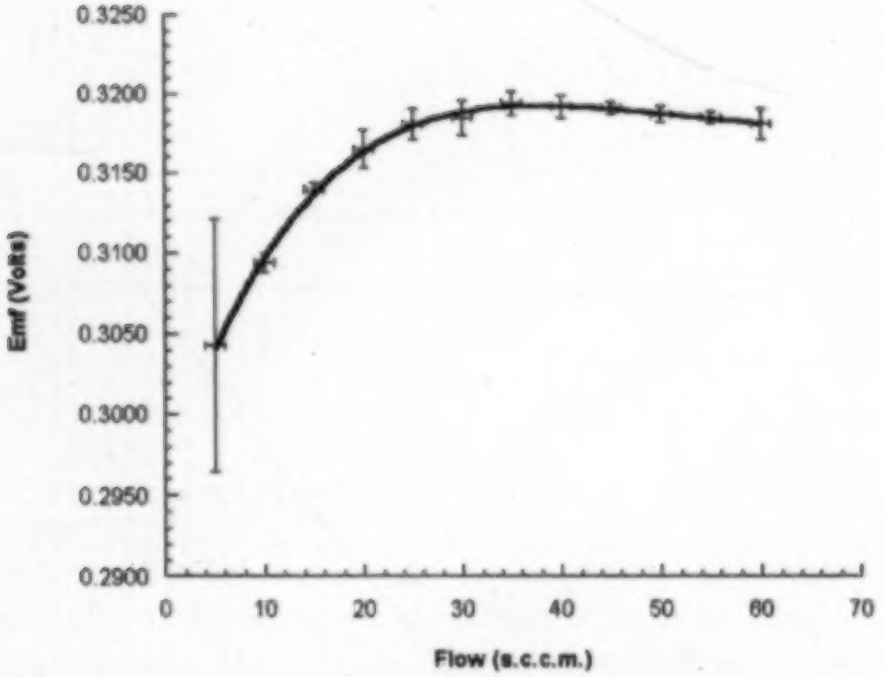

Figure 11-17. Flow rate dependence utilizing 200 ppm SO_2 in air at 535 °C.

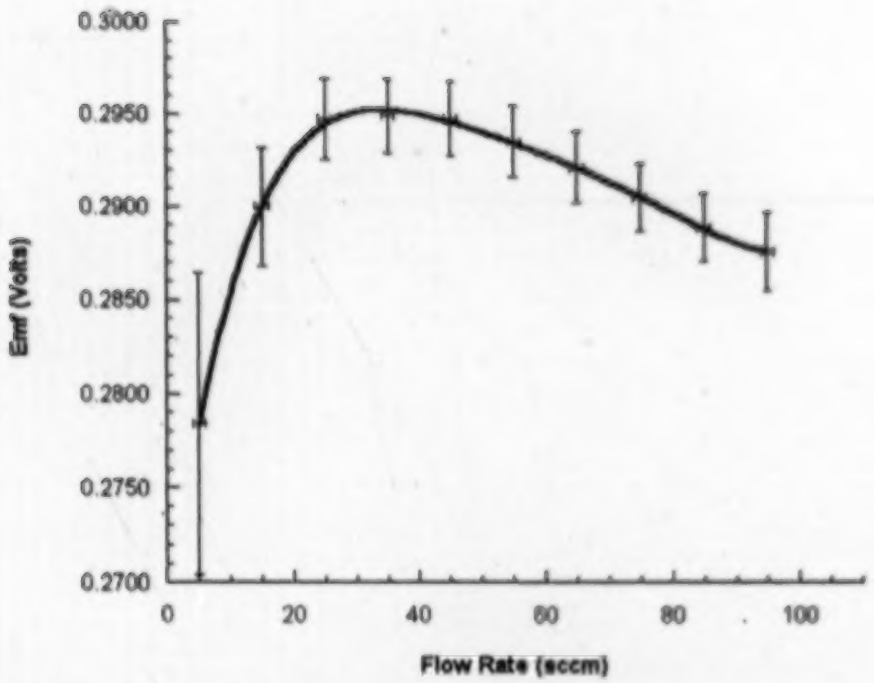

Figure 11-18. Flow rate dependence utilizing 50 ppm SO_2 in air at 535 °C.

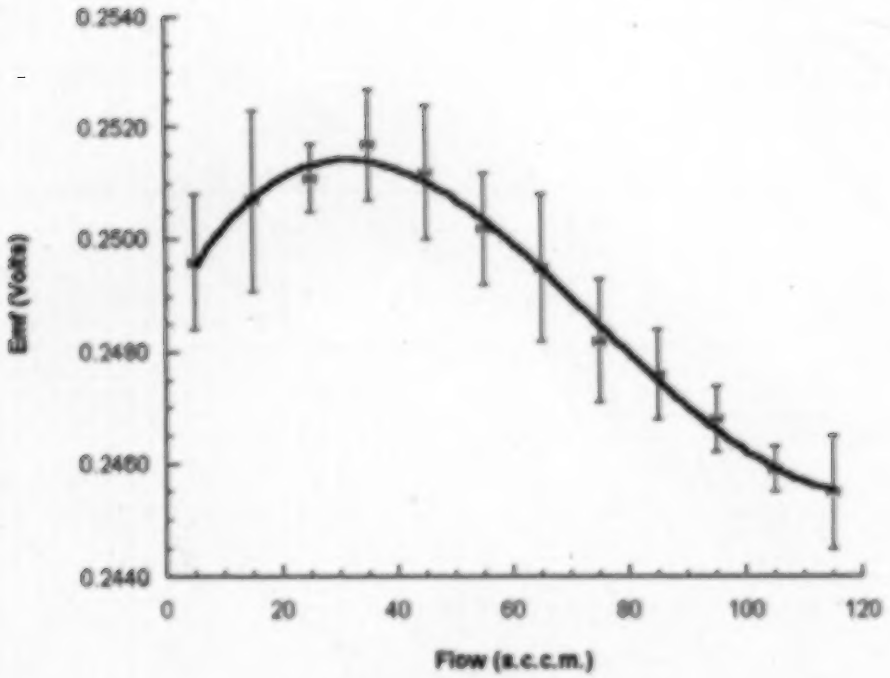

Figure 11-19. Flow rate dependence utilizing 5 ppm SO_2 in air at 535 °C.

Cell No. 5: Thick film electrolyte

This cell consists of a disc with a diameter of 25.4 mm constructed with the following layers:

- the working electrode consisted of a Pt thin film 0.1 μm (1000 Å) thick, deposited via evaporation onto the solid electrolyte material combined with an 80 mesh Pt gauze and Pt lead for connection to the external voltage measuring equipment
- the solid electrolyte layer consists of a 200 μm thick bi-layer of 25 m/o Ag_2SO_4 – 75 m/o Li_2SO_4 fabricated through thick film deposition of two 100 μm thick layers
- the reference electrode consists of 2:1 weight ratio mixture of Ag and 25 m/o Ag_2SO_4 – 75 m/o Li_2SO_4, 3 mm thick, fabricated via pressing and sintering in an atmosphere containing 500 ppm SO_2.
- a Pt foil containing the reference electrode which is connected to the external voltage measuring equipment via a Pt lead

This cell design is illustrated in Figure 11-20.

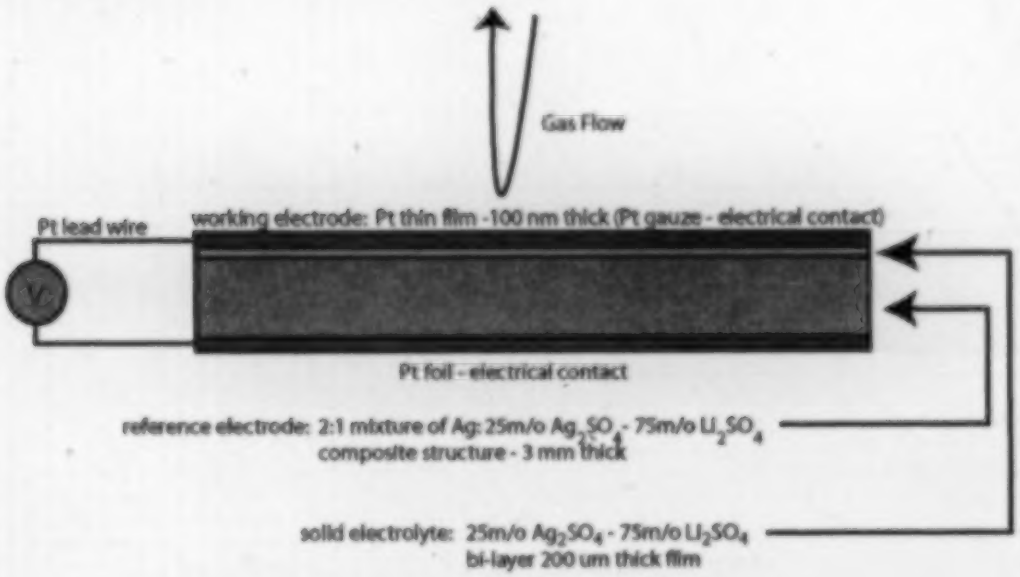
Gas Flow
Pt lead wire
working electrode: Pt thin film -100 nm thick (Pt gauze - electrical contact)
V
Pt foil - electrical contact
reference electrode: 2:1 mixture of Ag: 25m/o Ag2SO4 - 75m/o Li2SO4
composite structure - 3 mm thick
solid electrolyte: 25m/o Ag2SO4 - 75m/o Li2SO4
bi-layer 200 um thick film

Figure 11-20. Cell No. 5 Thick film solid electrolyte

In Figure 11-21 the results for Cell No. 5 from 71-947 ppm SO_2 in air at 535 °C are provided. The data for this run are located in Appendix A, Table A-14. In the fabrication of the solid electrolyte layer, two separate depositions were applied so as to reduce the effect of porosity. This is similar to multiple depositions of inter-layer dielectrics in micro-chip fabrication. However, the results show that the thick film solid electrolyte was essentially non-functional. From visual observations of the electrolyte it was apparent that porosity and cracking in the electrolyte film was the reason for failure.

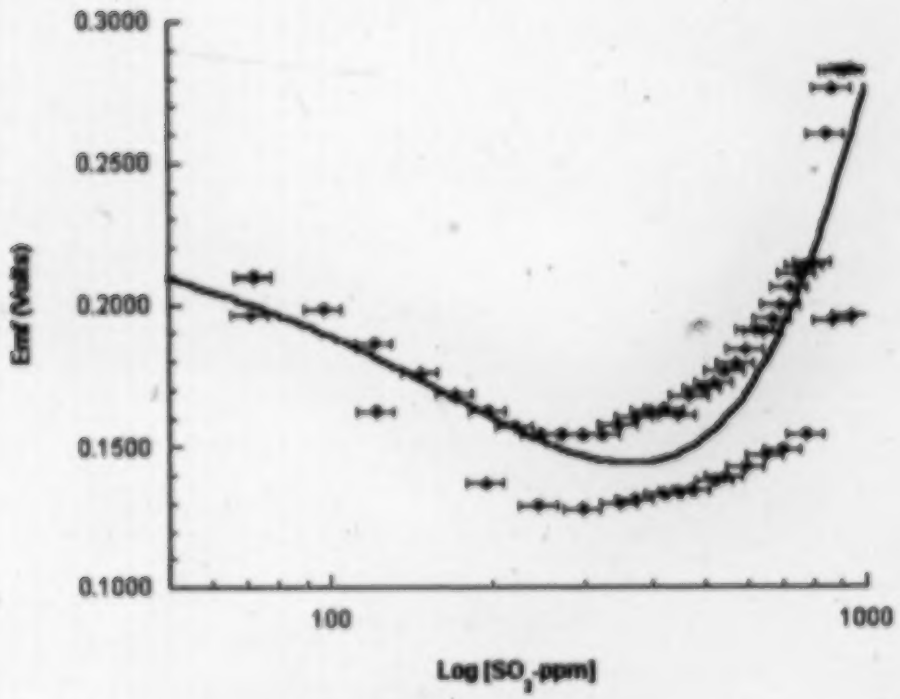

Figure 11-21. Thick film solid electrolyte

Summary of Results

In Tables 11-1 to 11-3 a summary of the experimental results achieved is given. It is apparent that at concentrations higher than 10 ppm, Cell No. 4 measures the concentration accurately to levels as high as 2400 ppm. The results for Cell No. 4 compare favourably (in some cases within 1-2% of theory) with the theoretically determined cell equation as derived in Appendix D.

The optimal flow rate for this cell design was found to be between 30 and 40 sccm as displayed in Figures 11-17 to 11-19 for concentrations below 200 ppm SO_2. Clearly, flow rate and its optimization are critical at SO_2 concentrations below 10 ppm (see Figure 11-19). If it is assumed that an accurate emf value is obtained at the plateau displayed in Figure 11-17 for 200 ppm SO_2, flow rate independence can be considered to be realized above 30 to 40 sccm. However, there will be cooling of the cell at higher flow rates and therefore a drop in cell emf at higher flow rates. Regardless, below a gas concentration of 200 ppm SO_2 the optimum cell voltage output is dependent on flow rate between 30 to 40 sccm.

Electrode kinetics at the working electrode, especially at the lower SO_2 concentrations, could also limit sensor accuracy. It would be useful in this case to determine the exchange current densities of the both the working and reference electrodes in relation to temperature, gas concentration and electrode structure. Regardless, excluding the difficulty with measurement of low SO_2 concentrations, the sensor performed reliably for over four months. The cumulative results plotted in Figure 11-15 between 14.4 and 2400 ppm and in Figure 11-16 between 50 and 2400 ppm SO_2 in air are indicative of the achievable performance.

The thin film working electrode provides a large density of triple phase boundary (T.P.B.) points, at least an order or more of magnitude than a typical Pt wire gauze. This combined with a high level of ionic conductivity in the electrolyte results in a fast response time. However, since the sensor was loaded into a relatively large

cylindrical ceramic chamber, precise determination of response times to changes in gas concentration was not possible. Regardless, it was observed that the sensor's initial response to changes in gas concentration occurred within 20-30 seconds. This would be primarily due to the time required for the altered gas concentration to reach the sensor. The remainder of the response time was more a function of the purging of the test chamber than the kinetics of the sensor response. It also appears that the Pt containing quartz chamber was effective in converting SO_2 to SO_3 due to the linearity of the results over a large range of concentration up to 2400 ppm SO_2. For future experimentation it is highly recommended that a small gas chamber be utilized for precise determination of the sensor response time. To further enhance the kinetics at the working electrode, it would be advantageous to develop a mixed ionic-electronic electrode consisting of a Pt-sulfate electrolyte mixture with controlled micro-porosity.

The composite reference electrode (consisting of a 2:1 weight ratio mixture of $Ag:Ag_2SO_4$-Li_2SO_4) resulted in the Ag_2SO_4 chemical potential being the same in both the electrolyte and the reference electrode. In this situation there should be no chemical interaction between the reference electrode and two-phase electrolyte. Therefore, over time the Ag_2SO_4 activity should remain constant and the cell output voltage will not change or degrade. In cell No. 4 over the test period a high level of stability was observed with concentrations being continuously cycled from high to low levels.

Table 11-1. Summary of experimental results for Cell No. 1 - Composite reference electrode

Range of $[SO_2]$	Equation: Emf(Volts) versus log(ppm SO_2) at 535 °C	Correlation Coefficient
Theoretical ($[SO_2]>0$)	Emf(V)= (0.1839 ±0.0391) + (0.08018 ±0.0002) log[ppm SO_2]	$R^2 = 1$
$[SO_2]$ = 94-900 ppm	Emf(V)= (0.2176 ±0.0043) + (0.0725 ±0.0016) log[ppm SO_2]	$R^2 = 0.9847$

Table 11-2. Summary of experimental results for Cell No. 3 - Thick film reference

Range (ppm SO_2)	Equation: Emf(Volts) versus log(ppm SO_2) at 525 °C	Correlation Coefficient
Theoretical ($[SO_2]>0$)	Emf(V)= (0.1963 ±0.0391) + (0.07919 ±0.0002) log[ppm SO_2]	$R^2 = 1$
$[SO_2]$ = 100-2400	Emf(V)= (0.1755 ±0.0044) + (0.0821 ±0.0014) log[ppm SO_2]	$R^2 = 0.9931$

Table 11-3. Summary of experimental results for Cell No. 4 - Thick film reference

Range (ppm SO_2)	Equation: Emf(Volts) versus log(ppm SO_2) at 535 °C	Correlation Coefficient
Theoretical ($[SO_2]>0$)	Emf(V)= (0.1839 ±0.0391) + (0.08018 ±0.0002) log[SO_2-ppm]	$R^2 = 1$
$[SO_2]$ = 100-2400	Emf(V)= (0.1658 ±0.0046) + (0.0824 ±0.0016) log[SO_2-ppm]	$R^2 = 0.9984$
$[SO_2]$ = 10-496	Emf(V)= (0.1864 ±0.0027) + (0.0743 ±0.0012) log[SO_2-ppm]	$R^2 = 0.9953$
$[SO_2]$ = 59-496	Emf(V)= (0.1686 ±0.0027) + (0.0816 ±0.0012) log[SO_2-ppm]	$R^2 = 0.9995$
$[SO_2]$ = 5.4-95.4	Emf(V)= 0.2613 + 0.00162 [SO_2-ppm] -1.425x10^{-5}[SO_2-ppm]^2 + 5.255x10^{-8}[SO_2]^3	$R^2 = 0.9998$
$[SO_2]$ = 0.6-11.6	Emf(V)= 0.2460 + 0.00238[SO_2-ppm] –1.389x10^{-5} [SO_2-ppm]^2	$R^2 = 0.9983$
$[SO_2]$ = 14.4-2400	Emf(V)= (0.1810 ±0.0010) + (0.0769 ±0.0005) log[SO_2-ppm]	$R^2 = 0.9975$
$[SO_2]$ = 50-2400	Emf(V)= (0.1723 ±0.0010) + (0.0802 ±0.0005) log[SO_2-ppm]	$R^2 = 0.9982$

Calculation of Ag_2SO_4 Activity

According to the Ag_2SO_4-Li_2SO_4 phase diagram, the two phase region (between 20-35 mole % Ag_2SO_4) in which this sensor operates consists of the two phases: αLi_2SO_4ss and $(Ag,Li)_2SO_4$ss. As indicated previously, the activity of Ag_2SO_4 does not depend on its concentration in this two phase region. However, the activity of Ag_2SO_4 is related to its composition as defined by the phase, $(Ag,Li)_2SO_4$ss.

To calculate the activity for Ag_2SO_4 and the associated error in the experimental results, data from the experimental run (cell No. 4) between 14.4-2400 ppm in SO_2 were utilized. Mixing of gases was performed with two electronic mass flow controllers (M.F.C.s) calibrated to the following specifications:

SO_2 flow rate = ±1% of full range of 50 sccm or ±0.5 sccm
Air flow rate = ±1% of full range of 100 sccm or ±1 sccm
SO_2 concentration = certified at ±1% of stated cylinder concentration or ±24 ppm

Therefore, the accuracy in the gas mixtures produced is ±5% of the mixtures concentration. For example, a 900 ppm SO_2 mixture would have an error of ±45 ppm SO_2.

Utilizing equation 8.4, the value of the activity for Ag_2SO_4 was calculated for concentrations between 100 and 2400 ppm SO_2 in air for Cell No. 4 with the values listed in Table 11-4. Propagation of the uncertainty with these calculations is outlined in Appendix E. From these calculations the average value for the experimental activity of Ag_2SO_4, $\bar{a}_{Ag_2SO_4}$, was determined to be:

$$\bar{a}_{Ag_2SO_4} = 0.2986 \pm 0.0265$$

The value for the activity of Ag_2SO_4 (23 m/o Ag_2SO_4 – 77 m/o Li_2SO_4) equals 0.25 at 530 °C according to the literature [40, 89]; however, this work indicates an experimentally determined activity of 0.2986 ±0.0265, at 535 °C, which is higher by 19.4%. This is a reasonable value for the activity given that the cell is operated at 535 °C and the material consists of 25 m/o Ag_2SO_4 – 75 m/o Li_2SO_4.

During preparation of the solid electrolyte for this cell, there was hydration of Li_2SO_4 resulting in the formation of $Li_2SO_4 \cdot H_2O$. Evidence of this hydration is the presence of both Li_2SO_4 and $Li_2SO_4 \cdot H_2O$ in the X-ray diffraction patterns of the material prior to formation of the solid electrolyte disc (see Figure 11-29). However, since the diffraction pattern displays the presence of peaks for both Li_2SO_4 and $Li_2SO_4 \cdot H_2O$, the conversion to the hydrated form was not entirely complete. The exact composition is not known. Regardless, the attached water would subsequently have been driven off during operation of the cell at 535 °C leaving behind anhydrous Li_2SO_4. For the case where the Li_2SO_4 is completely hydrated initially to $Li_2SO_4 \cdot H_2O$ at the time of weighing, the adjusted mole fraction of Ag_2SO_4 at an operating temperature of 535 °C would be equal to 0.2796 (see Appendix F). Therefore, in any event the solid electrolyte utilized in this work falls within the two phase region between 20 and 35 mole percent Ag_2SO_4. Therefore, the activity of Ag_2SO_4 is defined by the chemical composition of the $(Ag, Li)_2SO_4$ phase and not the molar fraction of Ag_2SO_4. Also, it is recommended that in future work for improved accuracy, the Li_2SO_4 is weighed in an atmosphere absent of water vapour.

Table 11-4. Average experimental activity, $a_{Ag_2SO_4}$, for cell No. 4 – Thick film reference, 14.4 to 2400 ppm SO_2 at 535 °C.

$SO_{2(in)}$ ppm	$SO_{3(in)}$ ppm	$Emf_{measured}$(Volts)	Activity	Activity Error
22	18.7	0.2901	0.2267	0.0204
23.4	19.9	0.2919	0.2289	0.0204
32.4	27.6	0.3003	0.2491	0.0222
34	28.9	0.2975	0.2832	0.0257
41.4	35.2	0.3075	0.2588	0.0231
46	39.2	0.3077	0.2859	0.0258
50.4	42.9	0.3128	0.2706	0.0241
59	50.2	0.3132	0.3131	0.0279
59.4	50.6	0.3180	0.2746	0.0245
68.4	58.2	0.3217	0.2844	0.0253
71	60.4	0.3209	0.3020	0.0268
77.4	65.9	0.3255	0.2885	0.0257
83	70.7	0.3254	0.3103	0.0276
86.4	73.5	0.3287	0.2938	0.0262
95	80.9	0.3305	0.3068	0.0273

95.4	81.2	0.3310	0.3037	0.0270
100	85.1	0.3342	0.2904	0.0261
107	91.1	0.3338	0.3143	0.0280
119	101.3	0.3379	0.3107	0.0278
131	111.5	0.3412	0.3111	0.0278
144	122.6	0.3445	0.3110	0.0276
156	132.8	0.3464	0.3191	0.0284
168	143.0	0.3497	0.3125	0.0278
180	153.2	0.3517	0.3162	0.0281
192	163.4	0.3548	0.3085	0.0275
204	173.7	0.3563	0.3140	0.0280
217	184.7	0.3591	0.3082	0.0274
229	194.9	0.3604	0.3133	0.0278
241	205.2	0.3632	0.3043	0.0271
253	215.4	0.3643	0.3095	0.0276
265	225.6	0.3672	0.2983	0.0266
277	235.8	0.3674	0.3100	0.0276
289	246.0	0.3709	0.2925	0.0261
302	257.1	0.3710	0.3048	0.0271
314	267.3	0.3734	0.2958	0.0263
326	277.5	0.3738	0.3036	0.0270
330	280.9	0.3694	0.3487	0.0316
338	287.7	0.3759	0.2963	0.0264
350	297.9	0.3762	0.3042	0.0271
362	308.2	0.3788	0.2920	0.0260
374	318.4	0.3790	0.2999	0.0267
387	329.4	0.3803	0.2990	0.0266
399	339.7	0.3810	0.3021	0.0269
411	349.9	0.3826	0.2972	0.0264
423	360.1	0.3826	0.3059	0.0272
435	370.3	0.3841	0.3013	0.0268
447	380.5	0.3848	0.3035	0.0270
460	391.6	0.3861	0.3009	0.0268
472	401.8	0.3856	0.3132	0.0279
484	412.0	0.3871	0.3076	0.0274
496	422.2	0.3878	0.3090	0.0276
560	476.7	0.3901	0.3265	0.0295
790	672.5	0.4035	0.3135	0.0282
1020	868.3	0.4136	0.3028	0.0273
1250	1064.1	0.4212	0.2984	0.0268
1480	1259.9	0.4272	0.2973	0.0267
1710	1455.7	0.4333	0.2883	0.0259
1940	1651.4	0.4375	0.2900	0.0260
2170	1847.2	0.4417	0.2875	0.0257

2400	2136.0	0.4448	0.3041	0.0261
		STDEV =	**0.0201**	**0.0022**
		Average =	**0.2986**	**0.0265**

Micrographs and Chemical Analysis of Electrodes

A scanning electron microscope (SEM), Cambridge Instruments Stereoscan Model 250, was used to produce micro-photographs of the working and reference electrodes. As can be seen in Figure 11-22 for Cell No. 4, the surface of the solid electrolyte (25m/o Ag_2SO_4–75m/o Li_2SO_4) at 72X appears with a coating of a porous thin film layer of Pt. In Figures 11-23 and 11-24 at higher magnification reveals the actual structure of the Pt thin film on the solid electrolyte. The working electrode displays islands of Pt which provide a tremendous number of triple phase boundary (T.P.B.) points, consisting of solid electrolyte-electrical conductor-gas phase interaction sites. From measurements derived from Figure 11-24, it has been estimated that the length of the T.P.B. sites is equal to ~85 μm from within an area of 350 μm^2. It follows that the T.P.B.:area ratio is equal to 0.24 $\mu m/\mu m^2$. In comparison, 80 mesh Pt gauze would have a T.P.B.:area ratio of 0.020 $\mu m/\mu m^2$. Also, contact of the Pt to the electrolyte is assured with thin film deposition; in contrast this will not always be the case for wire mesh in contact with an electrolyte surface. Since the Pt thin film provides an increase in the T.P.B. sites, this would explain the quick sensor response observed during testing to changes in gas concentration–implying rapid kinetics for the working electrode reaction (i.e., $SO_2 + \frac{1}{2}O_2 + 2e^- \rightarrow SO_4^{2-}$). In conclusion, a working electrode consisting of a Pt thin film and gauze has been shown to result in a favourable structure for the catalysis and conversion of SO_3 to SO_4^{2-} into the electrolyte.

Typically, in the deposition of thin films, the parameters required for stress-free films fall within a narrow region of pressure, deposition rate, substrate temperature and surface roughness. In the deposition of a porous thin film layer, strict control of depositional parameters is not required. Therefore, fabrication of the platinum thin

film with the required properties is relatively easy to achieve. There are also various combinations of deposition techniques and patterning methods that could be employed to increase the length of the T.P.B. sites even more.

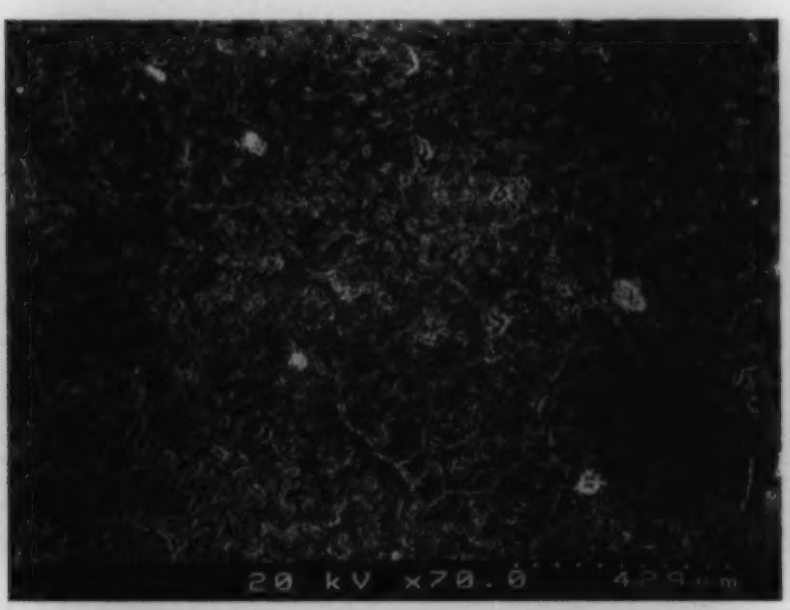

Figure 11-22. Photograph of the working electrode consisting of a platinum thin film 1000 Å thick deposited on the solid electrolyte substrate – 72X.

Along with the micrographs, the SEM system also has the capability of analyzing the chemical composition of the thin film via energy dispersive x-ray (EDX) analysis. In this technique an electron beam strikes the surface of a conducting sample with a beam energy typically in the range of 10-20 keV. The energy of the x-rays emitted (keV) depends on the material being analyzed, of which several signal peak counts are produced during data acquisition. EDX analysis typically results in a spectrum with various elements superimposed on each other. Utilizing computer analysis software, the individual elements were determined from the spectrum pattern. The interaction of the electron beam occurs within a volume of about two microns in depth; therefore, EDX is not a surface science technique. Elements of low atomic

number are also difficult to detect. In EDX analysis a lithium doped silicon detector is often protected by a beryllium window. The severe attenuation of the soft x-rays by a Be window precludes the detection of elements below an atomic number of 11 (Na). In windowless systems, elements with as low an atomic number as 4 (Be) can be detected. Regardless, with the lighter elements it is difficult to get a strong enough x-ray signal to ensure a high signal to noise ratio and an accurate analysis. Operation in windowless mode also limits the life of the Si-Li detector. This is due to the fact that the detector being chilled with liquid nitrogen will condense contaminants present in the vacuum chamber resulting in detector degradation.

In the EDX analysis presented in Figures 11-25 and 11-26 a beryllium window was utilized; therefore, it would be expected that Pt, Ag and S would be observed with Li and O being excluded from the analysis. This was observed with peaks for Pt and S present in the analysis and peaks for Li and O absent as expected. Any variation in the heights of Pt and Ag peaks between the two EDX analyses of the working electrode are probably due to spatial effects and placement of the analyzing beam. The two phase nature of the electrolyte, i.e., both Li_2SO_4 and Ag_2SO_4 phases are present, and the irregular deposition of the Pt film must also be taken into consideration. Since the energy of the x-rays was 20 keV, the measured signal count was high enough to ensure a good signal to noise ratio. A 20 keV beam thoroughly penetrates the 1000 Å and 10,000 Å films and includes analysis of the underlying solid electrolyte. EDX is a semi-quantitative technique at best with accurate analysis requiring calibration of the EDX analysis system using standards of known composition and thin specimens; for some combinations of elements, large differences in the self-absorption and fluorescence of emitted x-rays will limit the precision of quantitative analysis. The EDX spectra provided are for verification of the expected elements and to detect contamination in the thin film or solid electrolyte.

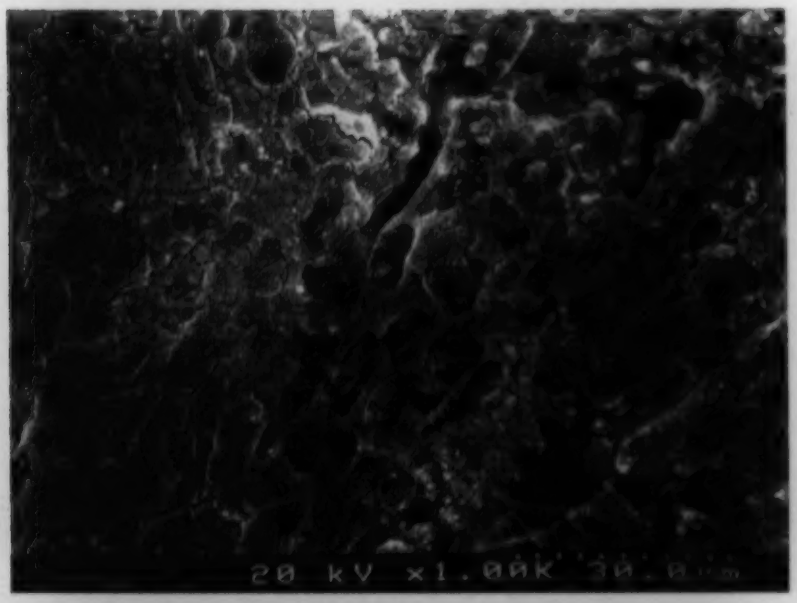

Figure 11-23. Photograph of the working electrode consisting of a platinum thin film 1000 Å thick deposited on the solid electrolyte substrate – 1,033X.

Figure 11-24. Photograph of the working electrode consisting of a platinum thin film 1000 Å thick deposited on the solid electrolyte substrate – 5,167X.

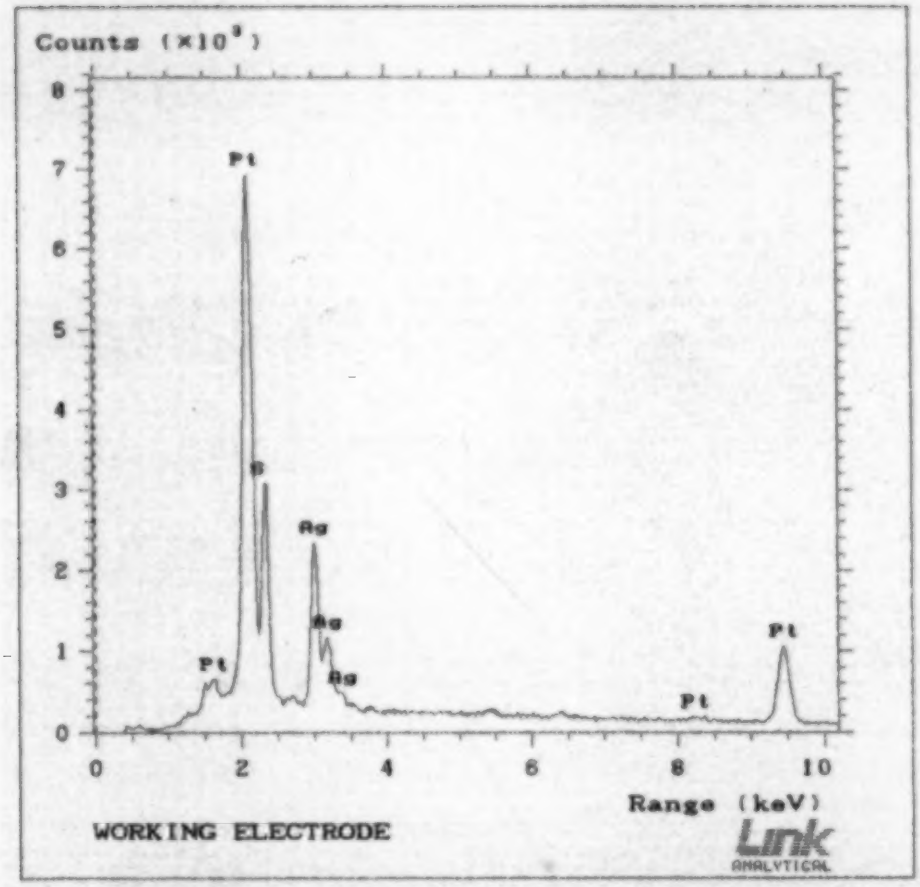

Figure 11-25. Energy dispersive x-ray (EDX) analysis of a working electrode – site No. 1, consisting of a platinum thin film 1000 Å thick deposited on the solid electrolyte.

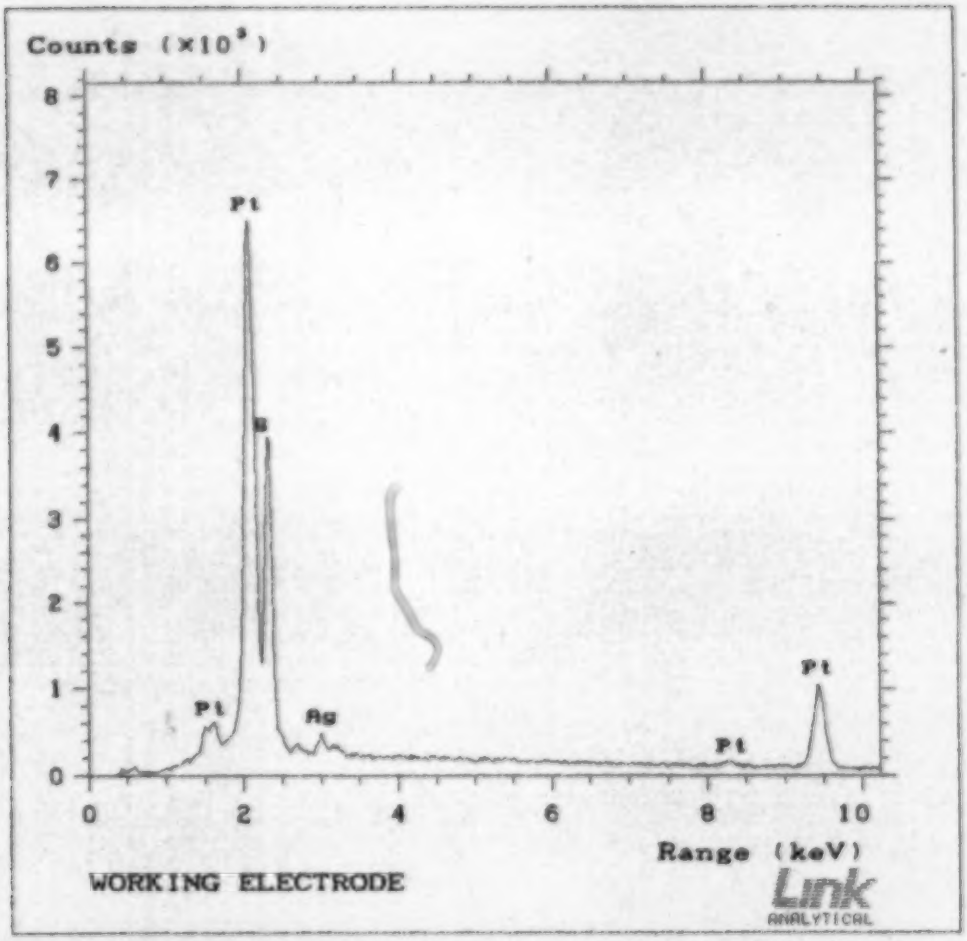

Figure 11-26. Energy dispersive x-ray (EDX) analysis of working electrode – site No. 2, consisting of a platinum thin film (1000 Å thick) deposited on the solid electrolyte.

In the fabrication of cell No. 4 the reference electrode consisted of a composite layer of Ag:Ag_2SO_4-Li_2SO_4 in contact with the electrolyte on one side and a coating of a Pt layer, 10,000Å/1 μm thick on the other side (see Figure 11-27). This Pt layer ensured good electrical contact. The peak observed for Pt was considerably higher in comparison to the other elements present (i.e., Ag and S) as observed in the EDX analysis in Figure 11-28.

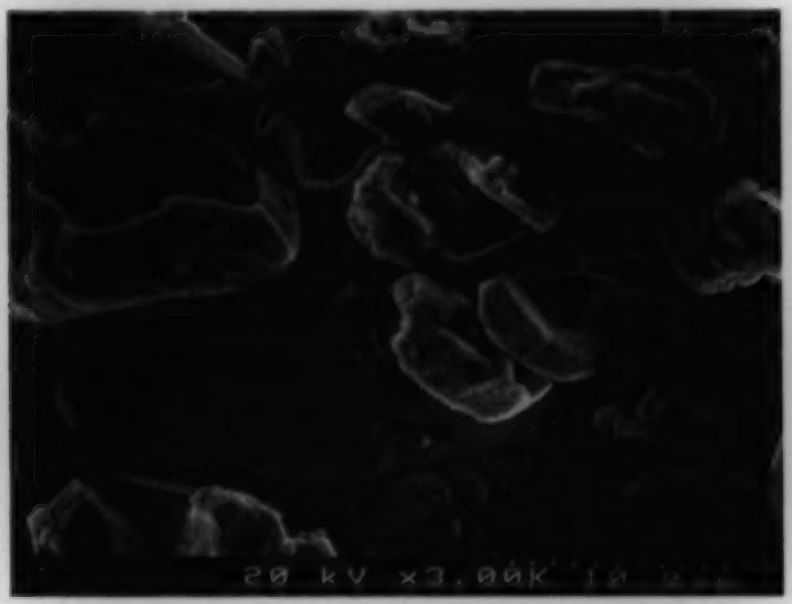

Figure 11-27. Photograph of the reference electrode consisting of a platinum thin film (10,000 Å thick) deposited on the Ag:Ag_2SO_4-Li_2SO_4 reference electrode – 3,100X.

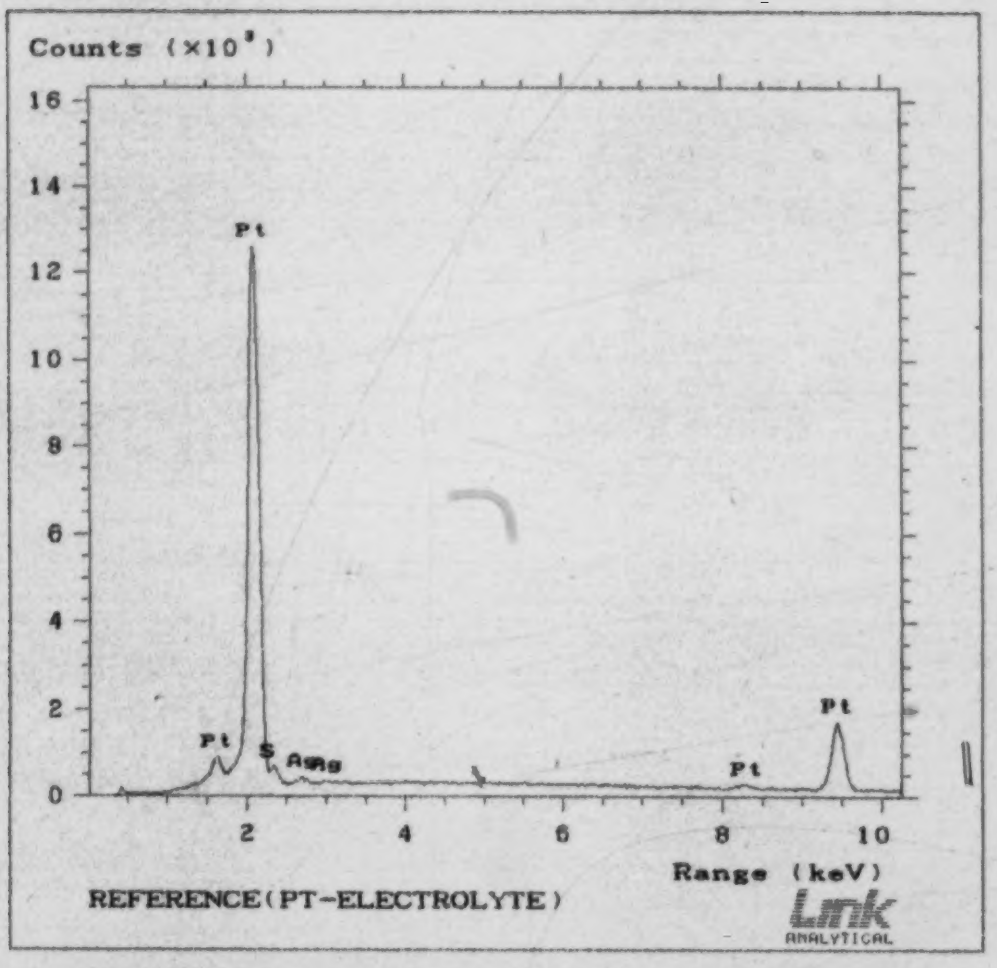

Figure 11-28. Energy dispersive x-ray (EDX) analysis of the Pt thin film (10,000 Å thick) deposited onto the reference electrode.

X-Ray Diffraction Results

Analysis of the materials utilized in the solid electrolyte was performed on the bulk material prior to sintering, on material after sintering and on the electrolyte after testing. These results are presented in Figures 11-29 to 11-31.

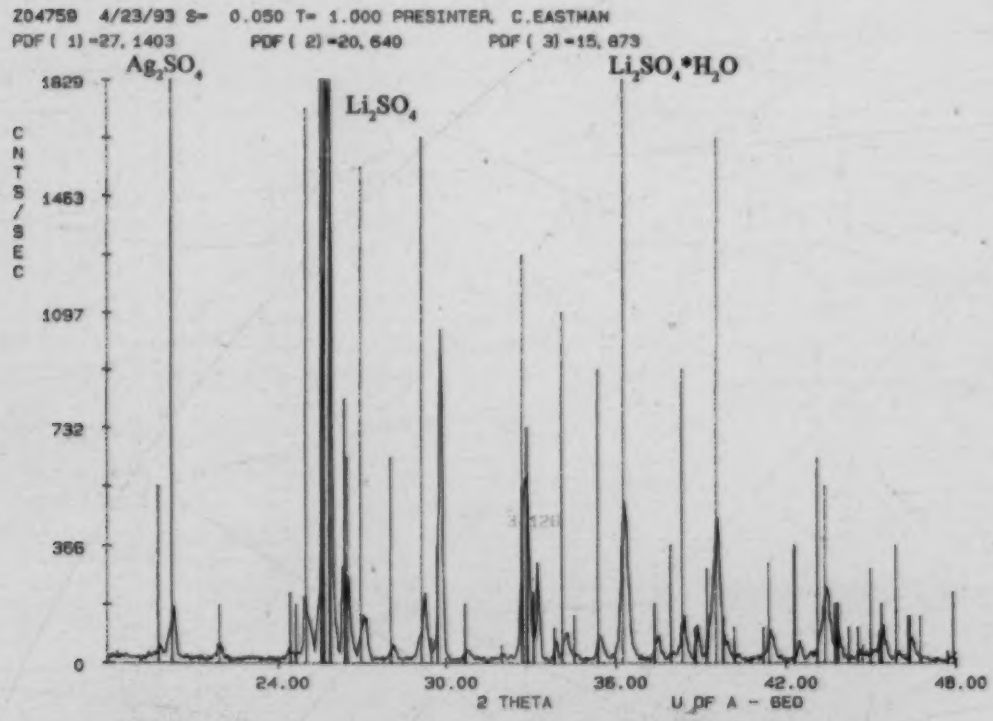

Figure 11-29. X-ray diffraction pattern: pre-sintered material.

Wavelength dispersive x-ray (WDX) analysis is similar to EDX analysis, except that its detector classifies and counts the impinging x-rays in terms of their characteristic wavelengths. The detector system uses an x-ray analyzing crystal that only allows the diffraction of desired wavelengths into the x-ray detector for counting. Advantages of WDX analysis over EDX analysis include:

- Improved energy resolution, preventing many peak overlap errors frequently encountered in EDX analysis

- Lower background noise allowing a more accurate quantitative analysis.

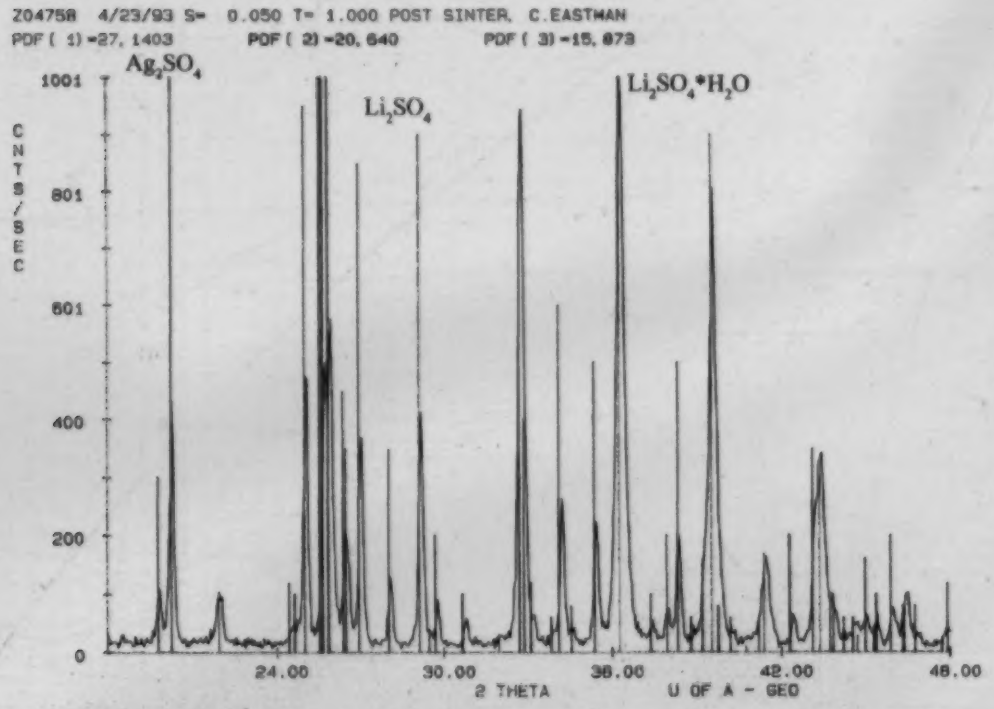

Figure 11-30. X-ray diffraction pattern: post-sintered material.

It is apparent from the analysis of these samples that in addition to the expected Ag_2SO_4 and Li_2SO_4, there was also $Li_2SO_4 \cdot H_2O$ (lithium sulfate monohydrate) present. This is expected since this compound forms readily in the presence of water vapour. At the same time there is no evidence for the formation of hydrated Ag_2SO_4.

In the future assembly of cells or sputter targets consisting of Ag_2SO_4 and Li_2SO_4, special consideration should be given to handling of the materials. It is recommended that Li_2SO_4 should be exposed to only a dry or possibly inert atmosphere during assembly. In addition, Ag_2SO_4 is photosensitive due to the presence of silver and, therefore, should possibly only be exposed to the light from a typical photographic darkroom light (Wratten No. 25 red light filter).

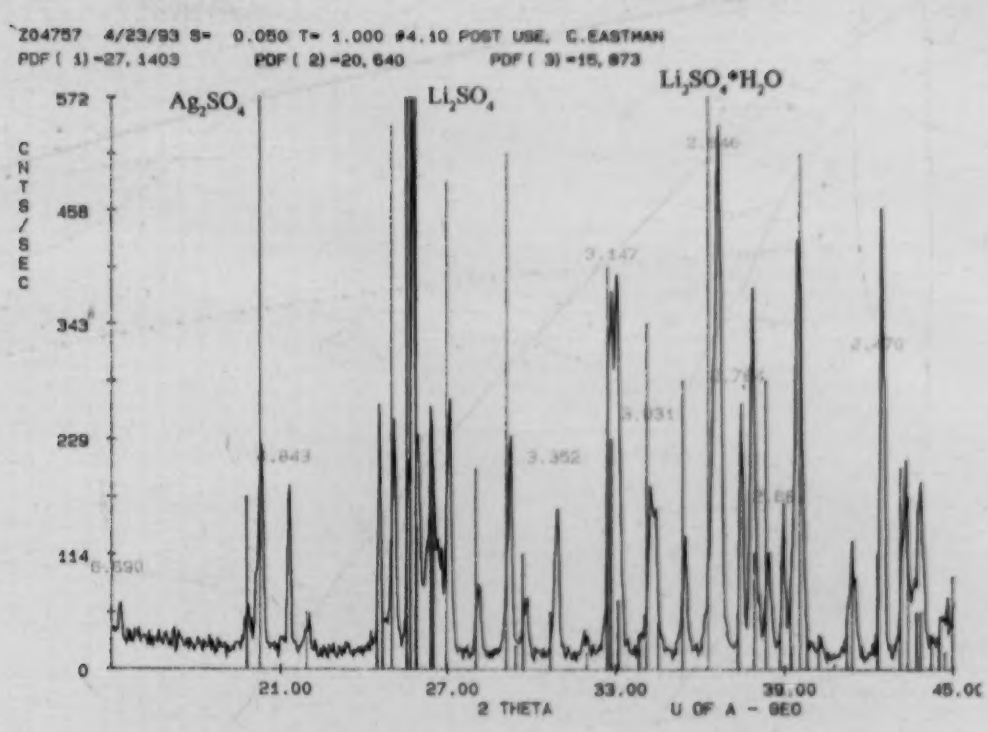

Figure 11-31. X-ray diffraction pattern: post-use material.

Chapter 12 : Discussion of Results

Sensitivity Analysis - Cell Measurements

Analysis of the sensitivity of the cell to changes in temperature and pressure is useful in determining the key factors which influence the emf response of the cell. As previously discussed the overall cell equation is defined by equation 8.4:

$$E = E^{o} + \frac{RT}{2F} \ln \frac{\left(P_{O_2}\right)^{1/2}\left(P_{SO_2}\right)}{a_{Ag_2SO_4}} \qquad (8.4)$$

This equation can be expanded into the following equation:

$$E = E^{o} + \frac{2.3026RT}{2F} log \frac{\left(P_{O_2}\right)^{1/2}}{a_{Ag_2SO_4}} + \frac{2.3026RT}{2F} log\, P_{SO_2} \qquad (12.1)$$

The first two terms in equation 12.1, consisting of the standard cell voltage, E^{o}, the oxygen pressure and activity of Ag_2SO_4 are equivalent to the y-intercept. In equation 12.1 the third term coefficient $\left(\frac{2.3026RT}{2F}\right)$, is equivalent to the slope of the cell equation. To visualize the relationship between the slope versus temperature and pressure, a plot is provided in Figure 12-1. The data from these calculations is provided in Table A-15. As expected from equation 12.1, the slope is related to temperature but not to pressure. There is a linear relationship with temperature as it increases from 525°C to 535°C, with the slope rising significantly. However, the effect of a variance in temperature of ±2 °C, typical of experimental conditions, would result in an error of ±0.0002 V/decade in measurement of the slope.

A plot of the y-intercept from equation 12.1 versus temperature and pressure is displayed in Figure 12-2. The relationship between the y-intercept and temperature is stronger than that with pressure. During acquisition of experimental data, the pressure typically ranged between 690 and 710 mm Hg. At a fixed temperature of 535 °C the effect of this variation in pressure on the y-intercept would be 0.0005 V. Regardless,

compensation for pressure was used in calculation of the experimental emf values. By comparison, the effect of a temperature variation of ±2 °C on the y-intercept for a fixed pressure is ±0.0012V.

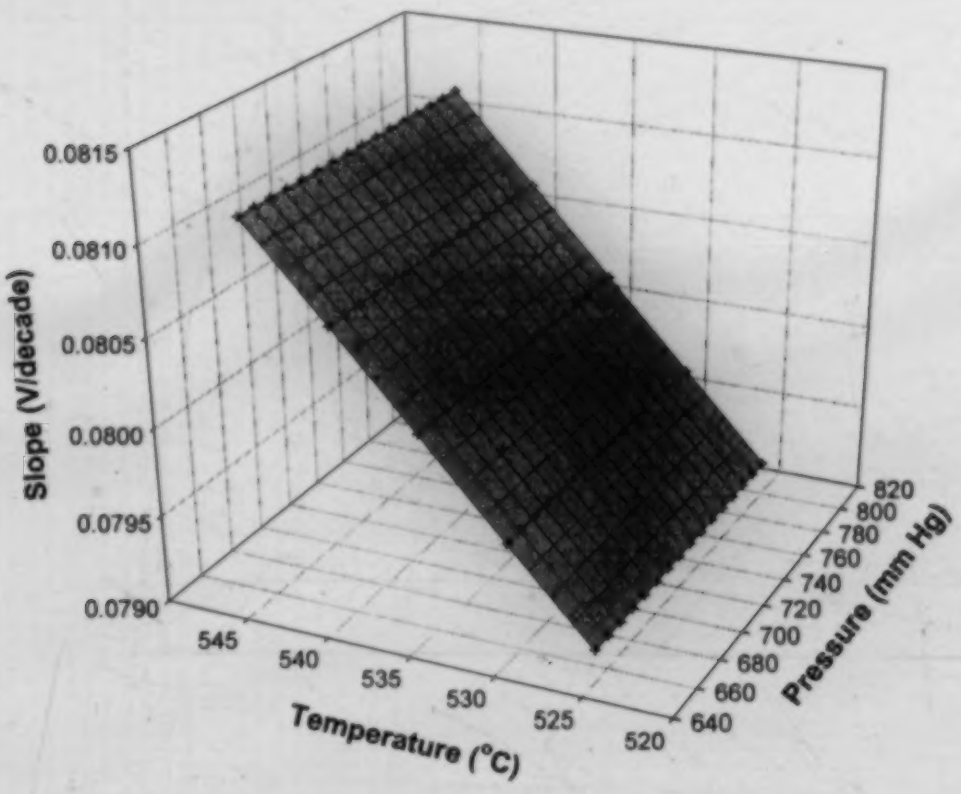

Figure 12-1. Slope versus temperature and pressure

It is apparent that variation in pressure or temperature should be controlled and/or compensated for when collecting experimental data. However, the effect of typical experimental variations in pressure or temperature would have a relatively small influence on the experimental data collected. This is not to say that control of temperature and pressure aren't important, but there are other experimental variables that should be considered. For example, with respect to the third term in equation 12.1, the error in concentration of gas mixtures is ±5%. Assuming a fixed temperature of 535°C/808.15K and a gas concentration of 1000 ±50 ppm of SO_2, the error induced in the cell voltage turns out to be very small at $\pm 5.5 \times 10^{-8}$ V. In comparison

the error in the theoretical value of the y-intercept for the standard voltage, E°, of ±0.0391V is significant when comparing the y-intercept values from theory and experiment. In addition, the free energy for the cell reaction(s), and therefore, the standard cell voltage, E°, have a strong temperature dependence.

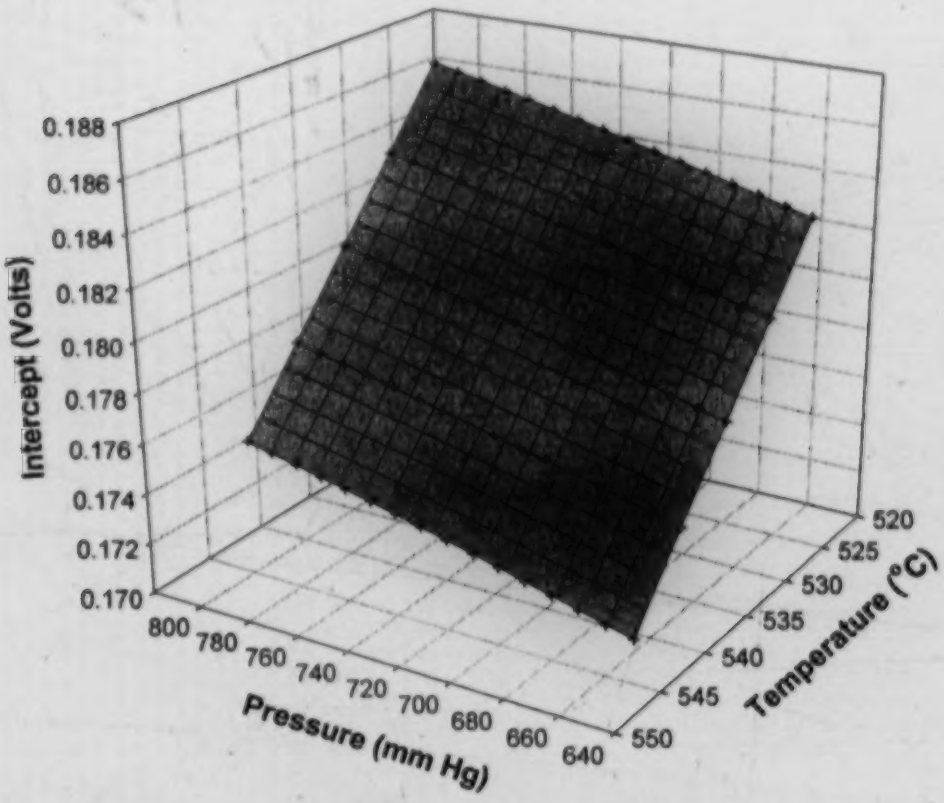

Figure 12-2. Intercept versus temperature and pressure

Cell Measurements

Cell No. 1: Composite reference electrode

This particular cell design consisted of a composite reference electrode attached directly to the two phase solid electrolyte disc with this half cell subsequently co-sintered. The slope of the experimental cell equation was found to be within 9.6% of the theoretical value. However, the y-intercept was in error by 18.3% from the theoretical value. The error in the y-intercept is primarily related to the error in the standard cell emf, E°, and to a lesser degree with the error in the partial pressure of oxygen, P_{O_2}, and the activity of Ag_2SO_4. Pressure was measured to within ±0.1 mm Hg, or ±0.013% of an atmosphere, ranging between 690 to 710 mm Hg during collection of experimental data. Therefore, in calculating the theoretical cell equation, an average pressure value of 700 mm Hg was utilized. If the error were solely related to the Ag_2SO_4 activity for this value of the y-intercept (see equation 12.1), it can be calculated that the $a_{Ag_2SO_4}$ would have to equal 0.1548. Since the solid electrolyte was weighed accurately with a mole fraction of Ag_2SO_4 equal to 0.25, and the activity had been measured experimentally to equal 0.2932, it is unlikely that the activity of the electrolyte was a factor. In comparison the value for E° is equal to 0.6571V with an error of ±0.0391V, or ±6%, a significant error.

There may also be some other factors operating in the cell creating this error. Possibly there are contact potentials being generated between the different components. Impedance spectroscopy could be utilized to determine the impedance or resistances present at the interfaces between the working electrode and electrolyte and the reference electrode and electrolyte. However, slight errors in the individual experimental measurements will lead to more error in the y-intercept than in the slope. At the same time the experimentally determined slope was found to be more accurate in comparison to the theoretical slope. This isn't surprising since the measurement of temperature is precise in comparison to the other measurands. Regardless, with the two phase solid electrolyte and the composite reference

electrode, this cell was found to function reasonably accurately for a relatively long period of time without degradation in cell emf.

Cell No. 2: Ag thin film reference electrode

Utilizing a 5000 Å thick Pt working electrode along with a 8000 Å thick Ag thin film, this cell displayed unstable emf's during its operation. After about three weeks of operation the cell was shut down. Visual observation of the cell revealed that the Ag thin film reference electrode had diffused into the bulk of the solid electrolyte disc. This resulted in the formation of additional Ag_2SO_4 throughout the solid electrolyte, along with the disappearance of the reference electrode. Since the amount of Ag contained in the thin film reference electrode layer is relatively small in comparison to the volume of the solid electrolyte disc, it would have had little effect on the phase amounts within the two phase mixture (i.e., the electrolyte remained in the two phase region). Therefore, the activity of Ag_2SO_4 would have also remained unaffected. Regardless, an increase in the mole fraction of Ag_2SO_4 would have reduced the cell voltage, not increased it as was observed experimentally. Therefore, the rise in voltage towards the end of the experiment was due to some other factor(s).

Cell No. 3: Ag thick film reference electrode

This cell used a Ag thick film, approximately 25μm thick for the reference electrode, along with a working electrode consisting of a 5000 Å thick Pt film. During its operation this cell produced some good results, but only for a relatively short period of time. It appears that diffusion of Ag into the solid electrolyte caused the cell voltage to drop over time. The amount of Ag available in the thick film for diffusion into the solid electrolyte was equivalent to 0.00123 moles. If this material were to diffuse into the solid electrolyte disc it would be converted into 0.000617 moles of Ag_2SO_4, and therefore the mole fraction of Ag_2SO_4 in the solid electrolyte would increase to 0.2538. With the Ag_2SO_4 mole fraction at this level, the solid electrolyte remains in the two phase region. Regardless, the loss of the reference electrode should result in a decline of cell voltage to zero.

It appears that a reference electrode consisting of pure silver changed the mole fraction of the metal sulfate component(s), followed by a subsequent decrease in cell emf. Therefore, it is suggested that an alternative sulfate based solid electrolyte should be utilized where the content of Ag_2SO_4 is close to 100%, such as (0.25 m/o)$BaSO_4$-(99.75 m/o)Ag_2SO_4. Since the activity of Ag_2SO_4 in these types of metal sulfate solid electrolytes is close to unity, any diffusion of Ag into the electrolyte would have negligible effect on the cell emf.

Cell No. 4: Composite thick film reference electrode

Cell No. 4 was fabricated with a thick film reference electrode consisting of a 2:1 weight ratio mixture of Ag:Ag_2SO_4-Li_2SO_4 and a working electrode consisting of a Pt thin film combined with a Pt gauze which produced the best experimental results. From 14.4 to 2400 ppm of SO_2 in air, the y-intercept of the experimental results was within 1.6% of the theoretical value and the slope within 4.1%. An error in the experimental y-intercept is not unexpected since the error in the theoretical standard cell voltage, E°, used to derive the theoretical cell equation is significant at ±0.0391V. Regardless this cell design displayed excellent precision. However, there are some areas that require improvement with respect to measurement at lower gas concentrations. In all cases whether the gas mixture was either mixed or drawn straight out of a gas cylinder, there is a tail in cell emf starting at concentrations below 10-15 ppm of SO_2 in air. There are also some questions with respect to the value of the activity for Ag_2SO_4 in the two phase mixture. The literature indicates that for 23 mol % Ag_2SO_4 – 77 mol% Li_2SO_4 at 530 °C, the activity is equal to 0.25. This activity was measured experimentally to equal 0.2932 ±0.0242. It is possible to calculate activities directly from a phase diagram (when there is solidus and liquidus lines defining the two phase region of interest), however the accuracy is generally poor. Regardless, our two phase region doesn't qualify for calculation from the phase diagram. Therefore, it would be very useful to determine the activity of Ag_2SO_4 at temperatures between 510-560 °C with mole fractions of Ag_2SO_4 between 20-35

mole % via emf measurements. This would clear up any error in operation of this sensor at other temperatures or mole fractions.

Cell No. 5: Thick film electrolyte

This cell was constructed with a 200 μm thick two-layer thick film solid electrolyte onto which a 1000 Å thick thin film of Pt was deposited forming the working electrode. The two layered electrolyte structure was an attempt to form a gas tight layer required for functionality. However, as the experimental results show, the electrolyte layer did not perform properly. The response was inconsistent and unstable throughout the range in SO_2 concentration. Throughout the literature it is apparent that the formation of thin films of Ag_2SO_4-Li_2SO_4 or other metal sulfates has not been achieved. Metal sulfates are difficult compounds to deposit as thin or thick films. It is suggested that using air brushing with very fine particles << 1 μm should be examined as a deposition method.

General Discussion

The sensor is capable of accurately measuring SO_2 concentrations assuming that the sample input consisting of air and SO_2 entering the sensor doesn't initially contain SO_3. In addition, the sensor is capable of measuring SO_3 contents in sensor stream inputs consisting of a carrier gas and pure SO_3 only or total SO_2/SO_3 concentrations.

The important factors to be considered with this sensor design consist of:

- The activity of Ag_2SO_4 is constant in the two phase region even as the amount of each of the phases changes. In comparison, single phase systems such as Ag_2SO_4-K_2SO_4 or Ag_2SO_4-Na_2SO_4 form a continuous solid solution over a range of composition. Single phase cells will be affected by variations in the concentration of silver sulfate. These variations are due to decomposition of the Ag_2SO_4 or reaction of silver in the reference electrode with SO_3 to form Ag_2SO_4. These problems are of less concern with two phase sulfate solid electrolytes and result in long term stability.

- By embedding Ag in the Ag_2SO_4-Li_2SO_4 mixture in the reference electrode, the sulfation of silver by gaseous SO_3 is minimized or virtually eliminated.

- The composite reference electrode mixture provides fixed SO_3 potentials and when sintered as one integral piece with the solid electrolyte, results in good electrical contact between the electrolyte and reference electrode material.

- Silver has the unique property of being stable above 200 °C in oxidizing atmospheres and its sulfate, Ag_2SO_4 is also stable. As observed in the potential phase diagrams (see Figures 12-5 to 12-7) for Ag-S-O, there is no silver oxide formed as an intermediary phase between Ag and Ag_2SO_4.

- Two phase electrolytes also absorb water less and have better mechanical properties.

Despite the excellent results above 10 ppm, the sensor should be capable of detecting to sub-ppm levels. The relationship between cell voltage and the SO_2 concentration should be linear into the sub-ppm concentrations. Below a concentration of 10-12 ppm SO_2 (equal to 10-12 ppm SO_3 at the surface of the sensor) the measured voltage departs from the expected values. From the difference in the measured voltage and that calculated by the theoretical cell equation, it would indicate that there is a perturbation in either the P_{O_2} or P_{SO_3} partial pressures present at the working electrode.

Voltage Differential and Shift in Partial Pressures

To acquire an understanding of the non-linear voltage shift at lower concentrations (i.e., 0.6 to 10 ppm SO_2), a calculation of the change in P_{O_2} or P_{SO_3} partial pressures required for the shift from the expected theoretical values has been formulated. The shift in voltage is defined by the difference in voltage, ΔE, between the experimentally observed voltage, E'_{exp}, and the theoretical voltage, $E'_{theoretical}$:

$$\Delta E = E'_{exp} - E'_{theoretical} \tag{12.2}$$

From the overall cell reaction given by equation 8.4, it can be shown that:

$$\Delta E = \frac{RT}{2F} \ln \frac{\left(PO_2^{*}\right)^{1/2}\left(PSO_3^{*}\right)}{\left(PO_2^{'}\right)^{1/2}\left(PSO_3^{'}\right)} \tag{12.3}$$

where PO_2^{*} represents the oxygen partial pressure present during experimental measurements, $PO_2^{'}$ that expected according to theory (i.e., 0.209476 times the measured pressure), PSO_3^{*} is the partial pressure of SO_3 measured at the sensor cathode, and $PSO_3^{'}$ that expected according to the input mixture.

In Table 12-1 values for the experimental and theoretical voltages are given. The voltage shift ΔE between these two voltages is calculated along with the required shift in either the oxygen or SO_3 partial pressures.

The shifted oxygen pressure is calculated from the voltage shift that would be required at a given partial pressure of SO_3 to produce the experimentally observed cell voltage. It also follows that the shifted P_{SO_3} partial pressure is calculated assuming that the oxygen partial pressure is unchanged.

Table 12-1. Voltage and partial pressure shift.

$[SO_2]$ ppm	Experimental Voltage	Theoretical Voltage	ΔE	Shifted Oxygen Pressure (atm)	Shifted $[SO_2]$ ppm
0.6	0.2460	0.1624	0.0835	25.4	6.6
1	0.2470	0.1802	0.0668	9.74	6.8
2	0.2497	0.2043	0.0453	2.83	7.4
3	0.2522	0.2185	0.0337	1.45	7.9
4	0.2546	0.2285	0.0261	0.9376	8.5
5	0.2568	0.2362	0.0206	0.6838	9.0
6	0.2590	0.2426	0.0164	0.5375	9.6
7	0.2610	0.2480	0.0131	0.4440	10.2
8	0.2630	0.2526	0.0104	0.3797	10.8
9	0.2648	0.2567	0.0081	0.3328	11.3
10	0.2665	0.2604	0.0061	0.2970	11.9

What might be responsible for this voltage shift upwards at low SO_2 concentrations?

1. The gas was not mixed properly at lower concentrations. This is unlikely for the following reasons; two gas cylinders with certified mixtures consisting of 0.6 ppm SO_2 in air and with 11.6 ppm SO_2 in air were utilized, without any mixing. Below 11.6 ppm the gas was diluted with an air stream. At the lowest concentration tested, 0.6 ppm SO_2 in air, the test gas consisted of an undiluted stream from a certified mixture. The cell voltage followed the trend with respect to the difference between the measured and theoretically calculated

cell voltage; therefore, it is unlikely that improper mixing of the gases was involved.

2. Did proper purging of the gas mixture occur inside the test chamber? To ensure that effective purging of the chamber took place, when the gas mixture was adjusted to 0.6 ppm, the chamber was purged for a couple of days. Also, the test procedure was cycled several times between 0.6 and 11.6 ppm SO_2 over several weeks. And since the voltage differential was relatively consistent and repeatable over many cycles, chamber purging is deemed to be effective.

3. Was there leakage across the sensor from the reference side? The cell was pressure tested with a few pounds of air applied to both the reference and working electrode chambers. No leakage was observed with a bubbler connected to either side. Regardless, leakage of air across the sensor from the reference electrode to the working electrode side would have caused dilution of the gas stream at the working electrode and a drop in cell voltage – opposite of what was observed. In addition, the reference side of the cell was exposed to static air pressure, not pressurized air. If the cell were to leak SO_2 it would have appeared on the reference electrode side. In conclusion, the cell was gas tight and the transference of gas across the sensor was not observed.

4. Thermal diffusion. If a temperature gradient is applied to a mixture of two gases of uniform concentration, there is a tendency for the heavier and larger gas molecules (mass, m_1 and diameter, δ_1) to move to the cold side, and for the lighter and smaller molecules (mass, m_2 and diameter, δ_2) to move to the hot side. At steady state there is a separation of light and heavy gas molecules due to a balance between the mixing effect of ordinary diffusion (coefficient D_{12}) and thermal diffusion (coefficient D_T) resulting in a concentration gradient due to the temperature gradient. The amount of thermal separation depends upon the ratio of m_1/m_2, the ratio δ_1/δ_2 the proportion of the

volume of the heavier gas, f_1, and of the lighter gas, f_2, and of the strength of the attractive/repulsive force between the different gas molecules.

Within the test apparatus a temperature gradient existed between the location of the sensor (at 535 °C) in the middle of the hot zone to the inlet of the furnace tube located outside the furnace. The temperature profile for the tube furnace with the controller set at 540 °C is given in Table 12-2 (measured from the end of the tube to the other side). During operation of the cell, the furnace controller was adjusted so the cell would be at 535 °C. At this setting the temperature at the end of the tube is approximately 426 °C less than the centre.

Therefore, it is expected that the temperature gradient (~420 °C) that exists between the sensor and the outer region of the furnace test tube will result in separation of the three primary gases, oxygen, nitrogen and sulfur trioxide down the length of the tube. There would also be a radial temperature gradient between the sensor body and the furnace walls adjacent to the sensor; however, this is expected to be significantly less. Regardless, the lighter gases, oxygen and nitrogen, will diffuse towards the inner hotter regions of the tube, with the sulfur trioxide migrating to the cooler outer portions of the tube. The SO_2 entering the cell is converted to SO_3, with the MW_{SO_3} equal to 80 g/mol whereas the oxygen and nitrogen possess molecular weights of MW_{O_2} = 32 g/mol and MW_{N_2} = 28 g/mol, respectively. According to the overall cell reaction given by:

$$E = E^{o} + \frac{RT}{2F} \ln \frac{\left(P_{O_2}\right)^{1/2}\left(P_{SO_3}\right)}{a_{Ag_2SO_4}}$$

enrichment of oxygen at the sensor would increase the cell voltage, while a decrease of sulfur trioxide at the sensor body would lower the cell voltage.

Which gas component is enriched or depleted more will determine whether the cell voltage increases or decreases. Therefore, thermal gas diffusion may or may not explain the lack of Nernstian response below 5-10 ppm. An analysis of the thermal diffusion is required. The magnitude of the radial temperature gradient located between the sensor and the furnace tube was not measured, but this gradient would have been much less than the axial gradient. Regardless, there may have been some enrichment of sulfur trioxide next to the sensor due to radial separation. However, the gradient down the length of the tube creates a much larger gas concentration gradient.

Table 12-2. Furnace temperature profile.

Distance In (cm)	Temperature °C
0	118
5	167
10	174
15	224
20	291
25	339
30	398
35	468
40	519
45	538
50	544
55	524
60	478
65	414
68	352

It is useful to determine what the concentration gradient for oxygen and sulfur trioxide is down the length of the furnace tube. The description of thermal diffusion of gases is somewhat complex and will be briefly described. For a

thorough description of thermal diffusion see "Thermal Diffusion in Gases" by Grew and Ibbs [92] or "The Thermal Diffusion Column" by Vasaru et al. [93]. For a binary gas mixture under the condition of steady state diffusion, the flux is given by:

$$\text{grad}\, c_1 = k_T\, \text{grad}\, \ln T \tag{12.4}$$

where k_T is the thermal diffusion ratio given by:

$$k_T = \frac{D_T}{D_{12}} \tag{12.5}$$

and D_{12} is the coefficient of ordinary diffusion of a binary gas mixture and D_T is the thermal diffusion coefficient.

It follows from equation 12.4 that the concentration gradient is, therefore, given by:

$$[c_1]_2 - [c_1]_1 = \alpha_T c_1 c_2 \ln \frac{T_2}{T_1} \tag{12.6}$$

where the term on the left side (i.e., $[c_1]_2 - [c_1]_1$) represents the gradient in concentration of the first species between the two locations as indicated by the subscripts 1 and 2 outside the brackets, α_T is the thermal diffusion constant and c_1 and c_2 are the initial concentrations of the two gases.

Since the dependence of k_T on composition is strong, it is convenient to utilize the thermal diffusion constant defined by:

$$\alpha_T = \frac{k_T}{c_1 c_2} \tag{12.7}$$

which includes a term for concentration and is, therefore, less dependent on

composition.

Another term found in the literature is the thermal separation ratio, R_T, which is defined as the ratio of k_T (experimental) or α_T (experimental) obtained from experimental data, to the theoretical values calculated using a rigid elastic sphere (R.E.S.) model. The equation is of the form:

$$R_T = \frac{k_T\,(\text{exp.})}{k_T\,(\text{R.E.S.})} = \frac{\alpha_T\,(\text{exp.})}{\alpha_T\,(\text{R.E.S.})} \tag{12.8}$$

Values for R_T typically vary between 0.1 to 0.7.

The general theory for thermal diffusion in ternary and polynary gas mixtures can be somewhat modified as outlined by Hellund [94] and Jones [95]. However, in the case where the molecules only differ with respect to their masses, the thermal diffusion equation can be written in terms of the binary thermal diffusion constant. The gas stream used in testing the chemical sensor consists primarily of three gases: sulfur trioxide, oxygen and nitrogen. In this situation the thermal diffusion equation 12.6 is re-written for a ternary gas mixture as:

$$\Delta c_1 = [c_1]_2 - [c_1]_1 = (\alpha_{12}c_2 + \alpha_{13}c_3)\ln\frac{T_2}{T_1} \tag{12.9}$$

For this work involving O_2, N_2 and SO_3 in case of the separation of oxygen, equation 12.9 can be modified to:

$$\Delta c_{O_2} = [c_{O_2}]_2 - [c_{O_2}]_1 = (\alpha_{O_2\text{-}N_2}c_{N_2} + \alpha_{O_2\text{-}SO_3}c_{SO_3})\ln\frac{T_2}{T_1} \tag{12.10}$$

and for separation of SO_3:

$$\Delta c_{SO_3} = [c_{SO_3}]_2 - [c_{SO_3}]_1 = (\alpha_{SO_3\text{-}N_2}c_{N_2} + \alpha_{SO_3\text{-}O_2}c_{O_2})\ln\frac{T_2}{T_1} \tag{12.11}$$

For an approximate calculation of the thermal diffusion constant, α_T, the rigid elastic sphere model along with the approximation given by Chapman-Enskog for mixtures of molecules with similar diameters and or masses [93] is as follows:

$$[\alpha_T]_i = \frac{105}{118}\frac{M_i - M_{i+1}}{M_i + M_{i+1}} \tag{12.12}$$

Utilizing a temperature gradient of 420 °C (i.e. 535-115 °C), assuming that the thermal separation ratio, R_T, equals unity, and using the Chapman-Enskog approximation for the thermal diffusion constant, the following value for the separation of O_2 down the length of the tube was determined:

$$\Delta c_{O_2} = 0.034 \tag{12.13}$$

Therefore, with the initial concentration of oxygen at 0.2095 atm, the final concentration in the hot zone would become ~ 0.2434 atm. This value was calculated for a $[SO_2]$ = 5 ppm.

For a change in SO_3 concentration:

$$\Delta c_{SO_3} = 0.3038 \tag{12.14}$$

Therefore, if the concentration of SO_3 were equal to 10 ppm it would increase by a relatively small amount to 10.3 ppm. And since the change in SO_3 would be constant over the entire range of $[SO_3]$, it would have even a smaller effect at higher concentrations.

Regardless, the increase in oxygen concentration is significant and the effect of $[SO_2]$ has little influence in the change in oxygen over the entire range the sensor operated. Therefore, due to the change in the partial pressure of

oxygen, ΔP_{O_2}, one would expect to see a large perturbation in the sensor voltage over the entire range of [SO_2] measured. This was not observed as the sensor obeyed the expected response above concentrations of 10 ppm SO_2. In addition, since the gas was flowing through the cell at 30 sccm whereas thermal diffusion calculations assumed a stagnant gas mixture, a perturbation in cell voltage due to thermal diffusion should have been further minimized or not present at all.

Some further suggestions for determining whether thermal diffusion is at play in this sensor:

Measure the cell voltage with the gas mixture contained within the full open length of the tube. Then for comparison measure the cell voltage with a sensor placed in an isolated test chamber in the hot zone of the furnace. If the sensor is capable of measuring gas mixtures with concentrations less than 10 ppm of SO_2 then thermal diffusion is a factor with an open tube test chamber.

It would also be useful in utilizing a gas mixture with a known concentration of SO_3 gas delivered in an alternative carrier gas. By using a carrier gas with a significantly different molecular weight, i.e. MW_{He} = 2 g/mol, any effect on cell voltage due to thermal diffusion would be readily observed.

5. Concentration polarization. This effect is well understood with oxygen concentration cells constructed of O^{2-} mobile ZrO_2-Y_2O_3 solid state electrolytes. At open circuit, the movement of oxygen anions from the cathode to the anode under conditions of mixed conduction (when t_{ion} <1) will occur since electrons can travel within the solid electrolyte to the cathode to neutralize the effect of the charge imbalance. At the cathode, the production of oxygen anions occurs according to the reaction, $\frac{1}{2}O_2 + 2e^- \rightleftharpoons O^{2-}$. Whereas, at the anode, the arriving oxygen anions will produce oxygen according to the reaction, $O^{2-} \rightleftharpoons \frac{1}{2}O_2 + 2e^-$. The oxygen produced at the surface of the anode,

if physically adsorbed on the surface, will result in a measured oxygen concentration higher than the bulk oxygen concentration (see Figure 12-3). This adsorbed layer of oxygen at the surface of the anode will result in a drop of the measured cell voltage or emf. Of course, it may be possible to flush this absorbed concentration of oxygen atoms/molecules off the surface of the electrode with higher flow rates of gas.

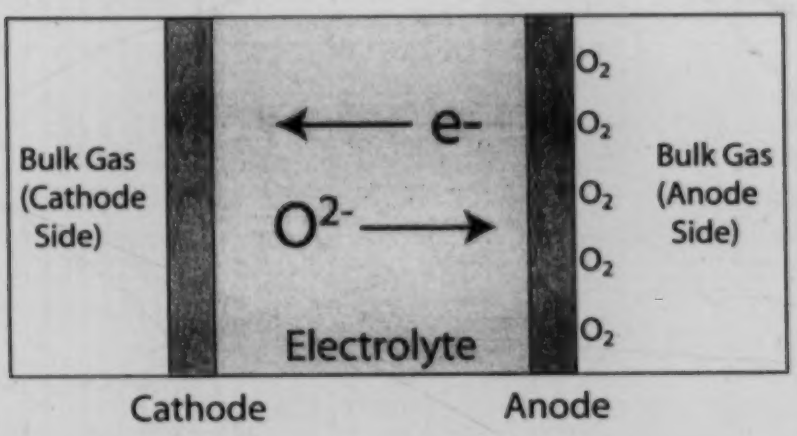

Figure 12-3. Polarization in an oxygen concentration cell.

In a similar fashion, a sulfur dioxide chemical sensor with mixed conduction would also have transference of both ions and electrons (see Figure 12-4). However, in this situation the mobile cation consists of Ag^+, which travels from the anode to the cathode. It follows with a mixed ionic conductor that this ionic current is offset by the movement of electrons (e-) in the same direction. At the cathode the electrons react with SO_3 and O_2 gas according to the reaction, $SO_3 + \frac{1}{2}O_2 + 2e^- \rightleftharpoons SO_4^{2-}$. The net result is a reduction of gas concentration in the polarized gas layer, next to the cathode. For this type of sensor, a drop in the cell voltage would also be expected, according to the overall cell reaction as given by equation 8.4.

According to what was measured experimentally, this theory is opposite to what was observed; the experimental evidence displays a rising tail in cell

voltage at lower gas concentrations, with the gap between the experimental and theoretical values widening with declining gas concentration. Therefore, it would appear that concentration polarization is not the reason for the non-linear behaviour in the cell voltage at lower gas concentrations. On the other hand, concentration polarization can explain low cell voltages observed in relation to the lower flow rates as observed in the flow rate dependence tests (see Figures 11-17 to 11-19).

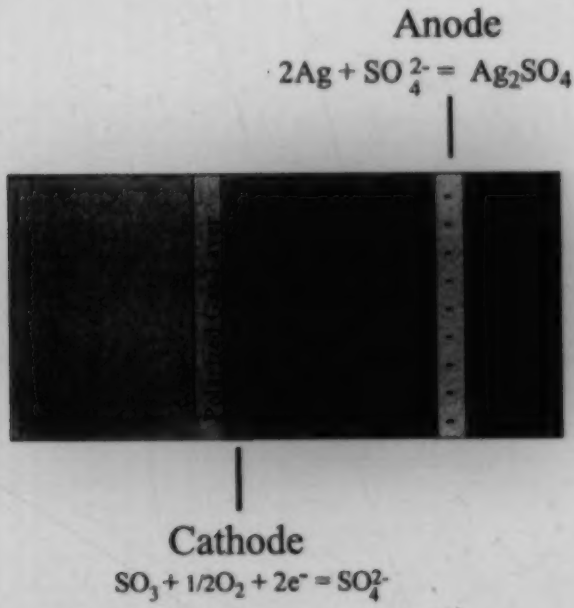

Figure 12-4. Cross section of sensor layers and reactions.

6. Decomposition of the solid electrolyte. Another possibility to consider is the decomposition of the two-phase solid electrolyte utilized in this work consisting of $(Ag,Li)_2SO_4$ss and αLi_2SO_4ss at lower partial pressures of SO_2 in air. There is no information in the literature with respect to decomposition of the two-phase solid electrolyte material in relation to SO_2. Therefore, consideration will be given to the assumption that the solid electrolyte can be analyzed as two separate components consisting of Ag_2SO_4 and Li_2SO_4.

For Ag_2SO_4:

$$Ag_2SO_4 \rightleftharpoons 2Ag + SO_3 + \tfrac{1}{2}O_2 \quad \Delta G_f^\circ = +126.8\,kJ/mol \text{ at } 535^\circ C/8081.5K \quad (12.15)$$

The cell emf was observed to depart from a Nernstian response at concentrations below 10 ppm SO_2 in air. Therefore, for the operating condition where $P_{SO_2} = P_{SO_3} = 10$ ppm and $P_{O_2} = 0.2095$ atm, the free energy for the decomposition of Ag_2SO_4 is approximately +51.4 kJ/mol. This calculation indicates that silver sulfate should not spontaneously decompose at 10 ppm. Assuming that the thermodynamic data are accurate, it can be shown that decomposition of Ag_2SO_4 will not occur until the $[SO_2]$ is below ~5 ppb.

For Li_2SO_4:

$$Li_2SO_4 \rightleftharpoons 2Li + SO_3 + \tfrac{1}{2}O_2 \quad \Delta G_f^\circ = +798\,kJ/mol \text{ at } 535^\circ C/808.15K \quad (12.16)$$

The free energy of decomposition for Li_2SO_4 at $P_{SO_3} = 10$ ppm is highly positive, making it even less favourable for decomposition to occur. It can be calculated that the theoretical decomposition of Li_2SO_4 occurs at a P_{SO_3} pressure of approximately 5.6×10^{-52} atm.

There is a strong relationship between the decomposition of Ag_2SO_4 and temperature. In Figures 12-5, 12-6 and 12-7 phase stability diagrams for the Ag-S-O system at various temperatures are provided. On each of these stability diagrams, the curves marked by a dashed line are in reference to a total pressure of 1 atm. However, during operation of the sulfur oxide sensor, the total pressure of air and SO_2 was actually equal to ~0.921 atm. Therefore, the total pressure curves marked on the phase stability diagrams should be shifted slightly down and to the left. Regardless, according to these diagrams, at 673K (400 °C) Ag_2SO_4 would decompose at a partial pressure of SO_2 equal to 10^{-15}-10^{-16} atm. At 808K (535 °C) Ag_2SO_4 decomposition occurs at a partial pressure of SO_2 equal to ~10^{-10} atm and at 873K (600 °C) at a partial pressure

of SO_2 equal to 10^{-8}-10^{-9} atm. Therefore, as the temperature increases, the pressure of SO_2 required to prevent decomposition of Ag_2SO_4 also increases. According to this thermodynamic analysis it would be advantageous to lower the operating temperature of Ag_2SO_4 based sensors, so as to permit the measurement of lower SO_2 pressures.

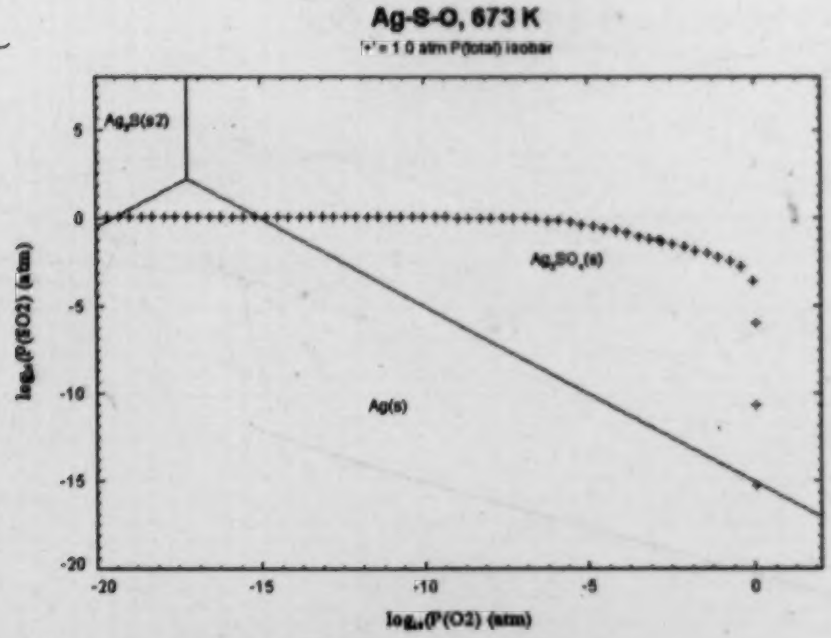

Figure 12-5. Phase stability for the Ag-S-O system at 673K.

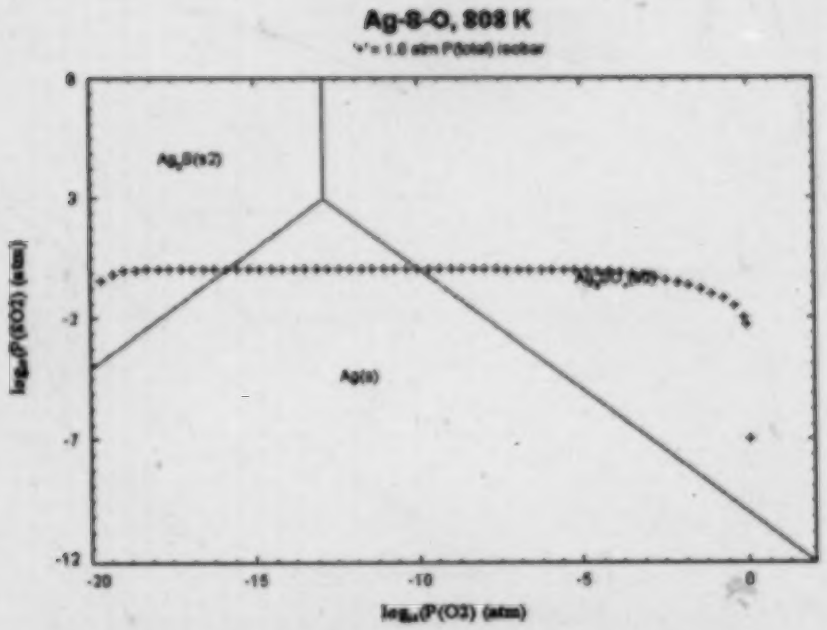

Figure 12-6. Phase stability for the Ag-S-O system at 808K.

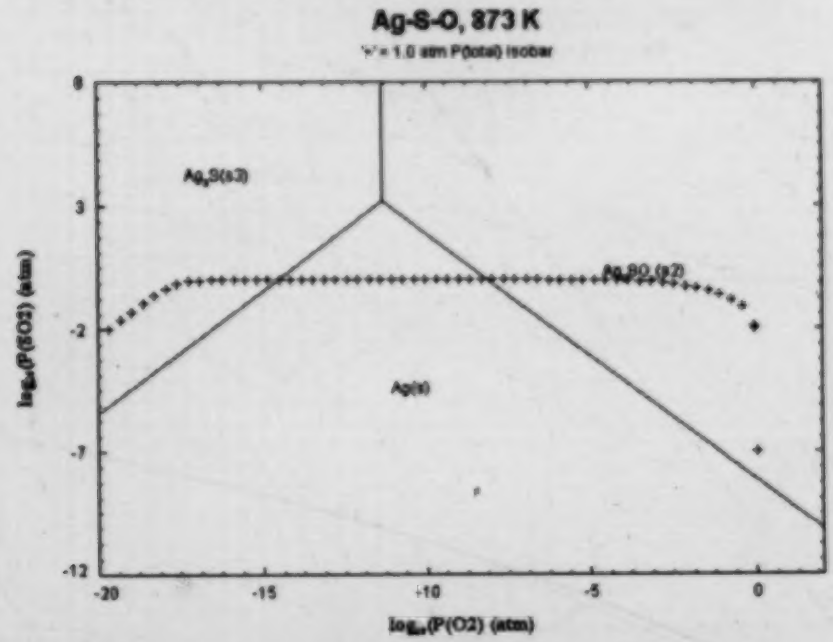

Figure 12-7. Phase stability for the Ag-S-O system at 873K.

From this simplified analysis, it is apparent that if decomposition were to occur, Ag_2SO_4 would be the more likely candidate. However, the solid electrolyte utilized in this work consists of the two phases: αLi_2SO_4ss and $(Ag, Li)_2SO_4$ss, and therefore would respond differently than the simplified analysis discussed in the previous section. The response of the sensor at lower SO_2 concentrations is displayed in Figure 12-8. There is a plateau in the emf as the concentration of SO_2 in air decreases under 10 ppm. The plateau can be described by the following equation:

$$E = E^{\circ} + \frac{2.3026RT}{2F} log \frac{\left(P_{O_2}\right)^{1/2}\left(P_{SO_2}\right)}{a^{\circ}_{Ag_2SO_4}} \qquad (12.17)$$

where $a^{\circ}_{Ag_2SO_4}$ is the effective activity of Ag_2SO_4 in the solid electrolyte as decomposition begins to occur. In this situation the activity is not a constant value.

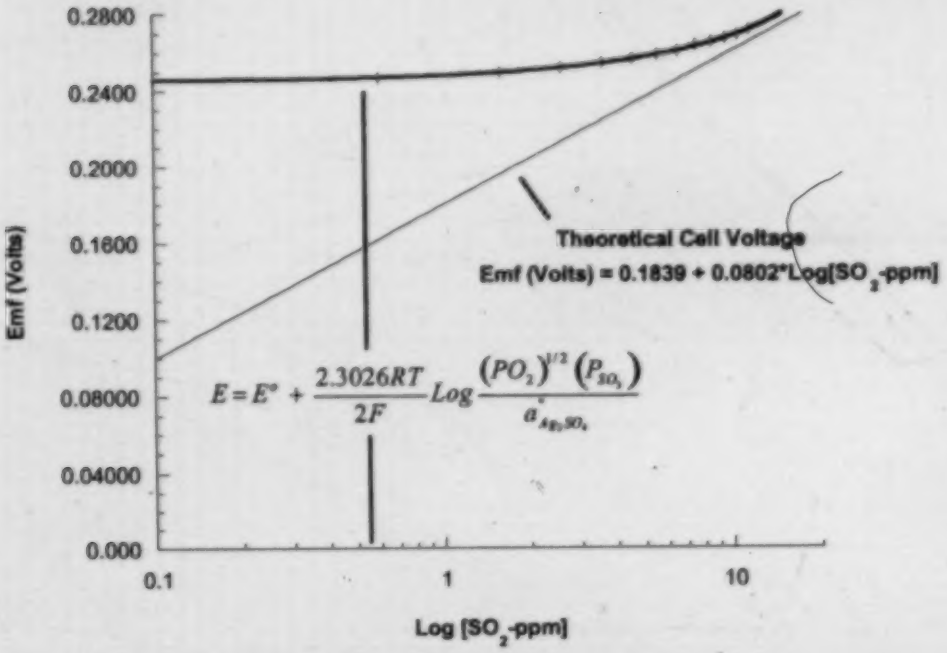

Figure 12-8. Emf versus log[SO_2-ppm] at low SO_2 concentrations.

As the $[SO_2]$ decreases, if the assumption is made that the $(Ag, Li)_2SO_4ss$ phase begins to decompose into Ag, Li, O_2 and SO_3, this would result in a decline in the effective activity of Ag_2SO_4 ($a^{\circ}_{Ag_2SO_4}$) as defined in equation 12.17. A decline in the activity would, therefore, reduce the effect of the second term in equation 12.17 and create a plateau in the measured emf.

In Table 12-3 the effective activity for Ag_2SO_4($a^{\circ}_{Ag_2SO_4}$) is given according to the concentration of $[SO_2]$ and the measured emf. The values for the activity of $(Ag, Li)_2SO_4ss$ would indicate, that as the concentration of SO_2 decreases, the amount of $(Ag, Li)_2SO_4ss$ transformed increases significantly.

Table 12-3. Adjusted Ag_2SO_4 activity

[SO2-ppm]	Emf (Volts)	Effective Activity
0.6	0.2471	0.0220
1.6	0.2500	0.0539
2.6	0.2523	0.0820
3.6	0.2545	0.1065
4.6	0.2567	0.1278
5.6	0.2587	0.1469
6.6	0.2605	0.1644
7.6	0.2638	0.1722
8.6	0.2656	0.1850
9.6	0.2673	0.1967
10.6	0.2693	0.2051
11.6	0.2720	0.2077

Chapter 13: Conclusions, Future Work and Recommendations

Several two-phase Ag_2SO_4-Li_2SO_4 sensors were designed and tested with a range of gas mixtures varying from 0.6 to 2400 ppm SO_2 in a stream of air. The best performance was observed with a design consisting of a Ag:Ag_2SO_4-Li_2SO_4 thick film reference electrode deposited onto a disc substrate consisting of the two phase electrolyte, Ag_2SO_4-Li_2SO_4. Testing of this design occurred over several months with continuous cycling from high to low gas concentrations for confirmation of reproducibility. This sensor was accurate to better than 5% and in some cases in the range of between 1 and 2% of the theoretically calculated values from 14.4 to 2400 ppm SO_2. However, improvement in the performance of the gas sensor at gas concentrations below 10 ppm SO_2 is required. Determination of the exchange current density for the working electrode is recommended for a better understanding of electrode kinetics, especially at lower gas concentrations.

The Ag_2SO_4 activity for a 25m/o Ag_2SO_4 – 75m/o Li_2SO_4 mixture at 535 °C has been determined to be 0.2986 ±0.0265, which is a reasonable value in comparison to that present in the literature. However, a more thorough examination of Ag_2SO_4 activity in relation to temperature and mole fraction of Ag_2SO_4 is recommended.

With development of a functional thick or thin film electrolyte of Ag_2SO_4-Li_2SO_4 it would be possible to construct a miniaturized integrated sulfur oxide sensor for the measurement of SO_2/SO_3 in air. This integrated sensor would offer several advantages with lower power consumption, faster response times, lower unit cost and compactness. The fabrication of sensors for other gases such as NO_x, CO_x, Cl_2, O_2, and H_2 with the techniques utilized in this work would be amenable to further miniaturization and integration.

The work presented has laid the groundwork for the development of a miniaturized, integrated chemical sensor. Utilizing semiconductor manufacturing and micromachining techniques additional work is required for fabrication of a miniaturized and integrated sensor. This work consists of the following:

- Selection of the optimal solid electrolyte combined with appropriate reference and working electrodes
- Development of a deposition process for a dense, gas tight thin film solid electrolyte
- Development of a sensor design and fabrication process for integration and miniaturization of the sensor

Improved Electrolyte

A change in the electrolyte and reference electrode can simplify fabrication of the chemical sensor. The two-phase sulfate utilized in this work displays excellent selectivity and stability in the measurement of SO_2/SO_3 . However, the operational range is relatively narrow (i.e., 520-560 °C) and errors in measurement could take place if the composition of the solid electrolyte is moved out of the two-phase region. As discussed previously there are several alternate choices in composite electrolytes to be considered. These additions to Ag_2SO_4 consist of:

Cs_2SO_4 – Increased the ionic conductivity of the parent Ag_2SO_4 material by a factor of 33X, a significant improvement. This material also has a large range of applicability all the way down to $P_{SO_2} = 10^{-28}$ atm with $P_{O_2} = 10^{-28}$ atm. However, Cs_2SO_4 does possess high solubility in water (167 gm/100 mL of water at 0 °C). As in the case with the combination of Li_2SO_4 and Ag_2SO_4, the addition of Cs_2SO_4 to Ag_2SO_4 should also reduce its hygroscopic nature. This needs to be determined experimentally. Regardless, consideration should be given to the fact that the combination of water vapour and SO_3 will produce H_2SO_4, which results in

dissolution of numerous metal sulfates. Therefore, it may be necessary to remove water vapour from the gas input stream regardless of which metal sulfate is utilized.

$MnSO_4$ – This material is capable of operating at low partial pressures of SO_2 (~0.1 ppb) and at lower operating temperatures (i.e., 400-450 °C). The increase in ionic conductivity is 10X over that of pure Ag_2SO_4. However, the water solubility is relatively high at 70 gm/100 mL at 70 °C, but once combined with Ag_2SO_4 it should become less soluble.

$CoSO_4$ – As for $MnSO_4$, this material would have to be operated at a lower temperature (i.e., 400-450 °C) for detection of P_{SO_2} to ~0.1 ppm. The increase in ionic conductivity with this addition is 8.5X over pure Ag_2SO_4. Again the water solubility is relatively high at 83 gm/100 mL at 100 °C, but once combined with Ag_2SO_4 it should again lose its hygroscopic nature. This needs to be determined experimentally.

Silver sulfate has a solubility in water of 1.41 gm/100 mL at 100 °C which is relatively low. In the fabrication of composite electrolytes, consideration was also given to choosing dopant additions that are of low water solubility. The dopants consist of the following:

$BaSO_4$ - Noted for its extremely low solubility in water (0.00036 gm/100 mL) this material is ideal for exposure to water vapour. A phase transition from an alpha to beta phase in pure Ag_2SO_4 results in a large drop in conductivity at 420 °C. The addition of $BaSO_4$ reduces this transition so as to allow the sensor to be utilized over a range of temperature as large as 300-600 °C (the m.p. of pure Ag_2SO_4 is 652 °C). Could be utilized in a composite electrolyte up to 5 mole %. This component would increase the ionic conductivity of the parent Ag_2SO_4 material by a factor of 2.2X at 440 °C. These additions have also been found to enhance the conductivity of Ag_2SO_4 between 2-5 times by Liu et al. [43] . Also since the concentration of this dopant and all other dopants discussed can be reduced to levels less than 1 mol%, the activity of Ag_2SO_4 is essentially unity. It would also be possible to utilize a pure Ag reference electrode, since the effect of Ag diffusion into Ag_2SO_4 would be negligible. This is

very significant, since development of a chemical sensor with a thin film layer of Ag would greatly simplify fabrication of a miniaturized sensor.

There are other dopants to be considered consisting of:

$CaSO_4$ – This material possesses low solubility in water of 0.1619 gm/100 mL at 100 °C. The increase in conductivity would be 2.4X over pure Ag_2SO_4 at 440 °C.

$PbSO_4$ – The water solubility of this material is 0.0056 gm/100 mL at 40 °C. Ionic conductivity is increased 2.9X over pure Ag_2SO_4 at 440 °C.

$SrSO_4$ – The final material to be considered has a solubility of 0.014 gm/100 mL at 30 °C. The increase in ionic conductivity is relatively low at only 1.16X at 440 °C.

There are other classes of solid electrolytes which display high values of ionic conductivity and could be applied to measurement of SO_2. These consist of fluorine, lithium, sodium, potassium, silver and copper ionic conductors. For example, several forms of fluorine conductors such as CaF_2, SrF_2, BaF_2, and PbF_2, as well as $SrCl_2$ and UO_2, display high ionic conductivity [96] and may possibly be suitable for use as a sulfur oxide sensor. A fluoride solid solution consisting of CaF_2 with 1 mol% NaF displays a conductivity of $2x10^{-4}$ $S\,cm^{-1}$ at 350 °C [97]. This solid electrolyte would be combined with an auxiliary working electrode consisting of $CaSO_4$ and a suitable solid state reference electrode. In a similar fashion other sensor systems could be devised utilizing lithium, sodium, potassium, silver and copper ionic conductors. The main motivation for using one of these alternative ion conductors would be in the ease of fabrication of the required thin films. In the case of fluorides, established processes exist for evaporation and sputtering of thin films. This is also the case with other solid electrolytes.

In the development of an improved electrolyte several factors need to be measured:

- Ionic conductivity versus temperature (phase transitions present?)
- Ionic conductivity versus dopant concentration

- Water resistance versus dopant concentration
- Ionic conductivity versus SO_2 concentration. A quick method for determination of ionic conductivity.

It is apparent that there are several parameters that will be required to be optimized, resulting in a complex experiment. To minimize the number of experiments to be performed, orthogonal design as utilized in combinatorial techniques is highly recommended. This approach is commonly utilized in semiconductor manufacture for process optimization when several input parameters at different levels are involved [98]. These techniques are closely related to combinatorial and high throughput experimental (C.H.T.E.) techniques utilized in the field of parallel, miniaturized, high speed experimentation. Combinatorial design consists of experimental design where relationships between variables can be elucidated through the evaluation of their combinations. It has become a very powerful method for the discovery and selection of new materials for application in ceramics, catalysts and drugs, and for new electronic, optical and magnetic materials. It is particularly suited for the fabrication of thin film material libraries via fractional masking methods in combination with thin film vapour deposition equipment (i.e., sputtering, laser ablation, thermal and e-beam evaporation, ion deposition, etc.) [99]. It may be expedient in the interim to develop a thick film material library through the application of a modified ink-jet printer and ceramic inks [100-107].

Sensor Integration

In this present work thick films or bulk pellets were utilized for formation of the solid electrolyte. However, it is recommended to switch to fabrication of this device entirely through the use of thin films. There would be numerous advantages with thin films and the resulting integration including:

- Rapid response times from changes in gas concentration possible with a thin film electrolyte structure. Response times ideally need to be in the millisecond range

- Optimization of electrode microstructure through thin film fabrication would also reduce response times
- Further miniaturization possible with integrated heater
- Reduced power requirements
- Rapid changes in operational temperature possible
- Integration of multiple chemical sensors possible; there is a commercial need for the simultaneous detection of SO_2, NO_x, CO and CO_2
- Homogeneous temperature distribution possible with miniaturized design – reduces/eliminates thermoelectric forces
- Multiple sensors would permit advanced signal conditioning
- Amenable to mass fabrication techniques similar to that used in microchip manufacture

The geometries present with this device (in the range between 50-100 microns) are in no way as demanding as present day sub-micron chip manufacturing processes, but there would be some challenges with respect to its development. Development of a fabrication process would require a method for the deposition of sulfate based electrolytes, such as the two phase Li_2SO_4-Ag_2SO_4 electrolyte used in this work. There are other alternative sulfate solid electrolytes consisting of Ag_2SO_4 combined with either Cs_2SO_4, $MnSO_4$, $CoSO_4$, $BaSO_4$, $CaSO_4$, $PbSO_4$ or $SrSO_4$. These compositions could be combined with a pure Ag reference electrode, greatly simplifying the fabrication of a miniaturized integrated sensor. In Figure 13.1 a cross sectional view of the proposed sensor structure is presented. This sensor unlike previous designs incorporates the following improvements:

- The electrolyte layer consisting of a mixture of Ag_2SO_4 and the dopant metal sulfate ($MeSO_4$) is a thin film fabricated by either sputtering or sol-gel deposition.

- Both the reference (Ag) and working (Pt) electrode structures consist of standard thin film deposited materials. This would best be accomplished through physical deposition processes (i.e., evaporation or sputtering).

- The sealant layer could consist of alumina or an alumina based material. This layer could be deposited by sputtering or with a photoresist spinner (as used in photolithography). Since this could be patterned via photo-lithography techniques, the distance between the reference and working electrodes would be controllable. As the distance between these two electrodes is reduced the response time to changes in gas concentration would also be reduced. The minimum distance would depend on the performance of the lithography system and the quality of the sealant layer.

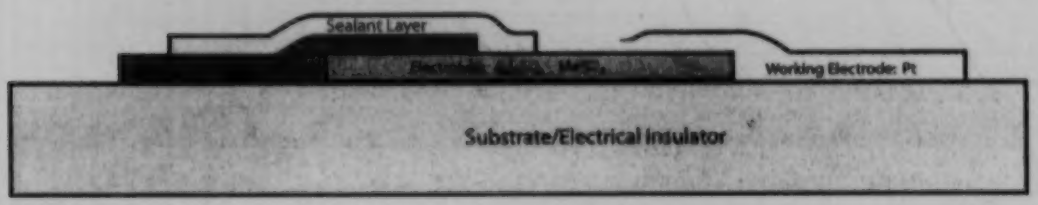

Figure 13-1. Cross-sectional view of Ag:Ag_2SO_4-$MeSO_4$ integrated sensor.

Absolutely necessary is an understanding of the thermal coefficient of expansion for the various layers required for fabrication of the integrated thin film sensor. Bulk thermal expansion coefficients are typically quite different than those for thin films. This information is critical in the design of a chemical sensor especially when combined with finite element analysis of the structure in response to temperature changes. Adjustments to the thickness and to the configuration of the layers could be made to optimize the design.

Additional Areas

There are some additional areas which need consideration and possibly further development:

- Devise an effective method for the conversion of $SO_2 \rightarrow SO_3$ at the micro-scale. Probably a properly engineered micro-porous Pt working electrode would be sufficient for this process. It is suggested that a sol-gel derived aerogel, doped with an appropriate catalyst could be utilized. Aerogels possess porosity in excess of 98% and have been shown to be suitable for conversion of NO to N_2 [108], and doped Cu-ZrO_2 aerogels can be used for methanol synthesis and Rh-ZrO_2 and Y_2O_3-ZrO_2 aerogels for methane oxidation [109]. The other possibility is a micro-machined channel containing Pt as a catalyst. This would be similar to micro-machined structures utilized for gas chromatography [110, 111].

- Attach multiple temperature probes for measurement of the temperature differential between the sensor and the walls of the test chamber. Combining this with the application of a carrier gas with significantly different molecular weight (i.e., He) will allow the effect of thermal diffusion at low concentrations to be determined.

- Potentiometric sensors are well-suited for measurements in real time. The intrinsic response time is a function of the kinetics of the different interfaces and of the ionic properties of the electrolyte. Extrinsic factors consist of diffusion of gaseous phases, convection, and interaction with all components in the sensor (adsorption and desorption phenomena). For these reasons it is critical that the response time of the sensor be determined. The design of the test cell chamber has to be made to reduce the gas residency time inside it and allow for rapid changes in gas concentration.

- Impedance analysis is an extremely powerful method for determining and characterizing the performance of the components in a chemical sensor. The electrical properties of solid electrolytes and associated electrodes are dependent on their structure. Therefore, depending on the deposition process, variations in the electrical characteristics of the electrolyte will be measurable

via impedance analysis. Impedance analysis would also permit identification of electrochemical processes at the electrode-electrolyte interfaces, including adsorption-desorption, chemical reactions, charge transfer and mass transfer. It is possible with this information to identify reaction mechanisms and the nature of the rate-limiting steps, and determine kinetic parameters.

Appendix A: Experimental Data for Sulfur Oxide Chemical Sensor

Table A-1. Cell No. 1: Composite reference electrode - emf versus [SO_2] and standard deviation (STDEV) of emf from 94 to 900 ppm SO_2 in air at 535 °C.

[mV]	[SO_2-ppm]	STDEV-[mV]
0.36350	93.800	0.0010
0.36900	116.10	0.0010
0.36600	124.40	0.0010
0.37300	167.40	0.0010
0.38150	172.50	0.0010
0.38500	191.80	0.0010
0.38100	202.80	0.0010
0.38500	218.20	0.0010
0.38700	219.10	0.0010
0.39700	273.60	0.0010
0.39900	288.50	0.0010
0.40300	322.60	0.0010
0.39950	340.00	0.0010
0.40000	342.30	0.0010
0.40650	372.40	0.0010
0.40500	394.80	0.0010
0.40900	395.50	0.0010
0.41000	447.40	0.0010
0.40800	455.10	0.0010
0.41400	486.50	0.0010
0.41250	488.90	0.0010
0.41900	540.00	0.0010
0.41750	576.30	0.0010
0.42250	640.80	0.0010
0.42300	642.90	0.0010
0.41900	649.40	0.0010
0.42100	680.00	0.0010
0.42600	703.40	0.0010
0.42450	721.60	0.0010
0.42550	750.00	0.0010
0.42350	754.40	0.0010
0.43100	900.00	0.0014

Table A-2. Cell No. 2: Ag thin film reference electrode- Emf versus time and standard deviation (STDEV) of emf for 496 ppm SO_2 in air at 535 °C.

Emf (Volts)	Time (Days:Hours:Minutes:Seconds)	STDEV-Emf(Volts)
0.35500	0:00:00:00	0.0010
0.28100	2:01:54:00	0.0010
0.29250	3:17:19:00	0.0010
0.38900	4:11:39:00	0.0010
0.37700	6:16:27:00	0.0010
0.38950	7:10:36:00	0.0010
0.38750	7:16:48:00	0.0010
0.40300	8:10:25:00	0.0010
0.39900	8:11:01:00	0.0010
0.39700	8:12:28:00	0.0010
0.40100	8:13:11:00	0.0010
0.41250	11:10:34:00	0.0010
0.40900	11:20:44:00	0.0010
0.40700	12:10:09:00	0.0010
0.40600	12:11:44:00	0.0010
0.40400	12:12:26:00	0.0010
0.39900	12:13:18:00	0.0010
0.39500	12:16:30:00	0.0010
0.39050	12:16:59:00	0.0010
0.38250	12:17:16:00	0.0010
0.43750	13:10:26:00	0.0010
0.42050	13:13:02:00	0.0010
0.44650	13:20:37:00	0.0010
0.43600	14:10:13:00	0.0010
0.42500	14:14:39:00	0.0010
0.42500	14:20:27:00	0.0010
0.41850	15:02:09:00	0.0010
0.42300	15:09:56:00	0.0010
0.43150	15:11:06:00	0.0010
0.41550	15:14:49:00	0.0010
0.40800	15:16:29:00	0.0010
0.40250	15:17:13:00	0.0010
0.40300	15:18:24:00	0.0010
0.40950	15:22:07:00	0.0010
0.39050	16:10:37:00	0.0010
0.39750	16:14:41:00	0.0010
0.38550	17:15:59:00	0.0010
0.40300	17:22:01:00	0.0010

0.38450	17:22:16:00	0.0010
0.40000	17:23:19:00	0.0010
0.45900	18:13:05:00	0.0010
0.48000	19:10:07:00	0.0010

Table A-3. Cell No. 2: Ag thin film reference electrode - Emf versus flow rate and standard deviation (STDEV) of emf in air at 535 °C.

Emf (Volts)	Flow rate (sccm)	STDEV-Emf (Volts)
0.4205	8.3	0.0010
0.4155	10.8	0.0096
0.4065	12.1	0.0010
0.4200	13.7	0.0010
0.4223	14.5	0.0051
0.4095	17.9	0.0042
0.4295	21.2	0.0010
0.4460	39.9	0.0010
0.4250	43.2	0.0010
0.4205	67.8	0.0010
0.4170	103.9	0.0010
0.3695	178.9	0.0010

Table A-4. Cell No. 3: Ag thick film reference electrode - %Variance from theory versus time for 100 to 2400 ppm SO_2 in air at 535 °C.

%Variance from theory	Time (Hours-Minutes-Seconds)
-1.2	0:00:00
-0.7	0:59:51
-0.1	1:59:42
0.5	2:59:34
0.4	3:59:25
0.8	4:59:16
1.5	5:59:08
1.5	6:58:59
1.9	7:58:50
1.7	8:58:42
1.6	9:58:33
1.5	10:58:24
1.8	11:58:15
1.6	12:58:07
1.7	13:57:58

1.7	14:57:49
1.6	15:57:41
2.1	16:57:32
0.8	17:19:47
0.5	17:19:59
25.2	17:27:28
6.4	17:57:23
3.4	18:27:19
1.9	18:57:15
1.6	19:27:10
1.2	19:57:06
0.9	20:27:02
0.6	20:56:57
0.9	21:26:53
2.2	21:56:49
1.2	22:26:44
1.0	22:56:40
1.3	23:26:35
1.8	23:56:31
1.5	24:26:27
1.6	24:56:22
1.5	25:26:18
1.3	25:56:14
1.2	26:26:09
1.7	26:56:05
1.0	27:26:01
1.6	27:55:56
1.4	28:25:52
1.4	28:55:48
1.7	29:25:43
1.6	29:55:39
1.4	30:25:35
2.0	30:55:30
1.9	31:25:26
1.7	31:55:22
1.7	32:25:17
2.3	32:55:13
1.9	33:25:09
1.7	33:55:04
1.8	34:25:00
1.3	34:54:55
1.8	35:24:51
1.8	35:54:47
1.5	36:24:42

1.4	36:54:38
1.1	37:24:34
0.7	37:54:29
1.5	38:24:25
1.1	38:54:21
0.9	39:24:16
2.1	39:54:12
3.6	40:54:03
-0.1	41:23:59
-1.6	41:53:55
-1.3	42:23:50
-1.7	42:53:46
-1.3	43:23:42
-1.3	43:53:37
-0.5	44:23:33
-0.7	44:53:31
-0.9	45:23:24
-0.4	45:53:20
-1.0	46:23:16
-0.4	46:53:11
-1.2	47:23:07
-0.9	47:53:02
-0.2	48:22:58
-1.2	48:52:54
-1.0	49:22:49
-1.5	49:52:45
-1.6	50:22:41
-1.7	50:52:36
-2.0	51:22:32
-1.7	51:52:28
-2.2	52:22:23
-1.7	52:52:19
-2.2	53:22:15
-2.2	53:52:10
-2.2	54:22:06
-2.3	54:52:02
-2.3	55:21:57
-2.3	55:51:53
-2.0	56:21:49
-2.4	56:51:44
-2.3	57:21:40
-2.6	57:51:36
-2.4	58:21:31
-2.6	58:51:27

-2.6	59:21:23
-2.5	59:51:18
-3.1	60:21:14
-2.7	60:51:10
-3.2	61:21:05
-2.9	61:51:01
-3.0	62:20:57
-2.2	62:50:52
-2.3	63:20:48
0.10	63:50:43
-4.0	64:35:37
-4.8	65:20:30
-5.3	66:05:24
-5.7	66:50:17
-5.7	67:35:11
-4.6	68:20:04
-5.2	69:04:58
-4.9	69:49:51
-4.7	70:34:45
-4.7	71:19:38
-4.7	72:04:32
-4.8	72:49:25
-4.5	73:34:19
-4.2	74:19:12
-4.2	75:04:06
-3.6	75:48:59
-4.0	76:33:53
-4.1	77:18:46
-4.2	78:03:40
-4.2	78:48:33
-4.3	79:33:26
-4.3	80:18:20
-4.1	81:03:14
-4.3	81:48:07
-4.3	82:33:00
-4.4	83:17:54
-4.7	84:03:31
-4.4	84:48:24
-4.9	85:33:18
-4.9	86:18:11
-5.2	87:03:05
-4.9	87:47:58
-4.9	88:32:52
-5.0	89:17:45

-4.9	90:02:39
-5.4	90:47:32
-5.3	91:32:26
-5.8	92:17:19
-5.5	93:02:13
-5.4	93:47:06
-6.1	94:32:00
-5.7	95:16:53
-6.5	96:01:47
-6.3	96:46:40
-5.9	97:31:34
-5.1	99:01:21
-7.4	99:46:14
-8.1	100:31:07
-8.3	101:16:01
-8.6	102:00:54
-8.0	102:45:48
-7.7	103:30:41
-6.8	104:15:35
-6.8	104:33:32
-11.8	128:56:00
-38.5	129:29:55
-41.9	132:59:26

Table A-5. Cell No. 3: Ag thick film reference electrode - Emf versus [SO_2] and standard deviation (STDEV) from 100 to 2400 ppm SO_2 in air at 525 °C.

Emf (Volts)	[SO_2-ppm]	STDEV-Emf(Volts)
0.3478	100	0.0143
0.3637	200	0.0131
0.3746	300	0.0136
0.3867	400	0.0156
0.3936	500	0.0157
0.4017	600	0.0146
0.4061	700	0.0148
0.4112	800	0.0143
0.4155	900	0.0145
0.4227	1000	0.0134
0.4259	1100	0.0132
0.4291	1200	0.0131
0.4322	1300	0.0130
0.4347	1400	0.0131

0.4374	1500	0.0129
0.4402	1600	0.0131
0.4419	1700	0.0127
0.4437	1800	0.0125
0.4456	1900	0.0122
0.4469	2000	0.0123
0.4486	2100	0.0124
0.4502	2200	0.0124
0.4520	2300	0.0125
0.4529	2400	0.0138

Table A-6. Cell No. 4: Composite thick film reference electrode - Emf versus [SO_2] and standard deviation (STDEV) of Emf for 100-2400 ppm SO_2 in air at 535°C.

Emf(Volts)	[SO_2-ppm]	STDEV-Emf(Volts)
0.3342	100	0.0055
0.3694	330	0.0073
0.3901	560	0.0070
0.4035	790	0.0057
0.4136	1020	0.0065
0.4212	1250	0.0054
0.4272	1480	0.0046
0.4333	1710	0.0049
0.4375	1940	0.0045
0.4417	2170	0.0045
0.4448	2400	0.0050

Table A-7. Cell No. 4: Composite thick film reference electrode - Emf versus [SO_2] and standard deviation (STDEV) of emf for 10-496 ppm SO_2 in air at 535 °C.

Emf(Volts)	[SO_2] ppm	STDEV-Emf(Volts)
0.2729	10	0.0042
0.2901	22	0.0029
0.2975	34	0.0052
0.3077	46	0.0036
0.3132	59	0.0046
0.3209	71	0.0016

0.3254	83	0.0017
0.3305	95	0.0009
0.3338	107	0.0018
0.3379	119	0.0006
0.3412	131	0.0025
0.3445	144	0.0006
0.3464	156	0.0013
0.3497	168	0.0006
0.3517	180	0.0016
0.3548	192	0.0008
0.3563	204	0.0017
0.3591	217	0.0010
0.3604	229	0.0017
0.3632	241	0.0011
0.3643	253	0.0022
0.3672	265	0.0020
0.3674	277	0.0016
0.3709	289	0.0018
0.3710	302	0.0019
0.3734	314	0.0014
0.3738	326	0.0019
0.3759	338	0.0014
0.3762	350	0.0016
0.3788	362	0.0011
0.3790	374	0.0016
0.3803	387	0.0012
0.3810	399	0.0016
0.3826	411	0.0012
0.3826	423	0.0013
0.3841	435	0.0007
0.3848	447	0.0016
0.3861	460	0.0008
0.3856	472	0.0013
0.3871	484	0.0006
0.3878	496	0.0022

Table A-8. Cell No. 4: Composite thick film reference electrode - Emf versus [SO_2] and standard deviation (STDEV) of emf for 5.4-95.4 ppm SO_2 in air at 535 °C.

Emf(Volts)	[SO_2-ppm]	STDEV-Emf(Volts)
0.2692	5.4	0.0066
0.2823	14.4	0.0060
0.2919	23.4	0.0036
0.3003	32.4	0.0032
0.3075	41.4	0.0033
0.3128	50.4	0.0023
0.3180	59.4	0.0025
0.3217	68.4	0.0016
0.3255	77.4	0.0013
0.3287	86.4	0.0011
0.3310	95.4	0.0011

Table A-9. Cell No. 4: Composite thick film reference electrode - Emf versus [SO_2] and standard deviation (STDEV) of emf for 0.6-11.6 ppm SO_2 in air at 535 °C.

Emf(Volts)	[SO_2] ppm	STDEV-Emf(Volts)
0.2471	0.6	0.0029
0.2500	1.6	0.0034
0.2523	2.6	0.0036
0.2545	3.6	0.0036
0.2567	4.6	0.0038
0.2587	5.6	0.0039
0.2605	6.6	0.0043
0.2638	7.6	0.0036
0.2656	8.6	0.0037
0.2673	9.6	0.0038
0.2693	10.6	0.0042
0.2720	11.6	0.0055

Table A-10. Cell No. 4: Composite thick film reference electrode - Emf versus [SO_2] and standard deviation (STDEV) of emf for 14.4 to 2400 ppm SO_2 in air at 535 °C.

[mVolts]	[SO_2-ppm]	STDEV-[mVolts]
0.2823	14.4	0.0060
0.2901	22.0	0.0029
0.2919	23.4	0.0036
0.3003	32.4	0.0032
0.2975	34.0	0.0052
0.3075	41.4	0.0033
0.3077	46.0	0.0036
0.3128	50.4	0.0023
0.3132	59.0	0.0046
0.3180	59.4	0.0025
0.3217	68.4	0.0016
0.3209	71.0	0.0016
0.3255	77.4	0.0013
0.3254	83.0	0.0017
0.3287	86.4	0.0011
0.3305	95.0	0.0009
0.3310	95.4	0.0011
0.3342	100.0	0.0055
0.3338	107.0	0.0018
0.3379	119.0	0.0006
0.3412	131.0	0.0025
0.3445	144.0	0.0006
0.3464	156.0	0.0013
0.3497	168.0	0.0006
0.3517	180.0	0.0016
0.3548	192.0	0.0008
0.3563	204.0	0.0017
0.3591	217.0	0.0010
0.3604	229.0	0.0017
0.3632	241.0	0.0011
0.3643	253.0	0.0022
0.3672	265.0	0.0020
0.3674	277.0	0.0016
0.3709	289.0	0.0018
0.3710	302.0	0.0019
0.3734	314.0	0.0014
0.3738	326.0	0.0019
0.3694	330.0	0.0073

0.3759	338.0	0.0014
0.3762	350.0	0.0016
0.3788	362.0	0.0011
0.3790	374.0	0.0016
0.3803	387.0	0.0012
0.3810	399.0	0.0016
0.3826	411.0	0.0012
0.3826	423.0	0.0013
0.3841	435.0	0.0007
0.3848	447.0	0.0016
0.3861	460.0	0.0008
0.3856	472.0	0.0013
0.3871	484.0	0.0006
0.3878	496.0	0.0022
0.3901	560.0	0.0070
0.4035	790.0	0.0057
0.4136	1020.0	0.0065
0.4212	1250.0	0.0054
0.4272	1480.0	0.0046
0.4333	1710.0	0.0049
0.4375	1940.0	0.0045
0.4417	2170.0	0.0045
0.4448	2400.0	0.0050

Table A-11. Cell No. 4: Composite thick film reference electrode – Emf versus flow rate and standard deviation (STDEV) of emf utilizing 200 ppm SO_2 in air at 535 °C.

Emf(mVolts)	Flow rate (sccm)	STDEV-Emf(mVolts)
0.3043	5	0.0078
0.3094	10	0.0006
0.3140	15	0.0004
0.3165	20	0.0012
0.3181	25	0.0010
0.3185	30	0.0011
0.3194	35	0.0008
0.3192	40	0.0007
0.3191	45	0.0004
0.3187	50	0.0005
0.3185	55	0.0004
0.3181	60	0.0010

Table A-12. Cell No. 4: Composite thick film reference electrode - Emf versus flow rate and standard deviation (STDEV) of emf utilizing 50 ppm SO_2 in air at 535 °C.

Emf(Volts)	Flow rate (sccm)	STDEV-Emf(Volts)
0.2784	5	0.0080
0.2900	15	0.0032
0.2947	25	0.0022
0.2949	35	0.0020
0.2947	45	0.0020
0.2935	55	0.0019
0.2921	65	0.0019
0.2905	75	0.0018
0.2889	85	0.0018
0.2876	95	0.0021

Table A-13. Cell No. 4: Composite thick film reference electrode - Emf versus flow rate and standard deviation (STDEV) of emf utilizing 5 ppm SO_2 in air at 535 °C.

Flow rate (sccm)	Emf(Volts)	STDEV-Emf(Volts)
5	0.2496	0.0012
15	0.2507	0.0016
25	0.2511	0.0006
35	0.2517	0.0010
45	0.2512	0.0012
55	0.2502	0.0010
65	0.2495	0.0013
75	0.2482	0.0011
85	0.2476	0.0008
95	0.2468	0.0006
105	0.2459	0.0004
115	0.2455	0.0010

Table A-14. Cell No. 5: Thick film solid electrolyte-Emf versus [SO_2] in air at 535°C.

Emf(Volts)	[SO_2-ppm]
0.2101	72
0.1963	71
0.2092	72
0.1986	97
0.1627	122
0.1862	121
0.1759	147
0.1683	171
0.1373	196
0.1625	197
0.1573	221
0.1293	246
0.1543	247
0.1544	272
0.1279	297
0.1540	296
0.1540	322
0.1302	347
0.1576	346
0.1314	371
0.1603	372
0.1621	396
0.1330	421
0.1631	422
0.1341	446
0.1611	447
0.1349	472
0.1681	471
0.1708	497
0.1378	522
0.1725	521
0.1391	546
0.1764	547
0.1792	571
0.1430	596
0.1841	597
0.1909	621
0.1471	647
0.1903	646
0.1949	672

0.1490	697
0.1997	696
0.2060	722
0.2106	746
0.1543	771
0.2134	772
0.2145	796
0.2601	847
0.1945	872
0.2761	871
0.2825	897
0.2825	921
0.1961	946
0.2830	947

Table A-15. Pressure, slope, y-intercept and temperature for sensitivity analysis.

Pressure (mmHg)	Slope (V/decade)	Y-Intercept	Temperature (°C)
650	0.07919	0.1832	525
660	0.07919	0.1835	525
670	0.07919	0.1837	525
680	0.07919	0.1840	525
690	0.07919	0.1842	525
700	0.07919	0.1845	525
710	0.07919	0.1847	525
720	0.07919	0.1850	525
730	0.07919	0.1852	525
740	0.07919	0.1854	525
750	0.07919	0.1857	525
760	0.07919	0.1859	525
770	0.07919	0.1861	525
780	0.07919	0.1863	525
790	0.07919	0.1866	525
800	0.07919	0.1868	525
650	0.07968	0.1803	530
660	0.07968	0.1806	530
670	0.07968	0.1809	530
680	0.07968	0.1811	530
690	0.07968	0.1814	530
700	0.07968	0.1816	530
710	0.07968	0.1819	530
720	0.07968	0.1821	530

730	0.07968	0.1823	530
740	0.07968	0.1826	530
750	0.07968	0.1828	530
760	0.07968	0.1830	530
770	0.07968	0.1833	530
780	0.07968	0.1835	530
790	0.07968	0.1837	530
800	0.07968	0.1839	530
650	0.08018	0.1775	535
660	0.08018	0.1777	535
670	0.08018	0.1780	535
680	0.08018	0.1783	535
690	0.08018	0.1785	535
700	0.08018	0.1788	535
710	0.08018	0.1790	535
720	0.08018	0.1793	535
730	0.08018	0.1795	535
740	0.08018	0.1797	535
750	0.08018	0.1800	535
760	0.08018	0.1802	535
770	0.08018	0.1804	535
780	0.08018	0.1807	535
790	0.08018	0.1809	535
800	0.08018	0.1811	535
650	0.08067	0.1746	540
660	0.08067	0.1749	540
670	0.08067	0.1751	540
680	0.08067	0.1754	540
690	0.08067	0.1757	540
700	0.08067	0.1759	540
710	0.08067	0.1762	540
720	0.08067	0.1764	540
730	0.08067	0.1766	540
740	0.08067	0.1769	540
750	0.08067	0.1771	540
760	0.08067	0.1774	540
770	0.08067	0.1776	540
780	0.08067	0.1778	540
790	0.08067	0.1780	540
800	0.08067	0.1783	540
650	0.08117	0.1718	545
660	0.08117	0.1720	545
670	0.08117	0.1723	545
680	0.08117	0.1725	545

690	0.08117	0.1728	545
700	0.08117	0.1731	545
710	0.08117	0.1733	545
720	0.08117	0.1736	545
730	0.08117	0.1738	545
740	0.08117	0.1740	545
750	0.08117	0.1743	545
760	0.08117	0.1745	545
770	0.08117	0.1747	545
780	0.08117	0.1750	545
790	0.08117	0.1752	545
800	0.08117	0.1754	545

Appendix B: Method of Least Squares

In calculating the best fit for a line, three quantities are defined consisting of the sum of squares, S_{xx}, S_{yy}, and S_{xy}, which are defined as follows:

$$S_{xx} = \sum x_i^2 - \frac{\left(\sum x_i\right)^2}{N} \tag{B.1}$$

$$S_{yy} = \sum y_i^2 - \frac{\left(\sum y_i\right)^2}{N} \tag{B.2}$$

$$S_{xy} = \sum x_i y_i - \frac{\sum x_i \sum y_i}{N} \tag{B.3}$$

From these quantities the following values are calculated:

The slope of the line m:

$$m = \frac{S_{xy}}{S_{xx}} \tag{B.4}$$

The intercept b:

$$b = \bar{y} - m\bar{x} \tag{B.5}$$

The standard deviation, s_y, of the residuals is given by:

$$s_y = \sqrt{\frac{S_{yy} - m^2 S_{xx}}{N-2}} \tag{B.6}$$

The standard deviation of the slope, s_m, given by:

$$s_m = \frac{s_y}{\sqrt{S_{xx}}} \tag{B.7}$$

while the standard deviation of the intercept, s_b, is given by:

$$s_b = s_y \sqrt{\frac{1}{N - \left(\sum x_i\right)^2 / \sum x_i^2}} \qquad \text{(B.8)}$$

The standard deviation utilizing the initial calibration curve followed by measurement of ordinate values, $s_{measured}$, is given by:

$$s_{measured} = \frac{s_y}{m} \sqrt{\frac{1}{L} + \frac{1}{N} + \frac{\left(\bar{y}_{measured} - \bar{y}\right)^2}{m^2 S_{xx}}} \qquad \text{(B.9)}$$

where $\bar{y}_{measured}$ is the mean calculated from a set of L measurements given by:

$$\bar{y}_{measured} = \frac{\sum y_i}{L} \qquad \text{(B.10)}$$

and $\bar{y}$ is the mean of a set of N measurements utilized in creation of the initial calibration curve given by:

$$\bar{y} = \frac{\sum y_i}{N} \qquad \text{(B.11)}$$

Appendix C: Standard Cell Potential, E°, and Associated Error

For calculation of the standard cell potential, E°, at 535°C/808.15K the following reactions are utilized:

$$2Ag + \tfrac{1}{2}S_2 + 2O_2 \rightleftharpoons Ag_2SO_4 \qquad \Delta G^o_{Ag_2SO_4} = -453,024 \pm 4,184\ J/mole\ [90] \qquad (C.1)$$

$$SO_3 \rightleftharpoons \tfrac{1}{2}S_2 + \tfrac{3}{2}O_2 \qquad \Delta G^0_{SO_3} = +326,218 \pm 6,276\ J/mole\ [60] \qquad (C.2)$$

$$2Ag_{(s)} + SO_{3(g)} + \tfrac{1}{2}O_{2(g)} \rightleftharpoons Ag_2SO_4 \qquad \Delta G^o_{cell(808.15K)} = -126,806 \pm 7,543\ J/mole \qquad (C.3)$$

For thermodynamic calculations the following values of the constants were utilized:

Molar Gas Constant (R) = 8.314472(15) J/mol K
Faraday Constant (F) = 96,485.3383(83) C/mol

The standard uncertainty (68% of Gaussian type error distribution) is the least significant digits as indicated by the terms in brackets. These values were current as of 2002, provided by the National Institute of Standards and Technology (N.I.S.T.), Gaithersburg, MD.

To calculate the value of ΔG^o_T for the cell reaction at alternative temperatures requires the application of the equation for the free energy of SO_3 (C.2) where:

$$\Delta G^o_{T,SO_3} = 456,976.5 - 161.8(T) \pm 6,276\ J/mole \qquad (C.4)$$

The second half of the cell reaction requires calculation of the free energy of formation for Ag_2SO_4, $\Delta G^o_{Ag_2SO_4}$, (equation C.1) which are provided in increments of 100 K in tabular form [112] or through calculation of this reaction at alternative temperatures, T, via the following equation:

$$\Delta G^{o}_{T.Ag_2SO_4} = \Delta H^{o}_{298} - T\Delta S^{o}_{298} + \int_{298}^{T} \Delta C_p dT - T\int_{298}^{T} \frac{\Delta C_p}{T} dT \qquad \text{(C.5)}$$

where ΔC_p is given by:

$$\Delta C_p = C_{p(\text{Products})} - C_{p(\text{Reactants})} \qquad \text{(C.6)}$$

Any phase changes due to crystal transformations (t), fusion (f) or evaporation (e), which occur in the temperature range between 298K and T must also be accounted for. In any case, the enthalpy, ΔH^{o}_{T}, or the entropy, ΔS^{o}_{T}, associated with a reaction is either subtracted when a reactant or added when a product to equation C.5. The value of ΔH^{o}_{T} is simply added or subtracted whereas ΔS^{o}_{T} associated with a phase change is added or subtracted through application of the following equation:

$$-T\left(\frac{\Delta H_{Phase\,Change}}{Temp.of\ Phase\,Change}\right) \qquad \text{(C.7)}$$

where T is the temperature of the reaction.

Error-cell voltage

The error in ΔG^{o}_{cell} is the combination of the error in $\Delta G^{o}_{Ag_2SO_4}$ and $\Delta G^{0}_{SO_3}$ according to the propagation of error (see Appendix E) and therefore:

$$\delta G^{o}_{cell} = \sqrt{\left(\delta G^{o}_{Ag_2SO_4}\right)^2 + \left(\delta G^{o}_{SO_3}\right)^2} = \sqrt{(4{,}184)^2 + (6{,}276)^2} = \pm 7{,}543\, J/mole \qquad \text{(C.8)}$$

The overall cell reaction (equation C.3) is associated with the standard cell potential at 808.15K, $E^{o}_{808.15K}$, by the equation:

$$\Delta G^{o}_{cell(808.15K)} = -n\, E^{o}_{808.15K}\, F \qquad \text{(C.9)}$$

It follows that:

$$E^{o}_{808.15} = \frac{-126,806\,J/mole}{-2(96,485.34\,C/mole)} = 0.6571V \qquad \text{(C.10)}$$

The relative error in the cell voltage, $\delta E^{o}_{808.15K}$, is given by:

$$\frac{\delta E^{o}_{808.15K}}{E^{o}_{808.15K}} = \sqrt{\left(\frac{7,543}{126,806}\right)^{2} + \text{Faraday constant(negligible error)}} = \pm 0.0595 \qquad \text{(C.11)}$$

It follows that the error in cell voltage is:

$$\delta E^{o}_{808.15K} = E^{o}_{808.15K}(\pm 0.0595) = 0.6571(\pm 0.0595) = \pm 0.0391V \qquad \text{(C.12)}$$

Therefore, the standard cell voltage at 808.15K including error is equal to:

$$E^{o}_{808.15K} = 0.6571 \pm 0.0391\,V \qquad \text{(C.13)}$$

For cell operation at 525°C the cell voltage can be calculated utilizing equation C.4 and thermodynamic data [90] as:

$$E^{o}_{798.15K} = \frac{-128,999\,J/mole}{-2(96,485.34)} = 0.6685V \qquad \text{(C.14)}$$

The error for 798.15K can be shown to equal:

$$\delta E^{o}_{798.15K} = 0.6685(\pm 0.0585) = \pm 0.0391V \qquad \text{(C.15)}$$

It follows that the standard cell voltage at 798.15K including error is equal to:

$$E^{o}_{798.15} = 0.6685 \pm 0.0391V \qquad \text{(C.16)}$$

Appendix D: Cell Equation and Associated Error

Cell Equation

The cell equation is described by:

$$E = E_T^o + \frac{RT}{2F}\ln\frac{\left(P_{O_2}\right)^{1/2}\left(P_{SO_3}\right)}{a_{Ag_2SO_4}} \qquad \text{(D.1)}$$

or:

$$E = E_T^o + \frac{2.30258RT}{2F}\log\frac{\left(P_{O_2}\right)^{1/2}\left(P_{SO_3}\right)}{a_{Ag_2SO_4}} \qquad \text{(D.2)}$$

Since E_T^o was calculated previously in Appendix C to equal 0.6402V, the cell temperature is 808.15K, since the average atmospheric pressure was observed to be 700 mmHg, $P_{O_2} = \left(\frac{700mmHg}{760mmHg}\right)0.2095\,atm = 0.1930\,atm$ and assuming that the theoretical activity of Ag_2SO_4 is 0.25, the cell equation becomes:

$$E = 0.6571 + 0.08018\log\frac{(0.1930)^{1/2}\left(P_{SO_3}\right)}{0.2984} \qquad \text{(D.3)}$$

The conversion of SO_2 to SO_3 occurs according to:

$$P_{SO_3} = \frac{P_{SO_2,in}}{\left[1+\frac{1}{K_P(PO_2)^{1/2}}\right]} \qquad \text{(D.4)}$$

where K_p is the equilibrium constant for the reaction $SO_2 + \frac{1}{2}O_2 \rightleftharpoons SO_3$.

The theoretical cell equation is therefore:

$$E = 0.1839 + 0.08018\log[SO_2, ppm] \quad at\ 535^oC/808.15K \qquad \text{(D.5)}$$

The theoretical cell equation for operation at 525 °C is derived as follows:

$$E = 0.6685 + 0.07919 \log \frac{(0.1930)^{1/2}\left(P_{SO_2}\right)}{0.3714} \qquad \text{(D.6)}$$

It follows that the cell equation at 525°C is equal to:

$$E = 0.1963 + 0.07919 \log\left(SO_2, ppm\right) \;\; at\, 525^{\circ}C / 798.15K \qquad \text{(D.7)}$$

Slope-error

Since the error due to measurement of cell temperature ($\pm 2K$) is many orders of magnitude more significant in comparison to the error present in gas constant, R, or the Faraday constant, F, then according to the propagation of error (see Appendix E) the relative error in the slope is equivalent to:

$$\frac{\delta slope}{slope} = \sqrt{\left(\frac{\delta Temperature}{Temperature}\right)^2} = \sqrt{\left(\frac{2}{808.15}\right)^2} = \pm 0.0025 \qquad \text{(D.8)}$$

and therefore for 535°C/808.15K the error in the slope is:

$$\delta\, slope = 0.08018\left(\pm 0.0025\right) = \pm 0.0002 \;\; at\, 535^{\circ}C \qquad \text{(D.9)}$$

It can also be shown that the error in the slope at 525°C/798.15K is:

$$\delta\, slope = 0.07919\left(\pm 0.0025\right) = \pm 0.0002 \;\; at\, 525^{\circ}C \qquad \text{(D.10)}$$

Y-intercept-error

The calculation of the y-intercept is obtained from the addition of three separate terms, two of which are calculated by the multiplying by the slope, the third being the standard cell voltage. Therefore, the error in the y-intercept is equal to:

$$\delta y - \text{int}\, ercept = \sqrt{\left(\delta E^{o}\right)^2 + \left(\delta \sec ond\, term\right)^2 + \left(\delta third\, term\right)^2} \qquad \text{(D.11)}$$

The error in the standard cell voltage, E°, was determined at both 525 °C and 535°C to equal:

$$\delta E^{\circ} = \pm 0.0391 \tag{D.12}$$

The relative error in the second term is equal to:

$$\frac{\delta second\ term}{second\ term} = \sqrt{\left(\frac{\delta slope}{second\ term}\right)^2} = \frac{0.0002}{.0272} = \pm 0.00735 \tag{D.13}$$

and therefore the error in the second term is:

$$\delta second\ term = \pm 0.00735(0.0272) = \pm 0.0002 \tag{D.14}$$

With the relative error in the third term consisting of:

$$\frac{\delta third\ term}{third\ term} = \sqrt{\left(\frac{\delta 0.0002}{0.0483}\right)^2} = \pm 0.00414 \tag{D.15}$$

it follows that the error in the third term is:

$$\delta third\ term = \pm 0.00414(0.0483) = \pm 0.0002 \tag{D.16}$$

As should be expected, it is apparent that the error in the second and third terms is equivalent to the error in the slope. Therefore, the error in the y-intercept at 535°C is equal to:

$$\delta y - intercept = \sqrt{(0.0391)^2 + (0.0002)^2 + (0.0002)^2} = \pm 0.0391\ V \tag{D.17}$$

It can also be shown that the error in the y-intercept at 525°C is also equal to $\pm 0.0391 V$.

Cell voltage measurement - error

The experimental error in measurement of the cell voltage consists of the STDEV from a series of measured cell voltages. Otherwise the potentiometer utilized (Keithley 617) is capable of voltage measurement with an accuracy of ±1 mV.

Description-plotting of reaction

According to equations D.5 or D.7, the slope of the line of emf(Volts) versus the log of the SO_2 concentration should theoretically be equal to 2.303(RT/nF) where n is the number of electrons involved in the electrochemical reaction, in this cell equal to 2. The theoretical cell equations, D.5 at 535°C and D.7 at 525°C, are linear equations of the form y = mx + b where y = emf(V), the slope = m, x = log[SO_2] and b equals the y-intercept. It follows that according to the cell equation, the theoretical value of the slope equals: 0.08018±0.0002 V/decade at 535 °C and 0.07919±0.0002 V/decade at 525°C. Since the value for x is equal to the log[SO_2] in ppm, the y-intercept is obtained when [SO_2] = 1 ppm. It follows that the theoretical value of the y-intercept is equal to 0.1790 ±0.0002 V at 535°C and 0.1974 ±0.0002 V at 525°C. A graph is provided in Figure D-1 to illustrate this point.

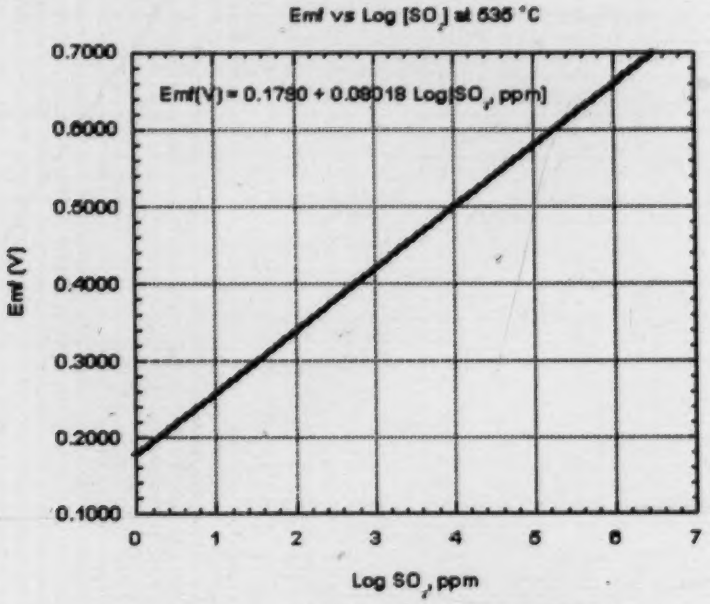

Figure D-1. Emf (V) versus log [ppm SO_2]

Appendix E: Propagation of Error Analysis

For the calculation of Ag_2SO_4 activity, error analysis must be taken into consideration. In the case of uncertainty in sums or differences the following equations are utilized:

$$q = x + \&.. + z - (u + \&. + w) \tag{E.1}$$

$$\delta q = \sqrt{(\delta x)^2 + ... + (\delta z)^2 + (\delta u)^2 + (\delta w)^2} \tag{E.2}$$

and for uncertainty in products and quotients where,

$$q = \frac{x \times ..... \times z}{u \times ..... \times w} \tag{E.3}$$

$$\frac{\delta q}{|q|} = \sqrt{\left(\frac{\delta x}{x}\right)^2 + ... + \left(\frac{\delta z}{z}\right)^2 + \left(\frac{\delta u}{u}\right)^2 + ... + \left(\frac{\delta w}{w}\right)^2} \tag{E.4}$$

For logarithms the following is applied in propagation of error where for a function, F, defined by:

$$F = \log x \tag{E.5}$$

the propagation of error due to x is given by:

$$\frac{e_F}{F} = (0.43429)e_x \tag{E.6}$$

Appendix F: Calculation of Adjusted Cell Molar Fraction

The required weight of Ag_2SO_4 and Li_2SO_4 for the solid electrolyte is first calculated. For the materials involved the following data were utilized:

$$\rho_{Ag_2SO_4} = 5.45\, gm/cm^3 \qquad MW_{Ag2SO4} = 311.800\, gm/mole$$
$$\rho_{Li_2SO_4} = 2.221\ gm/cm^3 \qquad MW_{Li2SO4} = 109.946\ gm/mole$$
$$MW_{Li_2SO_4 \cdot H_2O} = 127.956\, gm/mole$$

The volume of the solid electrolyte disc determines the weight of the components via the equation:

$$(gm - Ag_2SO_4)\left(\frac{1}{\rho_{Ag_2SO_4}}\right) + (gm - Li_2SO_4)\left(\frac{1}{\rho_{Li_2SO_4}}\right) = Volume \qquad \text{(F.1)}$$

For a disc 2 mm thick with a diameter of 25.4 mm, the volume is 1.0134 cm^3 which upon utilizing equation F.1 and the molecular weights (MW) of the individual components becomes:

$$(311.800\, gm/mole)(moles\ Ag_2SO_4)\left(\frac{cm^3}{5.45\, gm}\right) + (109.946\, gm/mole)(moles\ Li_2SO_4)\left(\frac{cm^3}{2.221\, gm}\right) = 1.0134\, cm^3 \qquad \text{(F.2)}$$

and since:

$$0.25 = \frac{moles\ Ag_2SO_4}{moles\ Ag_2SO_4 + moles\ Li_2SO_4} \qquad \text{(F.3)}$$

which is equivalent to:

$$3(moles\ Ag_2SO_4) = moles\ Li_2SO_4 \qquad \text{(F.4)}$$

Combining equations F.2 and F.4 results in:

$$205.719(moles\ Ag_2SO_4) = 1.0134 cm^3 \qquad \text{(F.5)}$$

Therefore:

$$moles\ Ag_2SO_4 = 0.00493 \tag{F.6}$$

and:

$$moles\ Li_2SO_4 = 0.01478 \tag{F.7}$$

These initial calculations assume that the Li_2SO_4 is not hydrated. However, if the Li_2SO_4 were actually hydrated in the form of $Li_2SO_4 \cdot H_2O$ at the time of weighing, the effective activity of Ag_2SO_4 during operation would be altered. This is assuming that $Li_2SO_4 \cdot H_2O$ is de-hydrated above 130°C at the cell's operating temperature of 535°C.

The initial weight of $Li_2SO_4 \cdot H_2O$ is equal to the amount of "Li_2SO_4" assumed to be weighed out, as determined by equation F.7 and the $MW_{Li_2SO_4}$ given as:

$$gm\ Li_2SO_4 \bullet H_2O\ weighed\ out = moles\ Li_2SO_4\ (MW_{Li_2SO_4}) \tag{F.8}$$

Assuming that $Li_2SO_4 \cdot H_2O$ was weighed instead of Li_2SO_4, the moles of $Li_2SO_4 \cdot H_2O$ is equal to:

$$moles\ Li_2SO_4 \bullet H_2O = gm\ Li_2SO_4 \bullet H_2O\ weighed\ out \left(\frac{1}{MW_{Li_2SO_4 \bullet H_2O}}\right) \tag{F.9}$$

According to the dehydration of $Li_2SO_4 \cdot H_2O$:

$$Li_2SO_4 \bullet H_2O \rightarrow Li_2SO_4 + H_2O\uparrow \tag{F.10}$$

Therefore, the number of moles of $Li_2SO_4 \cdot H_2O$, Li_2SO_4 and H_2O are equivalent. It follows that the adjusted Ag_2SO_4 mole fraction is equal to:

$$\begin{matrix} adjusted\ Ag_2SO_4 \\ mole\ fraction \end{matrix} = \frac{moles\ Ag_2SO_4}{moles\ Ag_2SO_4 + moles\ Li_2SO_4 \left(MW_{Li_2SO_4}\right)\left(\frac{1}{MW_{Li_2SO_4 \bullet H_2O}}\right)} \tag{F.11}$$

Substituting the values from equations F.6 and F.7 into F.11 results in an adjusted Ag_2SO_4 mole fraction equal to 0.2796. This is well within the two phase region for Ag_2SO_4-Li_2SO_4 at 535°C.

References

[1] C. D. Eastman, T. H. Etsell, and M. J. Brett, "Minaturised Sulphur Oxide Integrated Sensor," presented at High Temperature Materials Chemistry, Proceedings of the C.B. Alcock Symposium, London, 1995.

[2] C. D. Eastman and T. H. Etsell, "Thick/thin film sulfur oxide chemical sensor," *Solid State Ionics*, vol. 136-137, pp. 639-45, 2000.

[3] L. B. Valdes, "Resistivity measurements on germanium for transistors," *Proceedings of the IRE*, vol. 42, pp. 430-437, 1954.

[4] D. E. Smith, *AC Polarography and Related Techniques: Theory and Practice in Electroanalytical Chemistry*, vol. 1. New York, 1966.

[5] J. S. Lundsgaard, J. Malling, and M. L. S. Birchall, "A novel hydrogen gas sensor based on hydrogen uranyl phosphate," *Solid State Ionics*, vol. 7, pp. 53-56, 1982.

[6] N. Miura and N. Yamazoe, "Development of new chemical sensors based on low-temperature proton conductors," *Solid State Ionics*, vol. 23-56, pp. 975-982, 1992.

[7] W. L. Worrell, "Solid-Electrolyte Sensors for SO_2 and/or SO_3," in *Chem. Sensor Technol.*, vol. 1, T. Seiyama, Ed. Amsterdam: Elsevier, pp. 97-108, 1988

[8] K. T. Jacob and D. B. Rao, "Solid-State Probe for SO_2-SO_3 Based on Na_2SO_4-I Electrolyte," *J. Electrochem. Soc.*, vol. 126, pp. 1842-1847, 1979.

[9] M. Gauthier and A. Chamberland, "Solid-State Detectors for Potentiometric Determination of Gaseous Oxides .1. Measurement in Air," *Journal of the Electrochemical Society*, vol. 124, pp. 1579-1583, 1977.

[10] R. Cote, C. W. Bale, and M. Gauthier, "K_2CO_3 Solid Electrolyte as a CO_2 Probe: Decomposition Measurements of $CaCO_3$," *J. Electrochem. Soc.*, vol. 131, pp. 63-67, 1984.

[11] A. Pelloux, P. Fabry, and P. Durante, "Design and testing of a potentiometric chlorine gauge," *Sensors and Actuators*, vol. 7, pp. 245-52, 1985.

[12] T. Maruyama, Y. Saito, Y. Matsumoto, and Y. Yano, "Potentiometric sensor for sulfur oxides using NASICON as a solid electrolyte," *Solid State Ionics*, vol. 17, pp. 281-6, 1985.

[13] Y.-I. Bang, K.-D. Song, B.-S. Joo, J.-S. Huh, S.-D. Choi, and D.-D. Lee, "Thin film micro carbon dioxide sensor using MEMs," *Sensors Actuators B*, vol. 102, pp. 20-26, 2004.

[14] R. Mouazer, M. Persin, M. Cretin, and A. Larbot, "Elaboration of Nasicon/$ZnAl_2O_4$ thin films for ultrafiltration of ionic solutions," *Separation Purification Technol.*, vol. 32, pp. 111-116, 2003.

[15] B. J. Ward, C. C. Liu, and G. W. Hunter, "Novel processing of NASICON and sodium carbonate/barium carbonate thin and thick films for a CO_2 microsensor," *J. Mater. Sci.*, vol. 38, pp. 4289-4292, 2003.

[16] Y. Shimizu and T. Ushijima, "Sol-gel processing of NASICON thin film using aqueous complex precursor," *Solid State Ionics*, vol. 132, pp. 143-148, 2000.

[17] E. D. Bartolomeo and E. Traversa, "Influence of Humidty on Electrochemical CO_2 Sensors Based on Sol-Gel Processed NASICON with New Compositions," *J. Sol-Gel Sci.Technol.*, vol. 19, pp. 181-185, 2000.

[18] M. Meunier, R. Izqueirdo, L. Hasnaoui, E. Quenneville, D. Ivanov, F. Girard, F. Morin, A. Yelon, and M. Paleologou, "Pulsed laser deposition of superionic ceramic thin films: deposition and applications in electrochemistry," *Appl. Surf. Sci.*, vol. 127-129, pp. 466-470, 1998.

[19] E. Steudel, P. Birke, and W. Weppner, "Miniaturized solid state electrochemical CO_2 sensors," *Electrochim. Acta*, vol. 42, pp. 3147-3153, 1997.

[20] M. Morcrette, P. Barboux, A. Laurent, and J. Perriere, "Growth and characterization of nasicon thin films by the laser ablation method," *Solid State Ionics*, vol. 93, pp. 283-290, 1997.

[21] M. Morcrette, P. Barboux, J. Perriere, A. Laurent, J. P. Boilot, and T. Brousse, "Thin films of ionic conductors by laser ablation," presented at Solid State Ionics V. Symposium, Boston, MA, USA, 1999.

[22] R. Izquierdo, et al., "Pulsed laser deposition of nasicon thin films," *Appl. Surf. Sci.*, vol. 96-98, pp. 855-858, 1996.

[23] T. Lang, et. al., "Material characterization of sputtered sodium-ion conductive ceramics for a prototype CO_2 micro-sensor," *Sensors Actuators B*, vol. 31, pp. 9-12, 1996.

[24] D. Ivanov, et al., "Sputtered silicate-limit NASICON thin films for electrochemical sensors," *Solid State Ionics*, vol. 67, pp. 295-299, 1994.

[25] A. Ahmad, C. Glasgow, and T. A. Wheat, "Sol-gel processing of NASICON thin-film precursors," *Solid State Ionics*, vol. 76, pp. 143-154, 1995.

[26] R. Akila and K. T. Jacob, "An SO_x (x=2,3) sensor using beta -alumina Na_2SO_4 couple," *Sensors Actuators*, vol. 16, pp. 311-23, 1989.

[27] Y. Shimizu, Y. Okamoto, S. Yao, N. Miura, and N. Yamazoe, "Solid electrolyte NO_2 sensors fitted with sodium nitrate and/or barium nitrate electrodes," *Denki Kagaku*, vol. 59, pp. 465-72, 1991.

[28] T. Maruyama, S. Sasaki, and Y. Saito, "Potentiometric gas sensor for carbon dioxide using solid electrolytes," *Solid State Ionics*, vol. 23, pp. 107-12, 1987.

[29] N. Miura, J. Hisamoto, and N. Yamazoe, "Solid-state oxygen sensor using sputtered LaF_3 film," *Sensors Actuators*, vol. 16, pp. 301-310, 1989.

[30] J. Will, A. Mitterdorfer, D. Kleinlogel, D. Perednis, and L. J. Gauckler, "Fabrication of thin electrolytes for second -generation solid oxide fuel cells," *Solid State Ionics*, vol. 131, pp. 79-96, 2000.

[31] S. Yao, S. Hosohara, N. Shimizu, N. Miura, H. Futata, and N. Yamazoe, "Solid Electrolyte CO_2 Sensor Using Nasicon and Li-Based Binary Carbonate Electrode," *Chem. Lett.*, pp. 2069-2072, 1991.

[32] N. Miura, S. Yao, Y. Shimizu, and N. Yamazoe, "Development of High-Performance Solid-Electrolyte Sensors for NO and NO2," *Sensors and Actuators B*, vol. 13-14, pp. 387-390, 1993.

[33] Y. Yan, Y. Shimizu, N. Miura, and N. Yamazoe, "Solid-State Sensor for Sulfur-Oxides Based on Stabilized Zirconia and Metal Sulfate," *Chem. Lett.*, pp. 635-638, 1992.

[34] N. Miura, Y. Yan, M. Sato, S. Yao, Y. Shimizu, and N. Yamazoe, "Stabilized Zirconia Based CO_2 Sensors Combined with Carbonate Auxiliary Phase," *Chem. Lett.*, pp. 393-396, 1994.

[35] H. Kurosawa, Y. T. Yan, N. Miura, and N. Yamazoe, "Stabilized Zirconia-Based Potentiometric Sensor for Nitrogen- Oxides," *Chem. Lett.*, pp. 1733-1736, 1994.

[36] N. Miura, S. Yao, M. Sato, Y. Shimizu, S. Kuwata, and N. Yamazoe, "Carbon-Dioxide Sensor Using Combination of Fluoride-Ion Conductor and Metal Carbonate," *Chem. Lett.*, pp. 1973-1976, 1993.

[37] F. J. Salzano and L. Newman, "Sulfur Trioxide, Oxygen, Platinum Electrode in a Fused Sulfate," *J. Electrochem. Soc.*, vol. 119, pp. 1273-1278, 1972.

[38] M. Gauthier, A. Chamberland, A. Belanger, and M. Poirier, "Solid-State Detectors for Potentiometric Determination of Gaseous Oxides .2. Measurements in Oxygen-Variable Gases in SO_2, SO_3, O_2, Pt-$SO_4^=$ System," *J. Electrochem. Soc.*, vol. 124, pp. 1584-1587, 1977.

[39] Q. G. Liu and W. L. Worrell, "Development of a solid electrolyte to measure sulfur potentials in oxidizing environments," presented at Chemical Metallurgy - A Tribute to Carl Wagner, Chicago, Illinois, 1981.

[40] Q. G. Liu and W. L. Worrell, "Physical Chemistry of Extractive Metallurgy: Proceedings of an International Symposium," Y. K. Rao and V. Kudryk, Eds. Warrendale, PA: The Minerals, Metals & Materials Society, 1985.

[41] C. M. Mari, M. Beghi, S. Pizzini, and J. Faltemier, "Electrochemical Solid-State Sensor for SO_2 Determination in Air," *Sensors Actuators B*, vol. 2, pp. 51-55, 1990.

[42] Q. G. Liu, "Ph.D. Dissertation." Philadelphia: University of Pennsylvania, 1987.

[43] Q. G. Liu, X. D. Sun, and W. J. Wu, "A New SO_2/SO_3 Sensor with Ag_2SO_4-Based Electrolyte," *Solid State Ionics*, vol. 40-1, pp. 456-459, 1990.

[44] K. T. Jacob, M. Iwase, and Y. Waseda, "A galvanic sensor for SO_3-SO_2 based on the CaF_2-$CaSO_4$ couple," *Solid State Ionics*, vol. 23, pp. 245-52, 1987.

[45] S.-D. Choi, W.-Y. Chung, and D.-D. Lee, "SO_2 sensing characteristics of Nasicon electrolytes," *Sensors Actuators B*, vol. B36, pp. 263-6, 1996.

[46] J. F. Currie, A. Essalik, and J. C. Marusic, "Micromachined thin film solid state electrochemical CO_2, NO_2 and SO_2 gas sensors," *Sensors Actuators B*, vol. 59, pp. 235-241, 1999.

[47] S. Suganuma, M. Watanabe, T. Kobayashi, and S.-I. Wakabayashi, "SO_2 gas sensor utilizing stabilized zirconia and sulfate salts with a new working mechanism," *Solid State Ionics*, vol. 126, pp. 175-9, 1999.

[48] S. S. Bhoga, K. Singh, J. Randhawa, and P. D. Borkar, "Ag^+ glass-Ag_2SO_4 composite solid electrolyte based SO_2 galvanic sensor," *Sensors Actuators B*, vol. 55, pp. 70-76, 1999.

[49] K. Singh and S. S. Bhoga, "On the insertion of $70Li_2O$:$3B_2O_3$ glass in to the polycrystalline $6Li_2SO_4$-$4Li_2CO_3$ composite system," *J. Electroanalyt. Chem.*, vol. 137, pp. 1970-1974, 1990.

[50] G. M. Kale, L. Wang, and Y. R. Hong, "Planar SO_x sensor incorporating a bi-electrolyte couple," *Solid State Ionics*, vol. 161, pp. 155-163, 2003.

[51] J. Maier, M. Holzinger, and W. Sitte, "Fast Potentiometric CO_2 Sensors with Open Reference Electrodes," *Solid State Ionics*, vol. 74, pp. 5-9, 1994.

[52] M. Holzinger, J. Maier, and W. Sitte, "Fast CO_2-selective potentiometric sensor with open reference electrode," *Solid State Ionics*, vol. 86-88, pp. 1055-62, 1996.

[53] M. Holzinger, J. Maier, and W. Sitte, "Potentiometric detection of complex gases: Application to CO_2," *Solid State Ionics*, vol. 94, pp. 217-25, 1997.

[54] B.-K. Min and S.-D. Choi, "SO_2-sensing characteristics of Nasicon sensors with Na_2SO_4-$BaSO_4$ auxiliary electrolytes," *Sensors Actuators B*, vol. 93, pp. 209-213, 2003.

[55] N. Miura, S. Yao, Y. Shimizu, and N. Yamazoe, "Carbon-Dioxide Sensor Using Sodium-Ion Conductor and Binary Carbonate Auxiliary Electrode," *J. Electrochem. Soc.*, vol. 139, pp. 1384-1388, 1992.

[56] N. Rao, C. M. van den Bleek, J. Schoonman, and O. T. Sorensen, "A novel temperature-gradient Na^+- beta "-alumina solid electrolyte based SO_x gas sensor without gaseous reference electrode," *Solid State Ionics*, vol. 53-56, pp. 30-8, 1992.

[57] L. Wang and R. V. Kumar, "A new SO_2 gas sensor based on an Mg^{2+} conducting solid electrolyte," *J. Electroanal. Chem.*, vol. 543, pp. 109-114, 2003.

[58] J. Kirchnerova, C. W. Bale, and J. M. Skeaff, "Potentiometric gaseous sulfur sensor based on silver beta-alumina solid electrolyte," *Solid State Ionics*, vol. 91, pp. 257-64, 1996.

[59] F. Vandecruys, E. Brauns, W. Engelen, F. De Schutter, and J. Vangrunderbeek, "A H_2S-sensor for on-line measurements in a coal gasification system," *Solid State Ionics*, vol. 112, pp. 95-102, 1998.

[60] O. Kubaschewski and C. B. Alcock, *Metallurgical Thermochemistry*, 5th ed. New York: Pergamon Press, 1979.

[61] S. Dushmman, *Scientific Foundations of Vacuum Techniques*. New York: John Wiley & Sons, 1962.

[62] M. Gauthier, R. Bellemare, and A. Belanger, "Progress in the Development of Solid-State Sulfate Detectors for Sulfur-Oxides," *J. Electrochem. Soc.*, vol. 128, pp. 371-378, 1981.

[63] A. Kvist and A. Lunden, *Z. Naturforsch.*, vol. 20a, pp. 235, 1965.

[64] Q. G. Liu and W. L. Worrell, "Electrical conductivity of Li_2SO_4-Ag_2SO_4 solid electrolytes," *Solid State Ionics*, vol. 18-19, pp. 524-8, 1986.

[65] M. Natarajan and E. A. Secco, "Electrical-Conductivity and Phase-Transformation Studies on Pure and Doped (Mg^{2+},Zn^{2+},Cu^{2+}, and Mn^{2+}) Crystals of K_2SO_4," *Can. J. Chem.-Revue*, vol. 53, pp. 1542-1547, 1975.

[66] W. L. Worrell and Q. G. Liu, in: T. Seiyama, K. Fueki, J. Shiokawa and S. Suzuki (Eds.), Proc. Int. Meet. Chem. Sensors, Fukuoka, Japan, Sept. 19-22, Anal. Chem. Symp. Series, 17, (1983) 332.

[67] M. Gauthier, "Application of a New Potentiometric Technique Based on Solid Oxyanion-Bearing Electrolytes for Determination of Thermal- Stability of Sulfates," *Cim Bulletin*, vol. 70, pp. 134-134, 1977.

[68] L. Borjesson and L. M. Torell, "Raman-Scattering evidence of rotating SO_4^{2-} in solid sulphate electrolytes," *Solid State Ionics*, vol. 18-19, pp. 582-586, 1986.

[69] L. Nilsson, "Ph.D. Thesis." Goteborg. Chalmers University of Technology, 1981.

[70] A. Lunden, "Enhancement of cation mobility in some sulphate phases due to a paddle-wheel mechanism," *Solid State Ionics*, vol. 28-30, pp. 163-167, 1988.

[71] R. Tarneberg and E. Mellander Bengt, "Ion transport in high temperature rotator phase solid electrolytes," *Solid State Ionics*, vol. 98, pp. 175-183, 1997.

[72] R. Tarneberg and A. Lunden, "Ion diffusion in the high-temperature phases Li_2SO_4, $LiNaSO_4$, $LiAgSO_4$ and $Li_4Zn(SO_4)_3$," *Solid State Ionics*, vol. 90, pp. 209-220, 1996.

[73] A. Kvist and A. Bengtzelius, *Fast ion transport in solids*. Amsterdam: North-Holland, 1973.

[74] H. A. Oye, "Phase diagram Li_2SO_4-Ag_2SO_4 from concentration cell measurements," *Acta Chemica Scandinavica*, vol. 18, pp. 361, 1964.

[75] O. M. Sreedharan. Bombay: University of Bombay, 1975.

[76] M. Sato, *Research Techniques for High Pressure and High Temperature*. New York: Springer-Verlag, 1971.

[77] O. M. Sreedharan, "Proc. Symp. on High Temperature Chemistry," Bombay, India, 1982.

[78] O. M. Sreedharan, E. Athiappan, R. Pankajavalli, and J. B. Gnanamoorthy, "Free-energy of formation of GeO_2(Hex) by EMF Measurements," *J. Less-Common Metals*, vol. 68, pp. 143-152, 1979.

[79] O. M. Sreedharan, M. S. Chandrasekharaiah, and E. S. Ramakrishnan, "Free-energy of formation of iridium oxide by solid electrolyte galvanic cell," *J. Electrochem. Soc.*, vol. 122, pp. 328-331, 1975.

[80] R. Pankajavalli, O. M. Sreedharan, E. Athiappan, and J. B. Gnanamoorthy, *J. Electrochem. Soc. India*, vol. 30, pp. 224, 1981.

[81] H. H. Kellogg, "Thermodyanmic properties of oxides of copper and nickel," *J. Chem. Eng. Data*, vol. 14, pp. 41, 1969.

[82] R. A. Giddings and R. S. Gordon, "Review of oxygen activities and phase boundaries in wustite as determined by the electromotive-force and gravimetric methods," *J. Am. Ceram. Soc.*, vol. 56, pp. 111-116, 1973.

[83] O. Sjoden, S. Seetharaman, and L. I. Staffansson, "On the gibbs energy of formation of wustite," *Metallurg. Trans. B*, vol. 17, pp. 179-184, 1986.

[84] C. Mallika, O. M. Sreedharan, and R. Subasri, "Use of air/platinum as the reference electrode in solid oxide electrolyte e.m.f. measurements," *J. Eur. Ceram. Soc.*, vol. 20, pp. 2297, 2000.

[85] V. Stancovski, S. Sridhar, and U. Pal, "Thermodynamic Stability and Interfacial Impedance of Solid-Electrolyte Cells with Noble-Metal Electrodes," *J. Electroceram.*, vol. 3:3, pp. 279-299, 1999.

[86] W. Fang and C.-Y. Lo, "On the thermal expansion coefficients of thin films," *Sensors Actuators*, vol. 84, pp. 310-314, 2000.

[87] O. Kraft and W. D. Nix, "Measurement of the lattice thermal expansion coefficents of thin metal films on substrates," *J. Appl. Phys.*, vol. 83, pp. 3035-3038, 1998.

[88] D. S. Campbell, *Handbook of Thin Film of Technology*, 1st (1983 reissue) ed. New York: McGraw-Hill, 1970.

[89] W. L. Worrell and Q. G. Liu, "A New Sulfur-Dioxide Sensor Using a Novel 2-Phase Solid-Sulfate Electrolyte," *J. Electroanalyt. Chem.*, vol. 168, pp. 355-362, 1984.

[90] I. Barin and O. Knacke, *Thermochemical data of pure substances*, second ed. Weinheim: Verlagsgesellschaft (VCH), 1993.

[91] N. Imanaka, Y. Yamaguchi, G. Adachi, and J. Shiokawa, "Sulfur-Dioxide Gas-Detection with Na_2SO_4-$Y_2(SO_4)_3$-SiO_2 Solid Electrolyte by a Solid Reference Electrode Method," *J. Electrochem. Soc.*, vol. 132, pp. 2519-2520, 1985.

[92] K. E. Grew and T. L. Ibbs, *Thermal diffusion in gases*. Cambridge: Cambridge University Press, 1952.

[93] G. Vasaru, G. Muller, G. Reinhold, and T. Fodor, *The Thermal Diffusion Column*. Berlin: VEB Deutscher Verlag Der Wissenschaften, 1969.

[94] E. I. Hellund, "Generalized Theory of Diffusion. II," *Phys. Rev.*, vol. 57, pp. 328-333, 1940.

[95] R. C. Jones, "On the theory of the thermal diffusion coefficient for isotopes. II," *Phys. Rev.*, vol. 59, pp. 1019-1033, 1941.

[96] A. L. Laskar and S. Chandra, *Superionic Solids and Solid Electrolytes-Recent Trends*. New York: Academic Press Ltd., 1989.

[97] S. Chandra, *Superionic Solids: Principles and Applications*: Elsevier North-Holland, 1981.

[98] Z. Y. Gerald and D. W. Jillie, "Orthogonal Design for Process Optimization and Its Application in Plasma Etching," *Solid State Technol.*, pp. 127-132, 1987.

[99] J. N. Cawse, *Experimental design for combinatorial and high throughput materials development*. Hoboken, New Jersey: Wiley-Interscience, 2003.

[100] W. D. Teng, M. J. Edirisinghe, and R. G. Evans, "Optimization of dispersion and viscosity of a ceramic jet printing ink," *J. Amer. Ceram. Soc.*, vol. 80, pp. 486-494, 1997.

[101] M. Mott, J.-H. Song, and J. R. G. Evans, "Microengineering of ceramics by direct ink-jet printing," *J. Amer. Ceram. Soc.*, vol. 82, pp. 1653-1658, 1999.

[102] W. D. Teng and M. J. Edirisinghe, "Development of ceramic inks for direct continuous jet printing," *J. Am. Ceram. Soc.*, vol. 81, pp. 1033-36, 1998.

[103] J. H. Song, M. J. Edirisinghe, and J. R. G. Evans, "Formulation and multiplayer jet printing of ceramic inks," *J. Amer. Ceram. Soc.*, vol. 82, pp. 3374-80, 1999.

[104] P. Blazdell and S. Kuroda, "Plasma spraying of submicron ceramic suspensions using a continuous ink jet printer," *Surf. Coat. Technol.*, vol. 123, pp. 239-46, 2000.

[105] B. Y. Tay and M. J. Edirisinghe, "Investigation of some phenomena occurring during continuous ink-jet printing of ceramics," *J. Mat. Res.*, vol. 16, pp. 373-84, 2000.

[106] K. A. M. Seerden, N. Reis, J.R.G. Evans, P.S. Grant, J.W. Halloran and B. Derby, "Ink-jet printing of waxbased alumina suspensions," *J. Amer. Ceram. Soc.*, vol. 84, pp. 2514-20, 2001.

[107] P. Blazdell and S. Kuroda, "Bimodal ceramic ink for continuous ink-jet printer plasma spraying," *J. Amer. Ceram. Soc.*, vol. 84, pp. 1257-59, 2001.

[108] H. Hirashima, C. Kojima, and H. Imai, "Application of alumina aerogels as catalysts," *J. Sol-Gel Sci.Technol.*, vol. 8, pp. 843-846, 1997.

[109] P. A. Sermon, V. A. Self, and Y. Sun, "Doped-ZrO2 aerogels: catalysts of controlled structure and properties," *J. Sol-Gel Sci. Technol.*, vol. 8, pp. 851-856, 1997.

[110] M. Kim and M. Somenath, "A microfabricated microconcentrator for sensors and gas chromatography," *J. Chromatogr. A*, vol. 996, pp. 1-11, 2003.

[111] J. A. Potkay, et al., "A high-performance microfabricated gas chromatography column," presented at Proceedings of the IEEE Micro Electromechanical Systems (MEMS), Kyoto, Japan, 2003.

[112] I. Barin and O. Knacke, *Thermochemical Properties of Inorganic Substances*, vol. 1, 1st ed. Berlin: Springer, 1973.